

**Theoretical studies on spintronics
materials: Angle-resolved
photoemission of Weyl semimetal
MoTe₂ and magnetoelectric effect
of Ba₂CuGe₂O₇
February 2021**

RYOTA ONO

Graduate School of
Science and Engineering
CHIBA UNIVERSITY

(千葉大学審査学位論文)

**Theoretical studies on spintronics
materials: Angle-resolved
photoemission of Weyl semimetal
MoTe₂ and magnetoelectric effect
of Ba₂CuGe₂O₇
February 2021**

RYOTA ONO

Graduate School of
Science and Engineering
CHIBA UNIVERSITY

Contents

I	Angle-resolved photoemission calculations of MoTe₂	1
1	Introduction	3
2	Theory of Photoelectron Spectroscopy	5
2.1	Photoelectron Spectroscopy (PES)	5
2.2	Photoemission three-step model	5
2.3	Photoemission one-step model	9
2.4	General remarks of ARPES	10
2.5	Selection rule	11
2.6	Final state plane-wave approximation	14
2.7	Matching method	15
3	Topological materials	17
3.1	Topological insulator	17
3.2	Topological semimetals	18
3.3	Weyl semimetal	18
3.4	Type-I and Type-II Weyl semimetal	20
3.5	TaAs as the first type-I Weyl semimetal	21
3.6	WTe ₂ and MoTe ₂ as the first type-II Weyl semimetal	22
4	Interpretations of the photocurrent intensities	25
4.1	A graphene-like box-potential	26
4.2	MoTe ₂	29
4.2.1	Calculation details	30
4.2.2	Band structure of MoTe ₂ (T _d)	31
4.2.3	Orbital projection and polarization dependence	32
4.2.4	Comparison with an experiment	37
4.3	Conclusion and future prospect	37
II	Theory of magnetoelectric effect in Ba₂CuGe₂O₇	41
5	Introduction	43
6	Multiferroics and magnetoelectric effect	47
6.1	Linear magnetoelectric effect	47
6.2	Ferroelectricity induced by magnetic orders (Giant magnetoelectric effect)	48

6.3	Microscopic mechanisms of the magnetically induced ferroelectricity	48
6.4	Examples of multiferroic materials	52
6.4.1	YMnO ₃	52
6.4.2	TbMnO ₃	53
6.4.3	CuFeO ₂	54
7	Theory for strongly correlated materials	57
7.1	Hubbard model	57
7.1.1	One-electron part in d-orbital case	59
7.2	Wannier function	59
7.2.1	Maximally localized Wannier function	60
7.2.2	Selectively localized Wannier function	62
7.2.3	Modified maximally localized Wannier function	62
7.3	Constrained Random Phase Approximation	63
7.3.1	Practical case	64
7.4	Spin Hamiltonian	65
7.4.1	Heisenberg model	66
7.4.2	Dzyaloshinskii-Moriya interaction	68
7.5	Superexchange theory in spin $\frac{1}{2}$ systems	72
7.6	Berry phase (Wannier) expression for the macroscopic electronic polarization	75
7.7	Superexchange theory for the magnetoelectric effect	77
7.8	Spin-current Mechanism	78
8	Magnetoelectric effect of a spiral magnet Ba₂CuGe₂O₇	81
8.1	Multiferroic Ba ₂ CuGe ₂ O ₇	81
8.2	Symmetric property of Ba ₂ CuGe ₂ O ₇	83
8.3	Electronic structure	87
8.4	Nonexistence of single ion contributions in spin 1/2 system	88
8.5	5-orbital model	91
8.5.1	Spin spiral state	92
8.5.2	Without SOC	94
8.5.3	Ferroelectricity	95
8.5.4	Response to external fields in collinear C-type AFM phase	99
8.6	Conclusion and future prospect	101
9	Summary	103
	Acknowledgements	115

Abstract

This thesis mainly accesses theoretical analysis of Angle-Resolved-Photoelectron Spectroscopy (ARPES) of a transition metal dichalcogenides MoTe_2 by using one-step calculation and magnetically induced magnetoelectric (ME) effect of $\text{Ba}_2\text{CuGe}_2\text{O}_7$ by using superexchange (SE) theory.

Concerning the first part, this thesis describes present theoretical methods which are sometimes used to understand the ARPES intensity. ARPES is an experimental technique for observing electronic band structure of the materials. Peaks of the observed ARPES spectra represent electronic structure of the material. Most often, only the peak position (band dispersion) is focused. However, this thesis focus not only on the peak position, but also on the ARPES intensity which contains important physical information. Namely, spectra are depending on the experimental condition (e.g. light polarization, photon energy) and relations between ARPES responses and physical properties of the materials are not so clear. This thesis investigates the ARPES intensities of MoTe_2 theoretically. Transitional metal dichalcogenides MoTe_2 in T_d phase is a candidate material of the so-called Weyl semimetal which has energy dispersion of the Weyl fermion. Therefore, there are some ARPES experiment done to this material until now. However, clear experimental evidence of Weyl semimetallicity of this material is lacking. This thesis reveals the specific bands for the Weyl semimetal (hole and electron pocket) can be selected in ARPES by choosing suitable experimental settings and which can be qualitatively explained by initial state with dipole selection rule. After the investigation, this thesis suggests suitable experimental settings for future ARPES experiments in order to better investigate the Weyl semimetallicity of the material.

Concerning the latter part, this thesis suggests so-called SE theory for the electronic polarization and applies the theory to unveil the mechanism of the magnetically induced ME effect of a multiferroic material $\text{Ba}_2\text{CuGe}_2\text{O}_7$. ME effect is a cross effect of usual response to the external fields. Namely, external magnetic (electronic) fields induce some ferroelectric (magnetic) order. Thus, one can control electronic polarization by the external magnetic field. The SE theory is well established theory for describing the magnetic energy of Mott insulators. Since the electronic polarization is a property of insulating materials, an extension of the SE theory of the Mott insulator to the electronic polarization has been performed. Then, the theory has successfully been applied to a controversial multiferroic spiral magnet $\text{Ba}_2\text{CuGe}_2\text{O}_7$. The theory qualitatively describes its experimental behavior. In addition to those, the theory predicts in-plane electronic polarization induced by the out-of-plane external magnetic field which has been overlooked.

List of Abbreviations

AFM	AntiFerroMagnet
ARPES	Angle-Resolved PhotoEmission Spectroscopy
ASA	Atomic Sphere Approxiamtion
cRPA	constrained Random Phase Approximation
DFT	Density Functional Theory
DM	Dzyaloshinskii-Moriya
DOS	Density Of States
IMFP	Inelastic scattering Mean Free Path
KKR	Korringa-Kohn-Rostoker
LDA	Local Density Approximation
LKKR	Layered Korringa-Kohn-Rostoker
ME	MagnetoElectric
MLWF	Maximally Localized Wannier Function
MST	Multiple Scattering Theory
PAW	Projector-Augumented Wave
PBE	Perdew-Burke-Ernzerhof
PDOS	Projected Density Of States
PES	PhotoEmission Spectroscopy
PWA	Plane-Wave Approximation
RPA	Random Phase Approximation
SE	SuperExchange
SLWF	Selectively Localized Wannier Function
SOC	Spin Orbit Coupling
SPR-KKR	Spin Polarized Relativistic-Korringa-Kohn-Rostoker
TMDC	Transitional Metal DichalCogenides
TRIM	Time-Reversal Invariant Momenta
VASP	Vienna-Abinitio-Simulation-Package

Part I

Angle-resolved photoemission calculations of MoTe₂

Chapter 1

Introduction

Angle-Resolved Photoelectron Spectroscopy (ARPES) has been extensively used to measure kinetic energies of the electrons in materials. The measurement method itself has quite a long history. Recently, the accuracy of ARPES is growing very fast and become more efficient. For example, time derivations of the ARPES (time-resolved ARPES), which capture ultrafast phenomena, are receiving much attention recently. Usually, ARPES measurements are performed to observe kinetic energy angle distributions of the electrons and thus draws band structures of the materials. In addition to the band dispersions, it is widely believed that the intensities obtained from the ARPES measurements have rich information (e.g., orbital character of the band structures). Indeed, an efficient interpretation of the ARPES intensities is suggested by Puschnig et al. [1] through a simple plane-wave approximation. However, it should be noted that the approximation used in their work is quite limited. In the plane-wave approximation, the ARPES final state is approximated as a single plane-wave. Meanwhile, the correct final state wave function should have a more complicated wave function, approximated as a plane-wave at enough distant points from the substances. Besides the plane-wave approximation, another efficient approach is called Layered Korringa-Kohn-Rostoker (LKKR) method [2–5]. The method uses advantages of the multiple scattering theory, and thus, one can have correct final states of ARPES since the multiple scattering theory can include all the scattering processes. However, the accuracy of the multiple scattering theory remains questionable when the material is a complex system. For these reasons, an efficient calculation method for ARPES is needed.

The first part accesses a new efficient calculation method for ARPES, which can be combined with very well established and used plane-wave basis Density Functional Theory (DFT). The plane-wave DFT method is believed to provide accurate electronic structure except for strongly correlated systems (in strongly correlated systems, many-body effects can not be neglected). Therefore, a new method is expected to provide accurate results even for complex systems. The validity of the new method will be discussed in Chap. 4 within a one-dimensional potential well which is fitted to have a graphene-like electronic structure.

Since the first observation of the physics of a topological insulator in HgTe [6], the exploration of new topological materials is extensively being performed. In topological materials, edge states (in other words, "surface" in

3D materials) are crucial. The edge states in topological materials show peculiar band structures. Therefore, dedicate ARPES measurements have been performed in such candidate topological materials recently. One interesting example of a topological material is Weyl semimetals. In Weyl semimetals, quasi Weyl fermion, which has not been observed in nature, is expected to exist at the edge states of the materials. The potential existence of the Weyl fermions gives expectations of interesting physical phenomena such as chiral anomaly, which will not be touched deeply in this thesis. Readers interested in it can read papers about it, e.g. [7–10]. The meaning of ARPES intensities in such material will be discussed in Chap. 4.

This first part of the thesis is structured as follows. Chap. 2 discusses basic concepts and shows new calculation methods for the exact final states from plane-wave DFT codes. The next Chap. 3 briefly shows how quasi Weyl fermions are rationalized in substances such as TaAs and WTe₂, which are nowadays found as the possible realization of two types of Weyl semimetals. Finally, Chap. 4 examines new theory of the ARPES calculation for the one-dimensional periodic potential well. After that, the efficient interpretation of ARPES intensity will be discussed with respect to one of the popular topological material Weyl semimetal MoTe₂.

Chapter 2

Theory of Photoelectron Spectroscopy

2.1 Photoelectron Spectroscopy (PES)

To understand physical properties of the materials, it is important to know the electronic structures of the materials [11]. In such situations, Angle-Resolved Photoelectron Spectroscopy (ARPES) is quite useful. ARPES is one of the experimental method of Photoelectron Spectroscopy (PES). Before speaking of ARPES, this section describes basic theory of PES. PES has quite long history and thus quite old technique. The first development of PES has been done by H. Hertz [12] and which is done just by emitting lights towards the target substances and detect the energies of the excited electrons (See Fig. 2.1 for a simple cartoon of the experimental setup). The basis of the PES has been explained from theoretical point of view by A. Einstein [13]. The most important parameter of the PES experiments is the kinetic energy of the electrons in the substances. From the energy conservation law, one can determine the kinetic energies as

$$E_{kin} = \hbar\omega - \Phi - |E_B|, \quad (2.1)$$

where $\hbar\omega$ is the photon energy of the light, Φ is the work function (corresponding the energy needed to take electrons from the substances) and $|E_B|$ is a binding energy of the electrons. Therefore one can determine the binding energy of the electron from obtained kinetic energy in the PES experiments. A common setting of the binding energies consists in taking $E_B = 0$ as the Fermi level. A simple picture of the PES processes is that a photon impinges on a substance, then through the photoelectric effect, an electron is excited and escapes to the vacuum. The detector detects the electron. Following sections describe more detailed interpretations of the photoexcited processes which are useful for understanding the experimental results and theoretical modelings of PES.

2.2 Photoemission three-step model

Photoemission three-step model has been recognized as one of the efficient phenomenological interpretation of the PES process. The main concept of

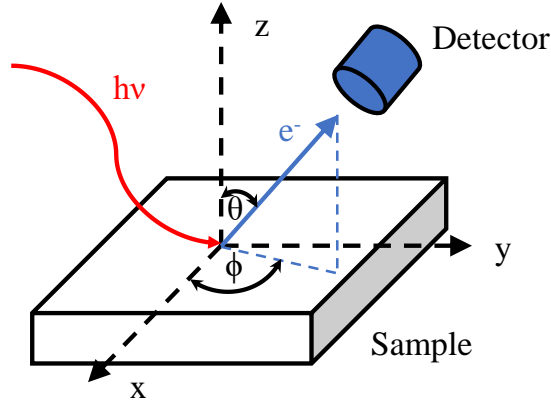


FIGURE 2.1: A schematic drawing of (Angle-resolved) PES experiments. θ and ϕ are a polar and azimuthal angle of the emitted electron which is excited by a light with photon energy of $h\nu$.

this three-step model is that splitting the whole process into following three parts (the process is depicted in Fig. 2.2(a)):

① *Excitation of a photoelectron*

The photon excite a N -electron initial (ground) state $|\psi_i^N\rangle$ to a final (excited) state $|\psi_f^N\rangle$. In the limits of the independent particle approximation, this excitation is understood as a dipole transition. The energy conservation law during this process is estimated as

$$E_f = \hbar\omega + E_i \quad (2.2)$$

where E_f is the final state energy and E_i is the initial state energy. By taking the energy gain from the excisions as a perturbation, one can have transition rate as the well known Fermi's golden rule:

$$w_{i \rightarrow f} = \frac{2\pi}{\hbar} |\langle \psi_f^N | H_{\text{int}} | \psi_i^N \rangle|^2 \delta(E_f^N - E_i^N - \hbar\omega). \quad (2.3)$$

The Hamiltonian H_{int} is a Hamiltonian of electron-photon interaction which is given by

$$H_{\text{int}} = \frac{e}{2mc} (\mathbf{A} \cdot \mathbf{p} + \mathbf{p} \cdot \mathbf{A}) = -\frac{e}{mc} \mathbf{A} \cdot \mathbf{p} \quad (2.4)$$

here the two photon process $\mathbf{A} \cdot \mathbf{A}$ (which is considered very weak effect) is ignored and the relation $\mathbf{A} \cdot \mathbf{p} + \mathbf{p} \cdot \mathbf{A} = 2\mathbf{A} \cdot \mathbf{p} + i\hbar(\nabla \cdot \mathbf{A})$ is used with the Coulomb gauge $\text{div} \mathbf{A} = \nabla \cdot \mathbf{A} = 0$. By making use of the Slater determinants, one can reduce the N -electron problem to one-electron problem $\langle \psi_f^N | H_{\text{int}} | \psi_i^N \rangle \rightarrow \langle \phi_f | H_{\text{int}} | \phi_i \rangle$. This expression now

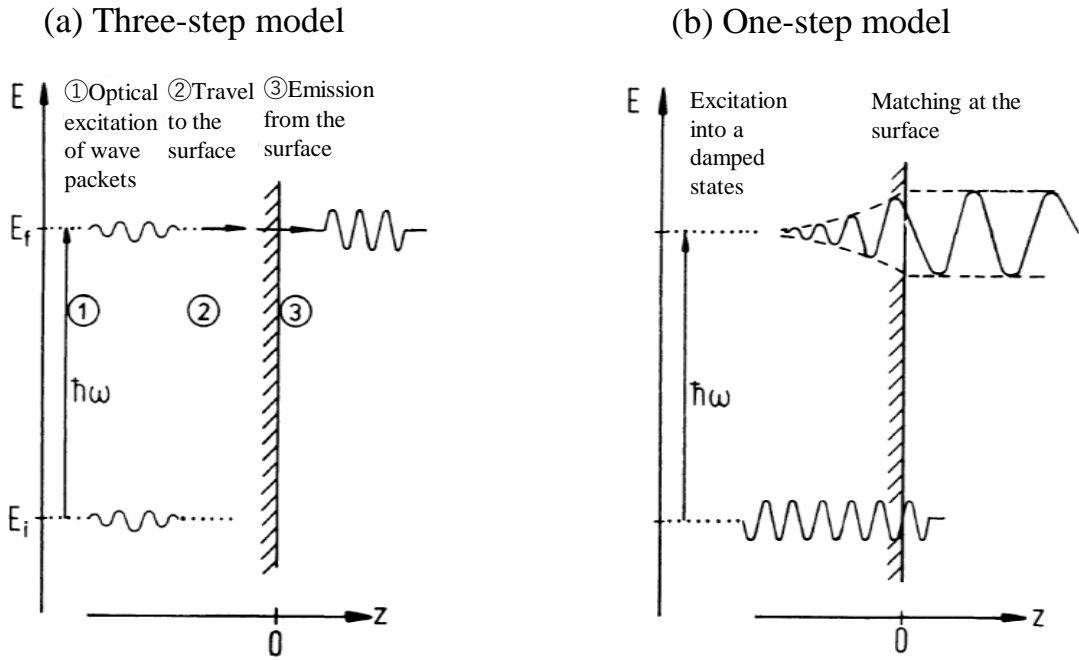


FIGURE 2.2: Picture of (a)the three-step model and (b)the one-step model. The figure is adopted from [11].

allows us to estimate the photocurrent intensities in the solids as

$$I(\hbar\omega) \propto |\langle \phi_f | H_{int} | \phi_i \rangle|^2 \delta(E_f - E_i - \hbar\omega) = |M_{fi}|^2 \delta(E_f - E_i - \hbar\omega). \quad (2.5)$$

The most important term M_{fi} is known as the optical transition matrix element. Furthermore, the Hamiltonian H_{int} can be simplified with an approximation which will be shown below. The Hamiltonian Eq. 2.4 can be further rewritten as

$$H_{int} = -\frac{e}{mc} A_0 \epsilon \cdot \mathbf{p} e^{i(\mathbf{k} \cdot \mathbf{r} - \omega t)} \quad (2.6)$$

where ϵ and A_0 are polarization vector and amplitudes, respectively. Taylor expansion of $e^{i\mathbf{k} \cdot \mathbf{r}}$ is given by

$$e^{i\mathbf{k} \cdot \mathbf{r}} = 1 + i\mathbf{k} \cdot \mathbf{r} - \frac{1}{2}(\mathbf{k} \cdot \mathbf{r})^2 + \dots \quad (2.7)$$

Using only the first term of Eq. 2.7 in the Hamiltonian is called dipole approximation. With the dipole approximation, the transition matrix element M_{fi} can be approximated as

$$M_{fi} \approx -\frac{e}{mc} A_0 e^{-i\omega t} \langle \phi_f | \epsilon \cdot \mathbf{p} | \phi_i \rangle. \quad (2.8)$$

With a commutation relation

$$[H_0, \mathbf{r}] = \frac{im}{\hbar} \mathbf{p}, \quad (2.9)$$

leads Eq. 2.8 to a simple form as

$$M_{fi} = -\frac{ie}{\hbar c} A_0 e^{-i\omega t} \langle \phi_f | \boldsymbol{\epsilon} \cdot [H_0, \mathbf{r}] | \phi_i \rangle \quad (2.10)$$

$$= -\frac{ie}{\hbar c} (E_f - E_i) A_0 e^{-i\omega t} \langle \phi_f | \boldsymbol{\epsilon} \cdot \mathbf{r} | \phi_i \rangle \quad (2.11)$$

$$= -\frac{ie\omega}{c} A_0 e^{-i\omega t} \langle \phi_f | \boldsymbol{\epsilon} \cdot \mathbf{r} | \phi_i \rangle. \quad (2.12)$$

As a consequence, the photocurrent intensities are represented as

$$I(\hbar\omega) \propto |\langle \phi_f | \boldsymbol{\epsilon} \cdot \mathbf{r} | \phi_i \rangle|^2 \delta(E_f - E_i - \hbar\omega) \quad (2.13)$$

within the dipole approximation.

② Transport of the excited photoelectron to the surfaces

As the second process, the photoelectrons excited in the solids travel to the surface of the solids. During this process, the excited photoelectrons will be mainly scattered by other electrons reside in the solids as inelastic scatterings. The inelastic scattering mean free path (IMFP) gives an idea how far the electrons travel on average in the solid before they loses the kinetic energy. According to D. R. Penn [14] Inverse of the IMFP $\lambda^{-1}(E)$ is given by

$$\lambda^{-1}(E) = \int_0^{(E-E_F)/\hbar} d\omega \tau(E, \omega), \quad (2.14)$$

where $\tau(E, \omega)$ is the inverse of a differential mean free path which is given via imaginary parts of dielectric functions as

$$\tau(E, \omega) = \frac{\hbar}{a_0 \pi E} \int_{q^-}^{q^+} \frac{dq}{q} \text{Im} \left(\frac{-1}{\epsilon(q, \omega)} \right). \quad (2.15)$$

The term $\text{Im}(-1/\epsilon)$ is called energy loss function and q^\pm are the transfer limits are given from the condition

$$\hbar\omega \leq E_{\mathbf{k}} - E_{\mathbf{k}-\mathbf{q}} = \frac{\hbar^2}{2m} (2kq - q^2), \quad (2.16)$$

which gives $q^\pm = k[1 \pm \sqrt{1 - (\hbar\omega/E_{\mathbf{k}})}]$ [14].

③ Emissions of the photoelectrons to the vacuum

The last step is the emission into vacuum of the photoelectrons that reached the surface. The emitted electron will be detected by a detector which measures kinetic energies of the electrons E_{kin} . Then the binding

energy is calculated from the conservation law Eq. 2.1. The detected electrons in the vacuum conserve reciprocal vectors parallel to the surface after the emission.

2.3 Photoemission one-step model

Another model along the same line is also used widely which is called one-step model firstly developed by J. B. Pendry in 1976 [15]. In the one-step model, all scattering events after the excitation of the electrons are included. Therefore, in the process, the excited damped final states are smoothly matched at the surface with a plane wave (Fig. 2.2(b)). Theoretical realization of the model can be achieved via multiple scattering theory and thus, Green's functions as will be shown in the following.

The general form of the transition rate is expressed as

$$w_{i \rightarrow f} = \frac{2\pi}{\hbar} |\langle \psi_f^N | \Delta | \psi_i^N \rangle|^2 \delta(E_f^N - E_i^N - \hbar\omega) \quad (2.17)$$

from Eq. 2.3 with a new notation for the perturbation Δ .

The perturbation Δ can be represented by the second quantization as

$$\Delta = \sum_{\alpha\beta} \Delta_{\alpha\beta} c_{\alpha}^{\dagger} c_{\beta} \quad (2.18)$$

where $\Delta_{\alpha\beta}$ is one-electron matrix elements of electron-photon interaction between one-particle states ϕ_{α} and ϕ_{β} . From this point, the initial and the final states are defined as $|\psi_i^N\rangle = |\psi_0^N\rangle$ and $|\psi_f^N\rangle = c_f^{\dagger} |\psi_s^{N-1}\rangle$ with N-electron ground states $|\psi_0^N\rangle$ and N-1 electron excited states $|\psi_s^{N-1}\rangle$. So-called sudden approximation is used at this point which means the interactions between an excited electron and the remaining N-1 electrons are ignored which is also shown as $c_f |\psi_0^N\rangle = 0$. Then the transition probability Eq. 2.17 is rewritten as

$$w_s = \frac{2\pi}{\hbar} |\langle \psi_s^{N-1} | \sum_{\alpha\beta} \Delta_{\alpha\beta} c_f c_{\alpha}^{\dagger} c_{\beta} | \psi_0^N \rangle|^2 \delta(E_s^N - E_0^N - \hbar\omega). \quad (2.19)$$

With the above expression, the photocurrent intensities are evaluated as

$$I(\hbar\omega) = \sum_s w_s = \sum_{\alpha\beta} \Delta_{f\alpha}^{\dagger} A_{\alpha\beta}(E_0^N) \Delta_{\beta f}. \quad (2.20)$$

The one-electron spectral function $A_{\alpha\beta}$ can further be represented as

$$A_{\alpha\beta} = -\frac{1}{\pi} \text{Im} G_{\alpha\beta}^R \quad (2.21)$$

with a retarded Green's function $G_{\alpha\beta}^R$. Therefore, one obtains

$$I(\hbar\omega) = -\frac{1}{\pi} \text{Im} \sum_{\alpha\beta} \Delta_{f\alpha}^\dagger G_{\alpha\beta}^R(E_0^N) \Delta_{\beta f}. \quad (2.22)$$

With a relation for the one-electron retarded Green's function G^R

$$G^R(E_0^N) = \sum_{\alpha\beta} |\phi_\alpha\rangle G_{\alpha\beta}^R(E_0^N) \langle\phi_\beta|, \quad (2.23)$$

thus we finally have a well known formula as the one-step photoemission

$$I(\hbar\omega) = -\frac{1}{\pi} \text{Im} \langle\phi_f|\Delta^\dagger G^R(E_0^N)\Delta|\phi_f\rangle. \quad (2.24)$$

In addition to above expressions, for the dipole approximation one can use $\Delta \approx \epsilon \cdot r$.

2.4 General remarks of ARPES

The word "Angle-Resolved" comes from the experimental setup of ARPES. ARPES experiments are performed by changing the angle of the light (Fig. 2.1). Then, a detector observes the angle distributions of the photocurrent intensities. Reciprocal vector of the free electron state in the vacuum \mathbf{K} and in the solid \mathbf{k} obey a conservation law for the parallel components (Fig. 2.3)

$$k_{\parallel} = K_{\parallel} = |\mathbf{K}| \sin \theta = \frac{\sqrt{2m_e E_{\text{kin}}}}{\hbar} \sin \theta. \quad (2.25)$$

For vertical component K_{\perp} and k_{\perp} , such conservation law is no longer applicable. Instead, k_{\perp} can be evaluated by an energy conservation law

$$E_{\text{kin}} = \frac{\hbar^2}{2m_e} (k_{\perp}^2 + k_{\parallel}^2) - V_0, \quad (2.26)$$

where V_0 is called inner-potential meaning determined as the bottom of approximated potential wells. In other words, it is known as the muffin-tin zero. Eq. 2.26 leads to

$$k_{\perp} = \frac{\sqrt{2m_e (E_{\text{kin}} \cos^2 \theta - V_0)}}{\hbar}, \quad (2.27)$$

therefore, from the ARPES, one can have \mathbf{k} -resolved photocurrent intensities whose peaks represent energy levels. Thus ARPES provides complete information about the electronic structures.

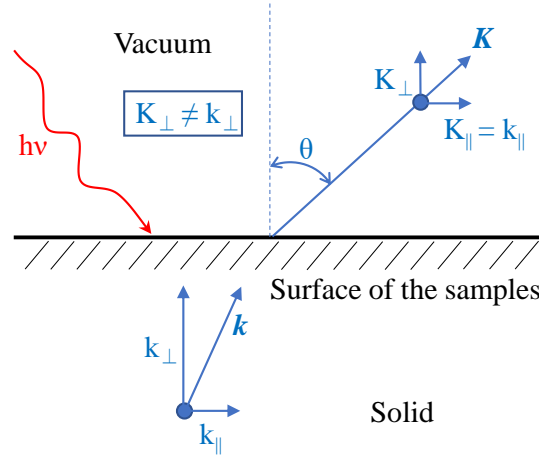


FIGURE 2.3: Picture of momentum conservation law in ARPES experiments.

2.5 Selection rule

As we saw in the previous sections, calculating the photocurrent intensities are quite complicated tasks. For the initial state, first-principle calculations provide quite good wave functions. On the other hand, final states are still difficult to compute. Since the final states have very complicated process in the bulk, some approximation give qualitative description of the final states. This section shows that analysis of symmetries of the wave functions of the transition matrix elements which makes the physics behind the intensities a little bit transparent.

First, let's think of the transition matrix elements in the dipole approximation Eq. 2.13. Parities of the functions inside the integrals give a restriction for the wave functions choices. The only possible transition in the dipole approximation is odd \rightarrow even or vice versa, because the position operator \mathbf{r} is odd.

As the next step, consider atomic wave functions form products of Radial wave functions $R_{nl}(\mathbf{r})$ and Spherical harmonics $Y_{lm}(\theta, \phi)$ as $\phi_{nml} = R_{nl}(\mathbf{r})Y_{lm}(\theta, \phi)$. The spherical harmonics can be further written as

$$Y_{lm}(\theta, \phi) = (-1)^{(m+|m|)/2} \sqrt{\frac{2l+1}{2} \frac{l-|m|}{l+|m|}} P_l^{|m|}(\cos \theta) \frac{1}{\sqrt{2\pi}} e^{im\phi}, \quad (2.28)$$

where $P_l^{|m|}(\zeta)$ is a Legendre polynomial defined as

$$P_l^{|m|}(\zeta) = (1-\zeta^2)^{\frac{|m|}{2}} \frac{d^{|m|}}{d\zeta^{|m|}} P_l(\zeta) \quad (2.29)$$

with

$$P_l(\zeta) = \frac{1}{2^l l!} \frac{d^l}{d\zeta^l} (\zeta^2 - 1)^l. \quad (2.30)$$

The spherical harmonics for $-m$ is then given by

$$Y_{l-m}(\theta, \phi) = (-1)^m Y_{lm}(\theta, \phi)^*. \quad (2.31)$$

Next step is to think of the parity inversion of the spherical harmonics. The parity inversion of the spherical coordinate is achieved by changing the polar angle $\theta \rightarrow \pi/2 - \theta$ and azimuthal angle $\phi \rightarrow \phi + \pi$ (Fig. 2.4). As for the ϕ -dependent part of $Y_{lm}(\theta, \phi)$, one has $\Phi_m(\phi + \pi) = (-1)^m \Phi_m(\phi)$. For the θ -dependent part, using the relation

$$P_l^{|m|}(-\zeta) = (-1)^{l+m} P_l^{|m|}(\zeta), \quad (2.32)$$

it follows $\Theta_l^m(\pi/2 - \theta) = (-1)^{l+m} \Theta_l^m(\theta)$. As a consequence, parity inversion of the spherical harmonics gives

$$Y_{lm}\left(\frac{\pi}{2} - \theta, \phi + \pi\right) = (-1)^l Y_{lm}(\theta, \phi). \quad (2.33)$$

This simply implies difference of two l -quantum numbers Δl to be odd to the matrix elements Eq. 2.13 have non-zero values. So far, the selection constraint is $\Delta l = l' - l$ to be odd. Followings show that this constraint can be more limited.

By writing the integral more explicit, the transition matrix elements are given by

$$\int \phi_{l'm'n'}^* \boldsymbol{\epsilon} \cdot \mathbf{r} \phi_{lmn} d\mathbf{r} \quad (2.34)$$

$$= AB \int_0^{2\pi} \int_0^\pi \boldsymbol{\epsilon} \cdot \hat{\mathbf{r}} P_{l'}^{|m'|}(\cos \theta) P_l^{|m|}(\cos \theta) e^{i(m-m')\phi} \sin \theta d\theta d\phi, \quad (2.35)$$

where $\phi_{l'm'n'}$, ϕ_{lmn} , A and B are the final state wave function, the initial state wave function, some coefficient and the radial integral term. The term for a z component of the polarization vector $\boldsymbol{\epsilon} = (\epsilon_x, \epsilon_y, \epsilon_z)$ is

$$\int \phi_{l'm'n'}^* \epsilon_z \cos \theta \phi_{lmn} d\mathbf{r} \quad (2.36)$$

$$= AB \int_0^\pi \sin \theta \cos \theta P_{l'}^{|m'|}(\cos \theta) P_l^{|m|}(\cos \theta) d\theta \int_0^{2\pi} e^{i(m-m')\phi} d\phi \quad (2.37)$$

which gives a condition $m' = m$. The condition leads Eq. 2.37 to following form:

$$2\pi AB \int_{-1}^1 z P_{l'}^{|m|}(z) P_l^{|m|}(z) dz. \quad (2.38)$$

By substituting following recursion formula for the Legendre polynomials

$$zP_l^{|m|}(z) = \frac{l-m+1}{2l+1}P_{l+1}^{|m|}(z) + \frac{l+m}{2l+1}P_{l-1}^{|m|}(z) \quad (2.39)$$

$$= aP_{l+1}^{|m|}(z) + bP_{l-1}^{|m|}(z) \quad (2.40)$$

one obtains

$$2\pi AB \int_{-1}^1 P_{l'}^{|m|}(z) \left(aP_{l+1}^{|m|}(z) + bP_{l-1}^{|m|}(z) \right) dz. \quad (2.41)$$

The orthogonality of the Legendre polynomials give the condition $\Delta l = \pm 1$ with $m' = m$. This is well known selection rule for the optical transitions. As for the x and y component of the transition matrix elements, same condition for Δl ($\Delta m = \pm 1$ for Δm) can be obtained by making use of $\cos \phi = (e^{i\phi} + e^{-i\phi})/2$ and $\sin \phi = (e^{i\phi} - e^{-i\phi})/2i$. As a summary, following conditions are implied to the matrix elements to have non-zero values

$$\Delta l = l' - l = \pm 1 \quad \text{and} \quad \Delta m = m' - m = \pm 1 \quad (\text{for } x \text{ and } y) \quad m' = m \quad (\text{for } z). \quad (2.42)$$

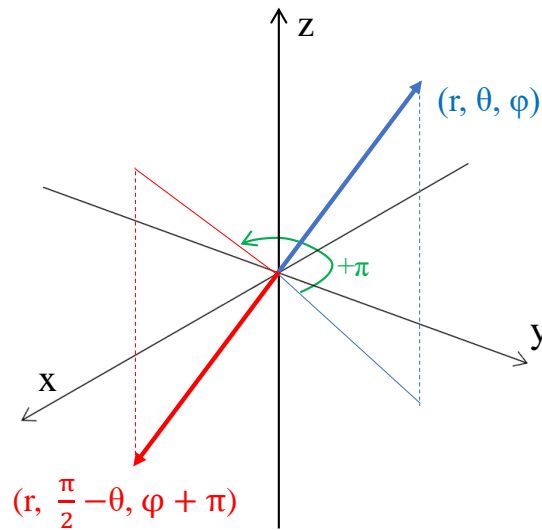


FIGURE 2.4: Inversion operation of the spherical coordinate.

2.6 Final state plane-wave approximation

Even if the photocurrent intensity can be calculated by Eq. 2.5, the final state wave function $|\phi_f\rangle$ is left nontrivial task. Because of this difficulty, the photocurrent intensity is not investigated well and even if one tries to investigate it, strong approximations are needed. This section describes a simple and efficient approximation for the final state wave functions (which is called final state plane-wave approximation) which is frequently used in theoretical analysis due to its simplicity. The approximation is simply called plane-wave approximation in this section. The plane-wave approximation is has been made popular by P. Puschnig et al. [1, 16] to describe the angle dependence of the photocurrent intensities. With the plane-wave approximation, they found the photocurrent intensities map represents molecular orbital densities of sexiphenyl and pentacene molecule (Fig. 2.5). From that time, the plane-wave approximation has been recognized as a very simple, but efficient approximation.

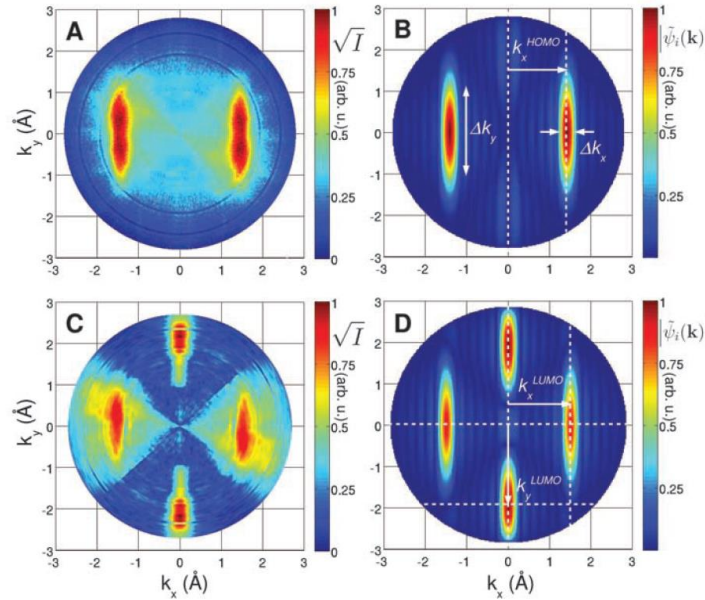


FIGURE 2.5: ARPES intensity angle distribution of (A, B) measurements (C, D) calculated from PW approximation for sexiphenyl. (A) With binding energy $E_B = 1.9$ eV. (B) Corresponding to (A). (C) With binding energy $E_B = 0.3$ eV. (D) Corresponding to (C).

In the plane-wave approximation, the final state wave function is simply approximated as a plane wave $|\phi_f\rangle = |\mathbf{p}'\rangle = |\mathbf{k}' + \mathbf{G}'\rangle$ (Fig. 2.6). If one use a linear combination of plane-wave (plane-wave basis) as the initial state wave function $|\phi_i\rangle = |n\mathbf{k}\rangle = \sum_{\mathbf{G}} C_{n\mathbf{k}}^{\mathbf{G}} |\mathbf{k} + \mathbf{G}\rangle$, the form becomes more simple and transparent. The transition matrix elements are then given by

$$M_{fi} = \langle \phi_f | \mathbf{A} \cdot \hat{\mathbf{p}} | \phi_i \rangle = \langle \mathbf{p}' | \mathbf{A} \cdot \hat{\mathbf{p}} | n\mathbf{k} \rangle = \mathbf{A} \cdot \mathbf{p} C_{n\mathbf{k}}^{\mathbf{G}} |_{\mathbf{p}=\mathbf{k}+\mathbf{G}}. \quad (2.43)$$

Therefore, in the plane-wave approximation, possible final state is only $\mathbf{p}' = \mathbf{p} = \mathbf{k} + \mathbf{G}$.

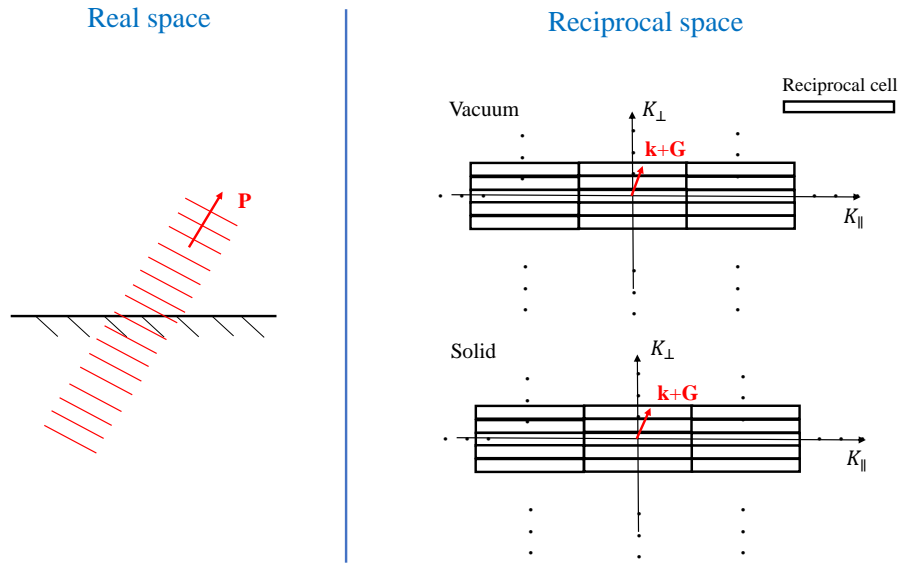


FIGURE 2.6: Image of the final state plane-wave approximation in real space (left) and in reciprocal space (right).

2.7 Matching method

Despite the success of the plane-wave approximation, the plane-wave approximation is insufficient in many cases and cannot elucidate many phenomena such as circular dichroism in angular distributions [17]. Multiple scattering theory (MST) gives exact one-step final state wave functions, however, the accuracy of the MST is questionable because of the muffin-tin approximations for the crystal potential, which is generally used in combinations with MST. One of the merits of the plane-wave approximation is that the initial states can be taken as plane-wave basis set which is widely used in DFT [18]. One of the possible procedures is making a linear combination of possible final states and then, fit coefficients to be a plane-wave at the boundary between surface and vacuum. Such an approach is introduced in [19]. This approach simply matches the linearized final state wave function and a plane-wave at the boundary, hence it is simply called Matching method from this point. Practical procedure will be explained below.

To achieve a numerically exact final state wave function (Fig. 2.7), assume

a linear combination of possible states (the energy and parallel crystal momentum k_{\parallel} are conserved). The linear combination is given as

$$\phi_f(\mathbf{r}) = \sum_{\gamma} \alpha_{\gamma} \phi_{\gamma}(\mathbf{r}) \quad (2.44)$$

where γ is a combined index of bands n and wave vectors \mathbf{k} and the sum runs over all possible states. The coefficient α_{γ} is determined by the boundary condition of surface where the combined final state coincides with a plane-wave. For the smooth matching, the value and its first derivative will be matched at the boundary. The conditions are given by

$$\begin{cases} \sum_{\gamma} \alpha_{\gamma} \phi_{\gamma}(\mathbf{r}') = \exp(i\mathbf{p} \cdot \mathbf{r}') \\ \sum_{\gamma} \alpha_{\gamma} \nabla \phi_{\gamma}(\mathbf{r})|_{\mathbf{r}=\mathbf{r}'} = i\mathbf{p} \exp(i\mathbf{p} \cdot \mathbf{r}') \end{cases} \quad (2.45)$$

where \mathbf{r}' is the position of the boundary between surface and vacuum which can be presumably taken at the middle of the vacuum region between the repeated slabs in slab model calculations. As a consequence, Eq. 2.45 is the equation to be solved to obtain good final state wave functions.

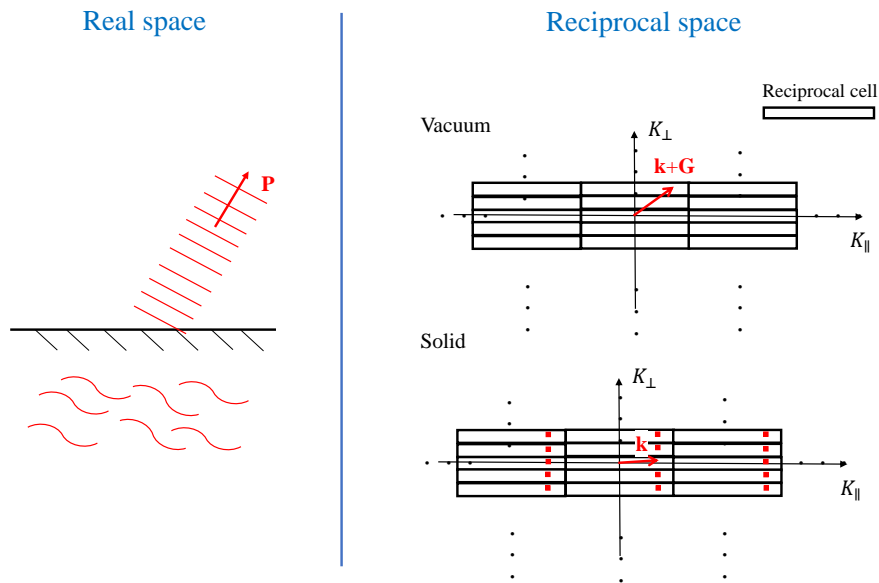


FIGURE 2.7: Image of the numerically exact ARPES final state wave function in real (left) and reciprocal (right) space.

Chapter 3

Topological materials

3.1 Topological insulator

Topological insulators are materials which are insulators in the bulk, but have gap-less states at their edges. In normal insulators, the edge states coming from the conduction bands come back to the conduction bands. On the other hand, edge states of the topological insulators connect conduction and valence bands (See Fig. 3.1). It should be noted that even if the insulator has gap-less states, it can be a normal insulator. The word "topological" means even if the form of the edge states are varied for some reasons, it still has gap-less edge states. This feature does not depend on the details of the edge states. Thus it is robust against perturbations from impurities. Insulators can be characterized by so called topological Z_2 number. This topological Z_2 number can be computed from parities at time-reversal invariant momenta (TRIM) [20]. In normal insulators, Z_2 number is even. By contrast, topological insulators have odd Z_2 numbers.

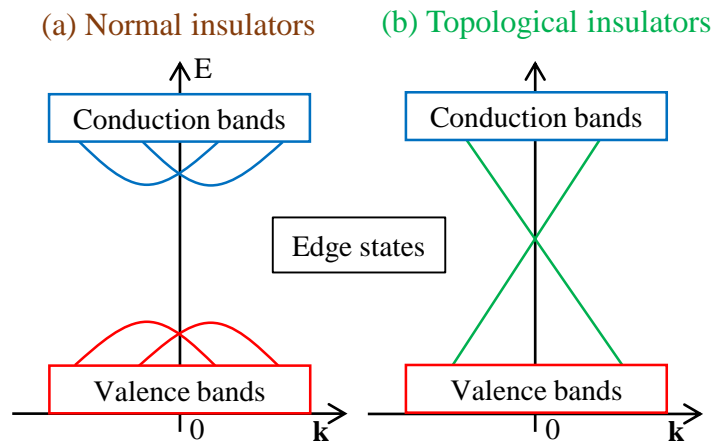


FIGURE 3.1: Cartoon of band structure of the edge states in (a)Normal insulators and (b)Topological insulators.

3.2 Topological semimetals

Only topological insulators have been focused so far, however, there is another interesting topological material family which is called topological semimetal [21]. In such materials, gapless edge states, in other words, the states where conduction and valence bands degenerate form point or line in k -space. There are various reasons of these degeneracies. Fig. 3.2 shows typical three types of topological semimetals ((a)Dirac semimetal, (b)Weyl semimetal, (c)Nodal line semimetal). (a) and (b) have cone like band structure which is called Dirac cone. Difference between (a) and (b) is that in (b)Weyl semimetals, the Dirac cone is non-degenerate, while it is degenerating with respect to spin in (a)Dirac semimetal (Kramers degeneracy). This degeneracy can occur when the system is invariant under the product operation of time-reversal operation and parity operation. Making a long story short, if the system has broken either time-reversal or parity, it becomes (b)Weyl semimetal. In (c)Nodal line semimetals, these bands are degenerating around a curve which is called Nodal line. One can have such Nodal lines for example when time-reversal and parity symmetry coexist with small spin-orbit interactions (can be ignored). Since later chapters are mainly focusing on the Weyl semimetals, details of the Weyl semimetals will be discussed in the following.

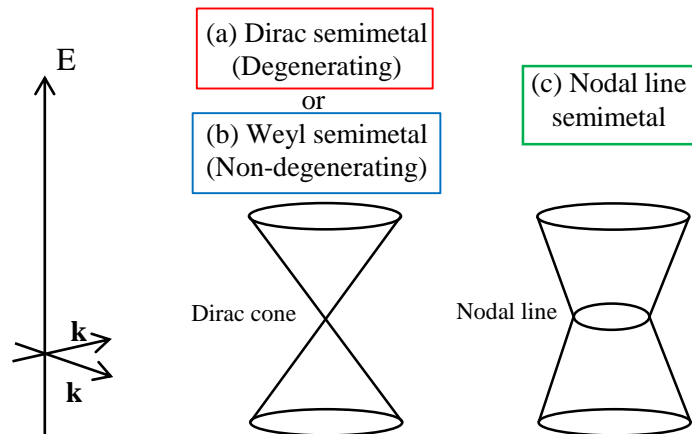


FIGURE 3.2: Typical three type of the semimetals. (a)Dirac semimetals and (b)Weyl semimetals and (c)Nodal semimetals with peculiar band crossings.

3.3 Weyl semimetal

Weyl semimetal is considered to have interesting topological features quite notably. The Dirac cones in the Weyl semimetals in the simplest case (Fig. 3.2(b))

can be reproduced by Weyl equation:

$$H_{\text{Weyl}}^{\pm} = \pm v \mathbf{k} \cdot \boldsymbol{\sigma} \quad (3.1)$$

$$= \pm v \begin{pmatrix} k_z & k_x - ik_y \\ k_x + ik_y & -k_z \end{pmatrix}. \quad (3.2)$$

Where $\boldsymbol{\sigma}$ is the vector of the Pauli matrices. Index \pm is corresponding to plus and minus helicity of the Weyl particles. By introducing unit momentum $\hat{\mathbf{p}} = \mathbf{p}/|\mathbf{p}|$ and helicity operators $\hat{\mathbf{p}} \cdot \boldsymbol{\sigma}$, the eigenstate corresponding to $\hat{\mathbf{p}} \cdot \boldsymbol{\sigma} = +1$ is called right-handed Fermion, while $\hat{\mathbf{p}} \cdot \boldsymbol{\sigma} = -1$ is called left-handed Fermion. From the fermion doubling theorem, Weyl points (the crossing point at the Fermi level) form pairs [7]. This Weyl equation reduces the 4×4 matrices of the Dirac equation to 2×2 matrices. An interesting topological feature appears when one think of Berry curvature which is given by:

$$B(\mathbf{k}) = \nabla_{\mathbf{k}} \times A(\mathbf{k}) \quad (3.3)$$

with the Berry connection defined as:

$$A(\mathbf{k}) = -i \langle u_{n\mathbf{k}} | \nabla_{\mathbf{k}} | u_{n\mathbf{k}} \rangle, \quad (3.4)$$

where $|u_{n\mathbf{k}}\rangle$ is a Bloch state with a band n and a crystal momentum \mathbf{k} [22]. About the valence band of the Weyl Hamiltonian, the Berry curvatures give

$$B_{\pm}(\mathbf{k}) = \mp \text{sign}(v) \frac{\mathbf{k}}{2k^3} \quad (3.5)$$

for right (+) and left (-) handed Weyl fermions, respectively. As the consequence, magnetic monopoles in momentum space is realized by monopole density which is defined as

$$\rho_n(\mathbf{k}) = \nabla_{\mathbf{k}} \cdot B_n(\mathbf{k}). \quad (3.6)$$

The monopole densities give

$$\rho_{\pm}(\mathbf{k}) = \mp 2\pi \text{sign}(v) \delta(\mathbf{k}) \quad (3.7)$$

which correspond to the magnetic monopoles at $\mathbf{k} = 0$ with the strength of $\pm 2\pi$. They act as a sink or a source of the Berry curvature in the momentum space. They are also called monopole and anti-monopole. The same number of the monopoles and anti-monopoles should exist in such substances (Nielsen-Ninomiya's theorem [7]). In addition to those, surface states appear as a band connecting pair of the Weyl points and this band is known as surface Fermi arcs (the cuttings of the 3D Weyl semimetals along k_z reduces the problem to quantum Hall insulators as one can see in the following sections) [23].

3.4 Type-I and Type-II Weyl semimetal

This section shows the Weyl semimetal can have another type of the band structure which is classified as type-II Weyl semimetal [24]. In the above discussions, Weyl semimetals are always having simple cone band structure which is classified as type-I Weyl semimetal. Let's think of the most general Hamiltonian about the Weyl point Eq. (3.1):

$$H'_{\text{Weyl}} = \sum_{i=x,y,z} \sum_{j=0,x,y,z} k_i A_{ij} \sigma_j, \quad (3.8)$$

where \mathbf{k} is the crystal momentum, A_{ij} is the 3×4 matrix of the coefficients, σ_0 is the unit matrix and $\sigma_{x,y,z}$ are the Pauli matrices. With a condition

$$A = \begin{pmatrix} 0 & \pm v & 0 & 0 \\ 0 & 0 & \pm v & 0 \\ 0 & 0 & 0 & \pm v \end{pmatrix}, \quad (3.9)$$

the equation coincides with Eq. (3.1). From this general Hamiltonian for the Weyl points, one can have energy dispersions as

$$\epsilon_{\pm}(\mathbf{k}) = \sum_{i=x,y,z} k_i A_{i0} \pm \sqrt{\sum_{j=x,y,x} \left(\sum_{i=x,y,z} k_i A_{ij} \right)^2} \quad (3.10)$$

$$= T(\mathbf{k}) \pm U(\mathbf{k}). \quad (3.11)$$

$T(\mathbf{k})$ and $U(\mathbf{k})$ are known as kinetic and potential term, respectively. The second term is responsible for the cone-like band dispersion, while the first term is a linear dispersion. Competitions between these two terms give tilts of the Dirac cones which can be realized easily below. For the sake of simplicity, if one assumes

$$A = \begin{pmatrix} 0 & \pm v & 0 & 0 \\ 0 & 0 & \pm v & 0 \\ v_{\epsilon} & 0 & 0 & \pm v \end{pmatrix} \quad (3.12)$$

and $k_x = k_y = 0$, then the effective Hamiltonian becomes

$$H'_{\text{Weyl}} = \begin{pmatrix} (\pm v + v_{\epsilon})k_z & 0 \\ 0 & (\mp v + v_{\epsilon})k_z \end{pmatrix}. \quad (3.13)$$

With this Hamiltonian, as the energy spectrum, one has analytical solutions

$$\epsilon_{\pm}(\mathbf{k}) = (\pm v + v_{\epsilon})k_z. \quad (3.14)$$

Schematic pictures of such energy spectrums are depicted in Fig. 3.3. As one can see, with a condition $v_{\epsilon} = 0$, equivalently $T(\mathbf{k}) = 0$, the Dirac cones form usual isotropic Dirac cones (Fig. 3.3(a)). On the other hand, finite values of v_{ϵ} result in tilts of the Dirac cones (Fig. 3.3(b)). In addition to that, if there

is a direction where v_ϵ , alternatively $T(\mathbf{k})$ becomes dominant over v so as $U(\mathbf{k})$, say $v_\epsilon > v$, the sign of the spectrum will be changed which results in an electron pocket and a hole pocket around the Fermi level (Fig. 3.3(c)). Such type of the Weyl semimetals are called type-II Weyl semimetals while Weyl semimetals with standard isotropic Dirac cones are called type-I Weyl semimetals.

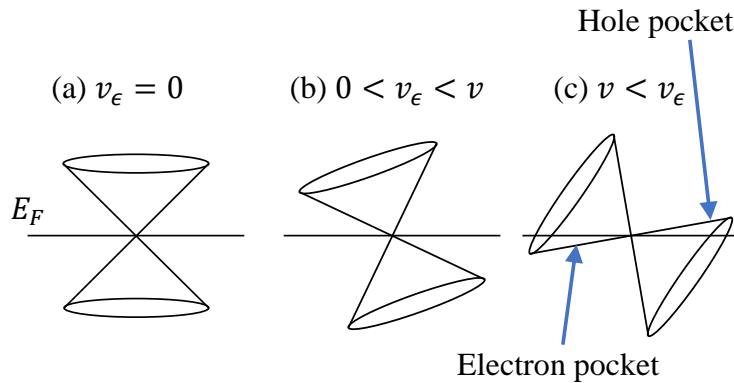


FIGURE 3.3: Variation of a cone-like band dispersion of Weyl semimetal. (a) Without additional v_ϵ , (b) With additional $0 < v_\epsilon < v$, (c) With additional $v < v_\epsilon$, called type-II Weyl semimetal

Another interesting aspect of the Weyl semimetals are unusual magnetoresistances namely, changes of the electrical resistances caused by external magnetic fields. In such type-I Weyl semimetals, the magnetoresistances show negative values. It is quite peculiar feature. On the other hand, the type-II Weyl semimetals are found not showing such negative magnetoresistance and show giant positive magnetoresistance instead (such behavior has been found in the first possible type-II Weyl semimetal WTe_2 [25]). The reason of the tilts in real type-II Weyl semimetals have not been revealed yet, however, these tilts are understood as silent responses to the external magnetic fields because of the behavior.

3.5 TaAs as the first type-I Weyl semimetal

The first candidate material of possible realization of the type-I Weyl semimetal is TaAs. TaAs has nonsymmorphic $I4_1md$ crystal group which breaks parity inversion symmetry that gives an anticipation to be the Weyl semimetal (Fig. 3.4). Indeed, a critical signature of the Weyl semimetals, the Surface Fermi Arcs are predicted from the first-principle electronic structure calculations and also in other sister materials (TaP, NbP, NbAs) [26].

After the prediction, the first observation of type-I Weyl semimetal state has been achieved in TaAs by B. Q. Lv et. al. [28]. Their ARPES experiments reveal the Surface Fermi Arcs are existing in TaAs (Fig. 3.5 (b)) and thus it has been recognized as the first realization of the type-I Weyl semimetal.

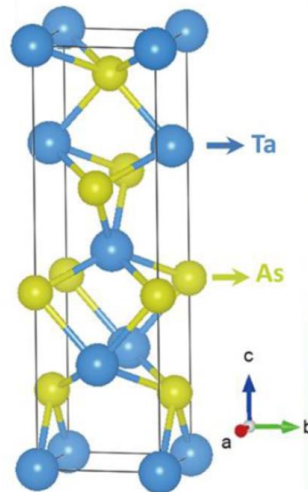


FIGURE 3.4: Ball and stick crystal model of TaAs. Blue spheres are Ta atoms and yellow spheres are As atoms, respectively. The picture is adopted from [27]

3.6 WTe_2 and $MoTe_2$ as the first type-II Weyl semimetal

Layered transitional dichalcogenides WTe_2 and $MoTe_2$ which have parity inversion broken $Pmn2_1$ crystal structure (Fig. 3.6) have been predicted to be the first type-II Weyl semimetal candidates [24]. From the first-principle electronic structure calculations, these substances are predicted to have tilted Dirac cones [24, 29, 30].

After these predictions, ARPES experiments revealed WTe_2 and $MoTe_2$ are possible candidates of the type-II Weyl semimetal [33–35]. The observed electron and hole pocket in WTe_2 and $MoTe_2$ are shown in Fig. 3.7.

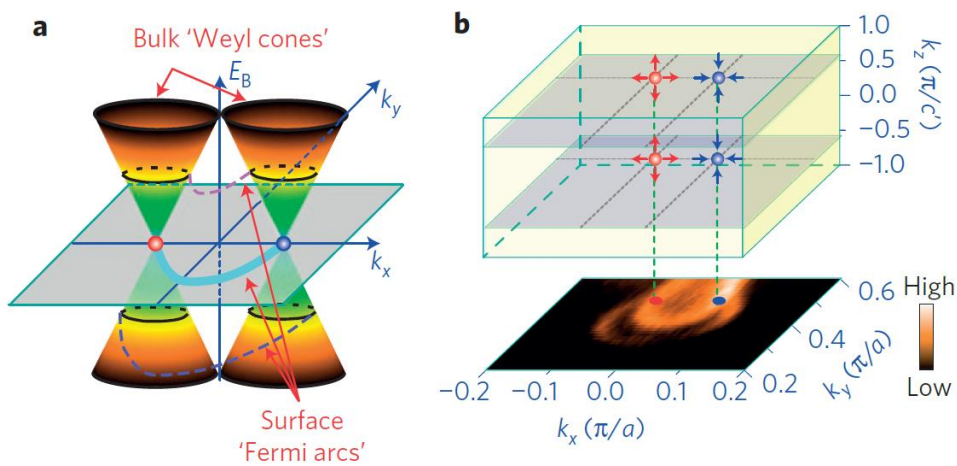


FIGURE 3.5: A schematic picture of a pair of bulk Weyl nodes (a) and observed surface Fermi Arc which is connecting those nodes by means of ARPES (b). The picture is adopted from [28]

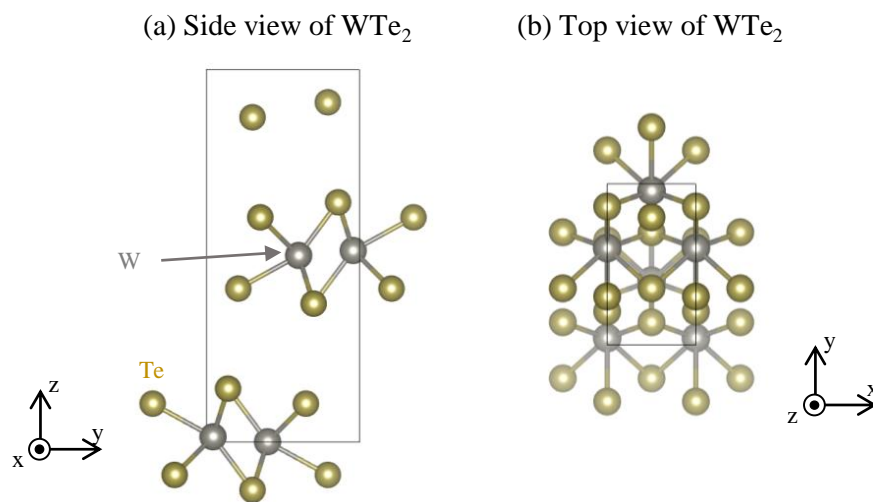


FIGURE 3.6: Experimental crystal structure of the orthorhombic WTe_2 [31, 32]. Gold spheres indicate Te atoms while silver spheres indicate W atoms. Side view (a) and Top view (b). Substitution of Mo atoms at the place of W atoms coincides the crystal structure of $MoTe_2$ with slightly different lattice parameters.

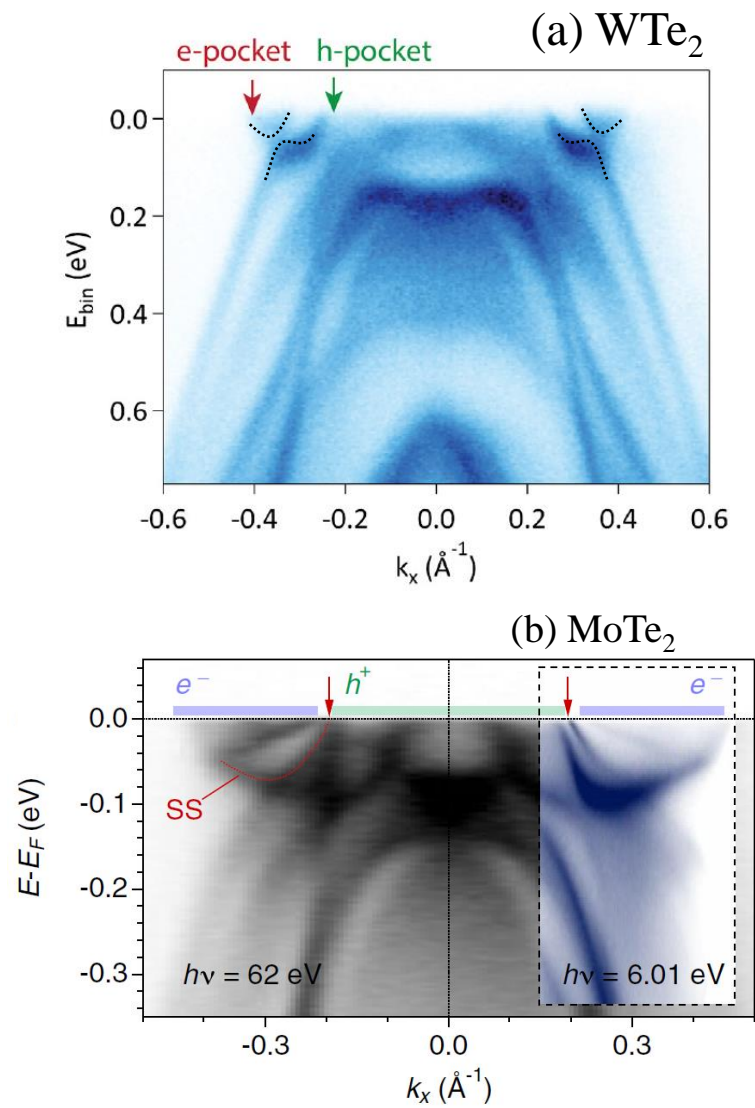


FIGURE 3.7: Observed electron and hole pocket in (a) WTe_2 and (b) MoTe_2 by means of ARPES. The pictures are taken from [34]

Chapter 4

Interpretations of the photocurrent intensities

As it is described, information contained in the photocurrent intensity should be understood with a robust calculation. So far, this thesis has accessed numerical difficulties of ARPES and interesting materials, which are mainly explored by ARPES.

This chapter discusses the interpretation of the ARPES photocurrent intensity, which has been overlooked, and there is no robust interpretation of it so far. This chapter tries to find the answer of such question by using several method (plane-wave approximation, matching method and one-step model).

Before go into the detailed discussion of the photocurrent intensity, at this point, advantages and disadvantages of the existing methods will be summarized. Here the mainly used two methods (plane-wave approximation (PWA) and multiple scattering theory (MST), equivalently, one-step model) are summarized in Table. 4.1.

TABLE 4.1: Comparison of widely used methods

Method	Advantages	Disadvantages
PWA	Simple	Strong approximation
MST	Exact boundary condition	Potential shape

As one can see from the Table 4.1, those widely used methods have sort of "trade-off" relations. One of the possible solution to these "trade-off" relations is the matching method which has been described in Sec. 2.7, however, still technical problems are remaining (for instance, there is no clear road map to implement it to powerful plane-wave basis DFT code). Therefore, in Sec. ??, the matching method will be applied to a simple potential well in which scattering problem can be solved exactly, analytically. Some benchmark between plane-wave approximation, matching method and the exact solution will be discussed.

One of the method which can treat the boundary condition exactly is the one-step model. In reality, the one-step model can be achieved by solving a multiple-scattering problem. In Sec. 4.2, the multiple scattering problem will be solved for the Weyl semimetal candidate MoTe₂. After that, meaning of the photocurrent intensity will be discussed.

4.1 A graphene-like box-potential

The matching method should be a new powerful method for theoretical ARPES calculation. This method is a "newborn" method. Therefore, it has not been implemented in a robust DFT code. This section applies the matching method to a one-dimensional periodic single rectangle potential well. This toy-model can be a good test-bed if one chooses proper parameters of the potential and lattice. This model can be considered as a simplified slab model of two dimensional lattice where the axis of the one-dimensional model corresponds to the axis perpendicular to the plane of the two-dimensional material (see Fig. 4.1).

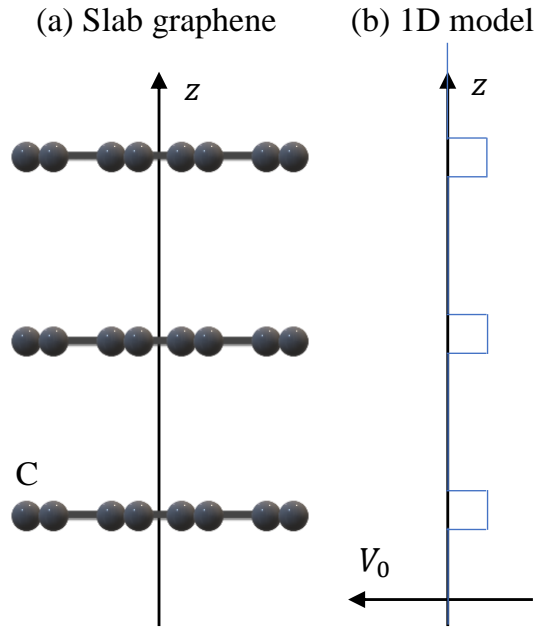


FIGURE 4.1: Schematic picture of (a) a slab model graphene and (b) the one-dimensional periodic potential well model.

As a real model, two-dimensional material graphene has been chosen as a test material. Therefore, here this toy-model is fitted to graphene electronic structure (corresponding graphene slab model is shown in Fig. 4.1 (a)).

Here consider the plane-wave basis to be used in the calculation of eigenvalue problem of the one-dimensional periodic potential. Then, the eigenstates are given in the plane-wave basis as

$$\psi_{nk}(z) = \sum_G C_{nk}^G e^{i(k+G)z}. \quad (4.1)$$

Then, by inserting this basis to Eq. 2.45 one can obtain matrix, however, another problem is how to determine the dimension or the number of the simultaneous equation. This can be a problem, but in this case, only two states (whose eigenvalues are closest to the final state energy) are chosen. Now, we

have two equations used in a simultaneous equation. Therefore, we have a 2×2 matrix to be diagonalized. After the diagonalization, one has two coefficient α_1 and α_2 so as to the numerical final state wave function obtained by matching

$$\psi_f = \alpha_1 \psi_{nk_1} + \alpha_2 \psi_{nk_2}. \quad (4.2)$$

Electronic structure of a supercell graphene is calculated by Vienna-Ab initio-Simulation-Package (VASP) [18, 36]. Where the potential is treated by projector-augmented wave (PAW) method [37] and plane-wave basis set. Supercell size $c \approx 20 \text{ \AA}$ has been chosen. Local Density Approximation (LDA) [38] is used in the exchange-correlation functional. The plane-wave cut-off is set as 1200 eV and the 34 k -points mesh are used.

Obtained Density Of States (DOS) of the graphene is plotted in Fig. 4.2 along with free electron DOS $\propto \sqrt{E}$ up to 70 eV. The obtained DOS shows almost complete matching with the free electron DOS, meaning the supercell size is enough where the continuum state is sufficient.

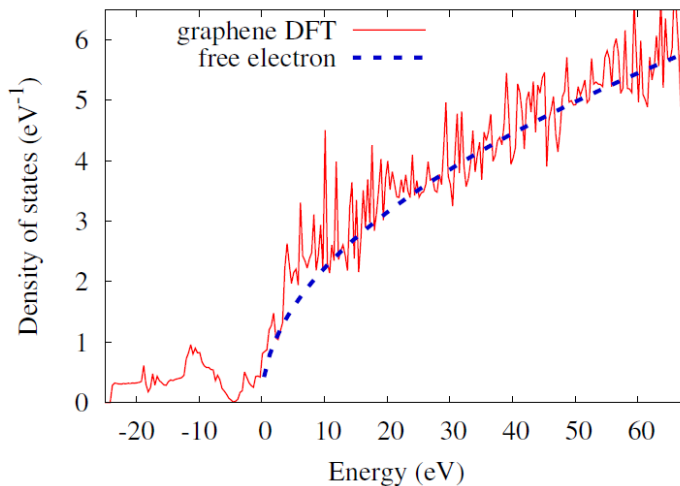


FIGURE 4.2: Calculated DOS of graphene (red) and free electron (blue).

Fig. 4.3 shows band structure along out-of-plane k_z of the supercell graphene (a), one-dimensional periodic potential (b) and free electron (c). Parameters of the one-dimensional periodic potential are fitted based on this comparison (its band structure to have roughly same band structure). Thus, the model is realistic and may have some information of graphene. One may notice hardly k_z dispersive bands in the graphene DFT bands which were denoted as thin lines. These do not have finite group velocity along z meaning bounded in two-dimensional plane. Therefore, those can be ignored for the purpose of this study. As one can see from the band structure, those (except free electron) have a bound state $E_i = 7.2 \text{ eV}$ which is used as an initial state.

Fig. 4.4 shows the imaginary part and the real part of the final state wave function which is calculated by the matching method (red solid line) and exact solution of the non-periodic one-dimensional potential well (dashed blue

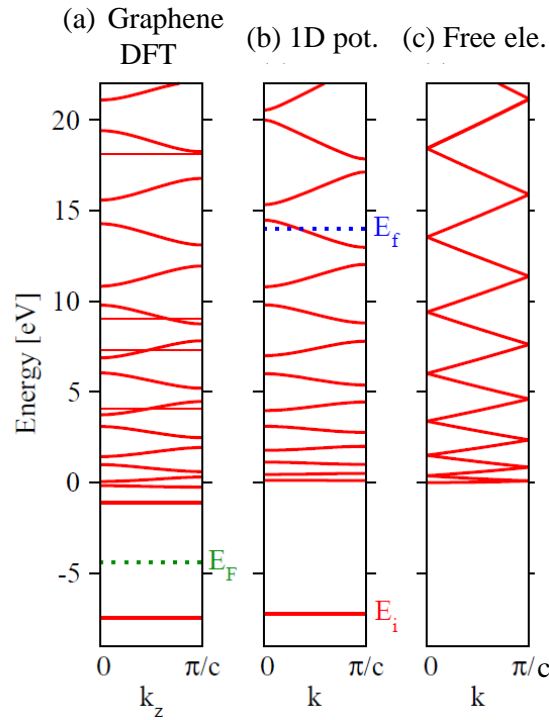


FIGURE 4.3: Calculated band structure of (a) Graphene, (b) Periodic one-dimensional potential well, (c) Free electron.

line). This final state has been chosen by a photon energy of the Helium I lamp $\hbar\omega(\text{HeI}) = 21.2$ eV so that the final state energy $E_f = E_i + 21.2 = 14.0$ eV. These shows almost perfect matching. Besides those, a plane-wave is plotted as black solid lines. As one can see from the picture, the matching method wave function and exact wave function coincide with the plane-wave at the boundary. Thus, these satisfy the boundary condition. By using this final state wave function and initial state wave function of the selected initial state, one can evaluate the photocurrent intensity via the transition matrix element Eq. 2.5. If one uses a plane-wave final state, it is exactly the final state plane-wave approximation which has been introduced in Sec. 2.6.

Fig. 4.5 indicates the photocurrent intensity calculated by the selected initial state (E_i of Fig. 4.3 and (a) of Fig. 4.4) and the final state wave function obtained by matching (red) and a plane-wave approximation (blue). The polarization vector has been chosen as $\mathbf{A} = \mathbf{e}_z$ (unit vector along z). Intensity of both of the matching and the plane-wave final state show similar shape photon energy dependence. However, there is a large shift. Indicating the final state plane-wave approximation is not so reliable, especially in low energy region. A better matching probably can be obtained if one shift the intensity of the plane-wave approximation around -60 eV. On the other hand, the final state wave function obtained by the matching method is probably quite reliable except some noise at the low energy region. The noises are probably caused by the choice of the number of states. In this calculation, only two

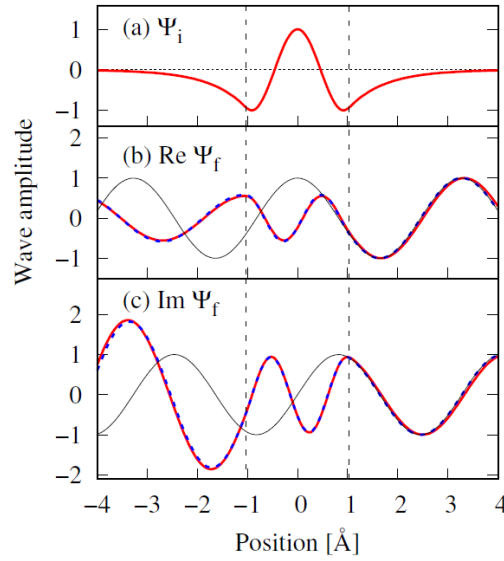


FIGURE 4.4: (a) Calculated bounded initial state wave function, (b) Real part of the final state wave function and (c) Imaginary part of the final state wave function. Red lines indicate the result of the matching method, blue dotted lines indicate an exact final state wave function of non-periodic potential well and black solid line indicate plane-wave which is matched at the boundary, respectively.

states are chosen which should be more reliable if one chooses more states. Therefore, this problem remains as a numerical problem should be solved in the future.

4.2 MoTe_2

As it is described in Chap. 3, topological Weyl semimetal is receiving much attentions recently. The particular interest is coming from the existence of the mass-less Dirac fermion which is called Weyl fermion which has not been observed in nature. This expectation is coming from the fact that the band dispersion of such material is represented by the Weyl equation (Eq. 3.1). Recent finding of the possibility of the tilted cone-like band dispersion has opened incipient field of interest. The materials have such tilted cones are called type-II Weyl semimetal and those are extensively searched recently.

The transitional metal dichalcogenides (TMDC) MoTe_2 is predicted to belong such type-II Weyl semimetal, however, a clear experimental evidence is still lacking. Therefore, it is known as a candidate material of the type-II Weyl semimetal. Indeed, critical evidence is a quite difficult problem. Special feature of such Weyl semimetal is that the cone-like tilted band dispersion always forming a pair and those are connected by a unclosed Fermi line which is known as surface Fermi arc [21]. Therefore, direct observation of the surface Fermi arc is an essential evidence of the Weyl semimetal. Therefore,

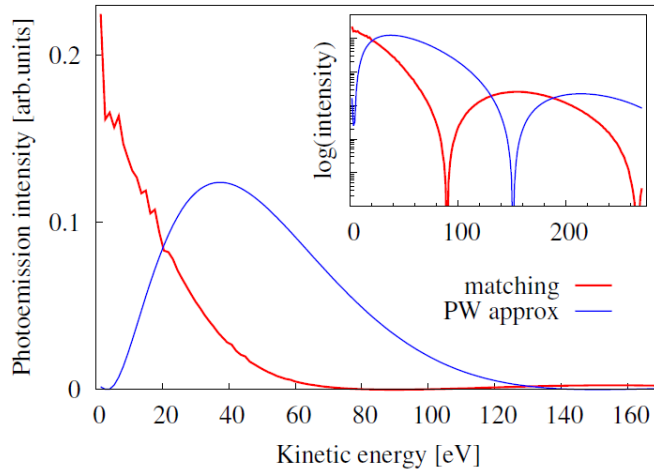


FIGURE 4.5: Calculated photon energy dependence of the ARPES intensity using the final state obtained from the matching method (red) and the final state plane-wave approximation (Blue). Inset indicates logarithmic scale of those.

many researchers are trying to find the surface band structure by means of ARPES which can give direct observation of such band dispersion. While the DFT electronic structure calculations give reliable results for such materials, ARPES results itself should be understood by theoretical calculations with exact boundary condition. This section provides first such ARPES calculation which will be a key of searching special surface Fermi arc of MoTe₂.

MoTe₂ has monoclinic centrosymmetric 1T' structure at the room temperature. Cooling down to below 240 K makes the MoTe₂ to orthorhombic T_d structure (space group *Pmn*2₁ structure). Since the orthorhombic T_d structure is breaking parity inversion symmetry, which gives a possibility of the Weyl semimetal. Most of the research are focusing on the region where the surface Fermi arc is expected to be found.

ARPES calculation with exact boundary condition is needed not only to understand the experimental results, but also to suggest proper condition of ARPES (e.g. light polarization and photon energy). For instance, if one could predict observable bands with specific condition, future experiments would be able to use the suggested conditions effectively.

This section tries to understand the meaning of the ARPES intensity and suggest best ARPES condition for future experiments by means of ground state DFT calculation and one of the most efficient "one-step" ARPES calculation.

4.2.1 Calculation details

As it is described above, this section introduce results of two types of calculations. In any case, an experimental crystal structure with the lattice parameters $a = 3.477 \text{ \AA}$, $b = 6.335 \text{ \AA}$ and $c = 13.883 \text{ \AA}$ [39] is used. The bulk crystal

structure is shown in Fig. 4.6 (a) and (b).

In DFT ground state calculations, a Slab structure has been constructed with four layers of MoTe_2 and 10 \AA of vacuum. Out of plane lattice parameter c results in $c = 37.8 \text{ \AA}$. The PAW method is used as it is implemented in VASP. Commonly adopted Perdew-Burke-Ernzerhof (PBE) exchange-correlation functional is used. $16 \times 16 \times 1$ k -points mesh is used in self-consistent field (SCF) calculation and the plane-wave cut-off is set as 400 eV. The relativistic spin-orbit coupling (SOC) is taken into account in all calculations.

The one-step ARPES calculation has been performed by using spin-polarized relativistic Korringa Kohn Rostoker (SPR-KKR) package [40]. As the Slab model DFT calculation, same experimental crystal structure is used in all calculations and SOC is treated via Dirac equation. As the potential shape, Atomic Sphere Approximation (ASA) is used. Angular momentum expansion $l_{\text{max}} = 3$ is used. Firstly, the bulk Green function is computed, then, a surface model is constructed. Next, the Green function of the semi-infinite surface model is calculated from the solution of Dyson equation. In the one-step model calculations, Layered KKR (LKKR) method is used. In the LKKR formalism, one treats spherical waves in the layer while plane-waves are used between the layers.

One of the problem of the one-step model is the potential shape. Since MoTe_2 has an opened crystal structure, the spaces must be filled with empty spheres. For the bulk SPR-KKR calculation, space filling is required and empty spheres were put both inside the MoTe_2 layers and between them. In the LKKR calculations (for ARPES) however, serious problem occurred and could not reproduce the slab band structure. A natural choice of the empty spheres was not applicable. Therefore, the empty spheres inside the layers have been removed while those of between the layered are left. Then, the quality of the electronic structure was much improved. Actually, same procedure has successfully been applied to another similar material WTe_2 [41, 42].

4.2.2 Band structure of MoTe_2 (T_d)

Since the topologically protected tilted cone-like band structure has been observed in many experiments and *ab-initio* calculations along $\bar{\Gamma}(0, 0) - \bar{X}(0, 0.5)$ point in the two-dimensional Brillouin Zone, this region will be discussed in the followings. Fig. 4.7 shows ground state band structure calculated by VASP (a) and the ARPES intensity map calculated by one-step calculation (b). Both showing very similar band structure. Since the plane-wave basis DFT is considered quite reliable theory for this kind of not strongly correlated materials, the result indicating this one-step calculation is accurate enough. Also, characteristic bands which are called hole and electron pocket are found in both calculations. Those are considered to form a tilted cone-like band dispersion. Both results are showing very good agreements with other calculations and experiments [29, 34].

One may notice that the form of the bands in one-step and ground state DFT are not in complete agreement. This is exactly the disadvantage of the

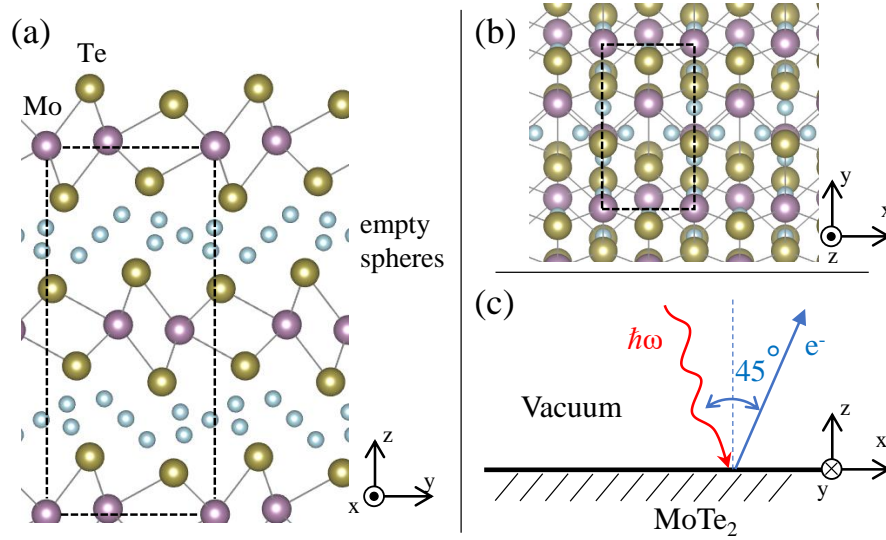


FIGURE 4.6: Crystal structure of MoTe_2 and experimental geometry which will be discussed in Sec. 4.2.4. Gold, purple and blue small spheres are indicating Te atoms, Mo atoms and empty spheres, respectively. Empty spheres will be used only in ARPES calculations. (a) Side view (b) Top view (c) Experimental geometry

MST which has been explained at the beginning of this Chapter. Of course, it is not perfect, but qualitatively agreeing. At least, the characteristic hole pocket and electron pocket are almost same form. Therefore, we can trust these band dispersions for the purpose of this work.

4.2.3 Orbital projection and polarization dependence

Now, let me discuss the results obtained from these two calculations. One-step calculation should yield exact final state wave functions. Therefore, if calculated intensities show useful information, this would be a useful guide to future experiments. However, understanding calculated ARPES intensities is a still quite difficult task. Here, this chapter employs the $l \pm 1$ selection rule which has already been discussed in Sec. 2.5 to understand the meaning of ARPES photocurrent intensity and tries to provide useful guides to future experiments.

Strategy of this subsection is following. First, consider possible initial state as it is formally allowed by the $l \pm 1$ selection rule. Second, predict which part of the ARPES intensities can be pronounced based on the rule. Finally, provide useful guides based on this analysis.

Since main interest of studies of MoTe_2 is around the Fermi energy E_F , let's focus on this region. Then, those states are clearly dominated by Te $4p$ -orbital and Mo $5d$ -orbital as seen in Fig. 4.8.

Hence, following discussions only consider these states as the initial state. For the sake of simplicity, this chapter considers only $l - 1$ transition. One may think this is a large approximation, however, as it will be shown later in

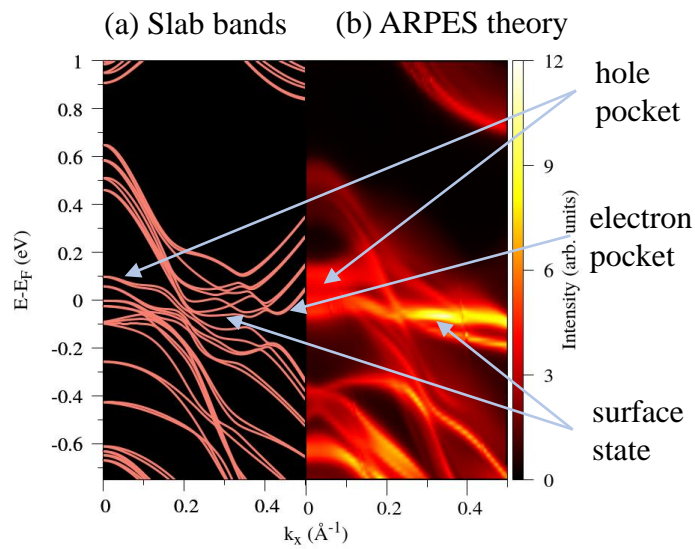


FIGURE 4.7: Calculated band structures along $\bar{\Gamma} - \bar{X}$ in the 2D Brillouin Zone (a) DFT Slab bands. (b) ARPES intensity map calculated from One-step ARPES calculation with photon energy $\hbar\omega = 60$ eV and unpolarized light (x-pol. + y-pol. + z-pol.).

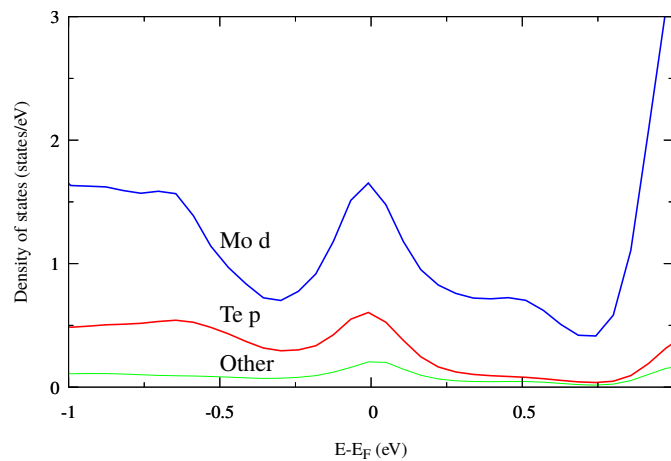


FIGURE 4.8: DOS projected onto Te $4p$ -orbital (red), Mo $5d$ -orbital (blue) and rest (green).

this chapter, this is quite efficient approximation. The reason can be understood as follows. As an example, consider p_z initial state. In that case, the intensity has the $l - 1$ transition yields s final state. Then, the intensity has a strong $\cos^2 \theta$ dependence. This can be easily understood by the fact that in general case of the light polarization is in xy -plane, the transition matrix element in dipole approximation is given as

$$M_{p_z \rightarrow s} = \langle s | z | p_z \rangle \cos \theta, \quad (4.3)$$

where the angle θ is the angle between the light polarization and z -axis. Therefore, square of this is proportional to $\cos^2 \theta$. However, $l + 1$ transition has 5 such d -orbital final states for any light polarization. Thus, I believe this is enough efficient analysis.

Now, let's use only linearly polarized light along x , y and z -axis (which this section calls x -polarization, y -polarization and z -polarization, respectively). Then, list possible transitions for these light polarization.

- X-polarization: Te $p_x \rightarrow s$ and Mo $d_{xz} \rightarrow p_z$
- Y-polarization: Te $p_y \rightarrow s$, Mo $d_{yz} \rightarrow p_z$ and Mo $d_{xy} \rightarrow p_x$
- Z-polarization: Te $p_z \rightarrow s$ and Mo $d_{z^2} \rightarrow p_z$

These are the all possible transitions according to the $l - 1$ selection rule.

Another important factor is the photon energy used in the light. Here let us use 60 eV as used in an experiment by Tamai et al. [34]. In the following figures, ARPES intensity with x , y and z -polarization will be plotted along with the orbital DOS projected onto the band dispersions which are possible initial states regarding the light polarization. As for the projected DOS (PDOS), only surface Te atoms and Mo atoms are considered. Since the Mo atoms are not exposed at the surface, damping effects are taken into account by dividing the DOS by a factor of 2 in a simple way.

Fig. 4.9 shows the calculated ARPES with x -polarization (a) and corresponding possible initial states (b) and (c). As one can see from the PDOS of Mo d_{xz} and Te p_x , those initial state analysis predict well intense points of the ARPES intensity for x -polarization. One of the interesting character is that with the x -polarization, characteristic hole pocket is highlighted very well. Furthermore, it is almost solely described by the Te p_x initial state which dominates the hole pocket band. As for the Mo d_{xz} state, still the PDOS is showing same character with the calculated x -pol. ARPES. The hole pocket is interesting feature of type-II Weyl semimetal, thus, if one wishes to observe the hole pocket of MoTe₂, one should use linear x -pol. in the ARPES experiment. This situation can be achieved with s -polarization light along y -axis.

Fig. 4.10 shows the calculated ARPES with y -polarization (a) and corresponding possible initial states (b), (c) and (d). As seen from the calculated ARPES, linearly dispersed bands are pronounced by y -polarized light. This band, actually, consists of two bands. The lower part is coming from the hole pocket while the upper part is coming from the electron pocket. Those two

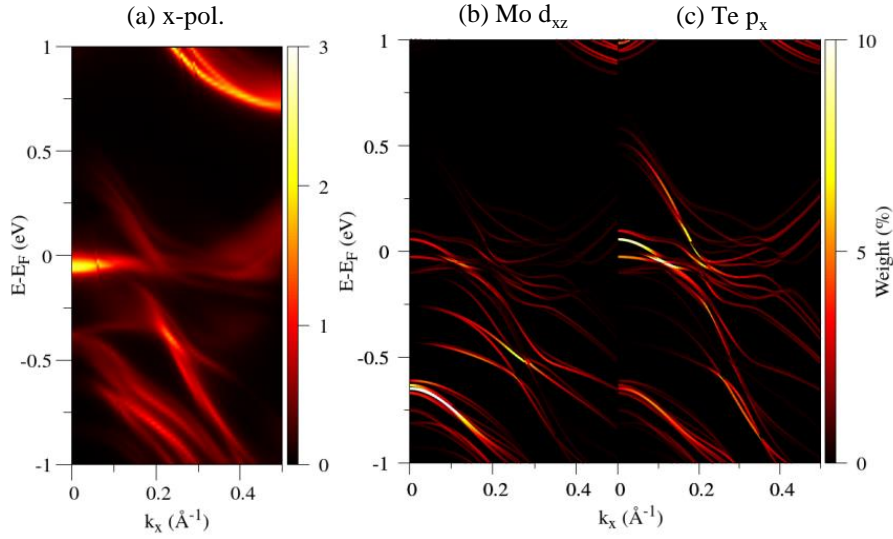


FIGURE 4.9: (a) Calculated ARPES intensity with the linear x-polarization and photon energy $\hbar\omega = 60$ eV. and corresponding possible initial states DOS projected onto the bands (b-c).

parts can be described by Mo d_{yz} and Mo d_{xy} orbital. The calculated ARPES intensity also has pronounced bands below this linearly dispersed bands. This group of bands are mainly coming from Te p_y orbital. As well as the x-polarization, y-polarization can be realized by the s-polarization, but with the light incident in the xz -plane.

Fig. 4.11 shows the calculated ARPES with z-polarization (a) and corresponding possible initial states (b) and (c). Again, the calculated ARPES intensity for z-polarization is well explained by the $l - 1$ transition. One of the important character of z-polarization is that the special electron pocket is pronounced well. Possible initial states also have some weight. At the same time, this electron pocket is possibly the surface states as seen in other work [33]. Which is also made of these possible initial states. Another character is an arc-like band dispersion around $k = 0$. As seen from the Fig. 4.11 (b), this is the character of Mo dz^2 orbital. As for the realization in experiments, exact z-polarization is impossible. However, slightly tilted z-polarization is possible by using p-polarization from almost grazing angle along any direction in xy -plane. With z-polarization, the intensity is much higher than that of in-plane polarization, therefore, slightly tilted grazing angle should give almost z-polarization.

Both of x and y polarization entirely show less intensity compare to z-polarization because the emission angle is almost perpendicular to the light polarization especially at the $\bar{\Gamma}$ point. This is well known that the intensity of the parallel emission is higher than perpendicular emission [43].

This subsection concludes if one wishes to observe the hole pocket, suitable condition for observing it is s-polarized light along y-axis. In contrast, if one wishes to observe the electron pocket, the suitable light polarization

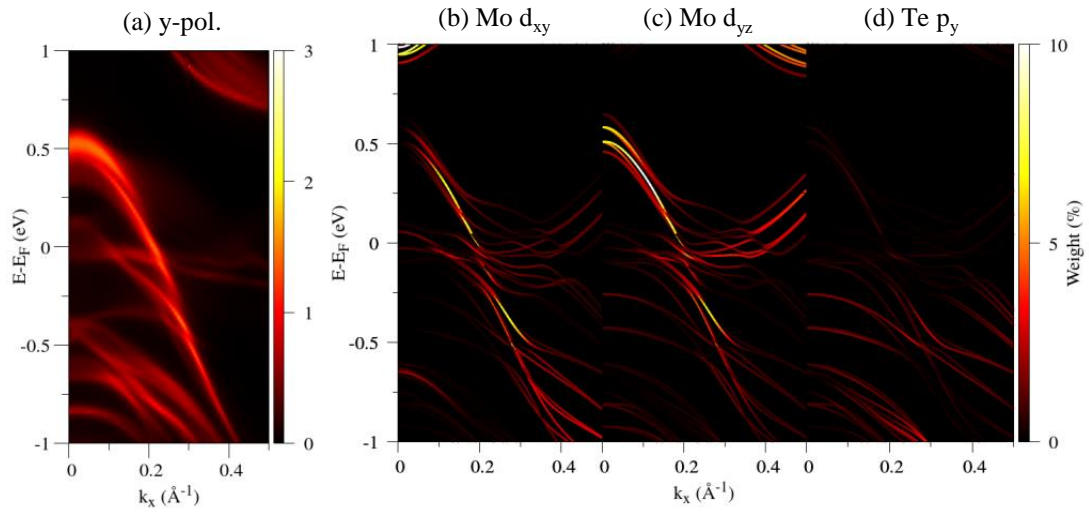


FIGURE 4.10: (a) Calculated ARPES intensity with the linear y-polarization and photon energy $\hbar\omega = 60$ eV. and corresponding possible initial states DOS projected onto the bands (b-d).

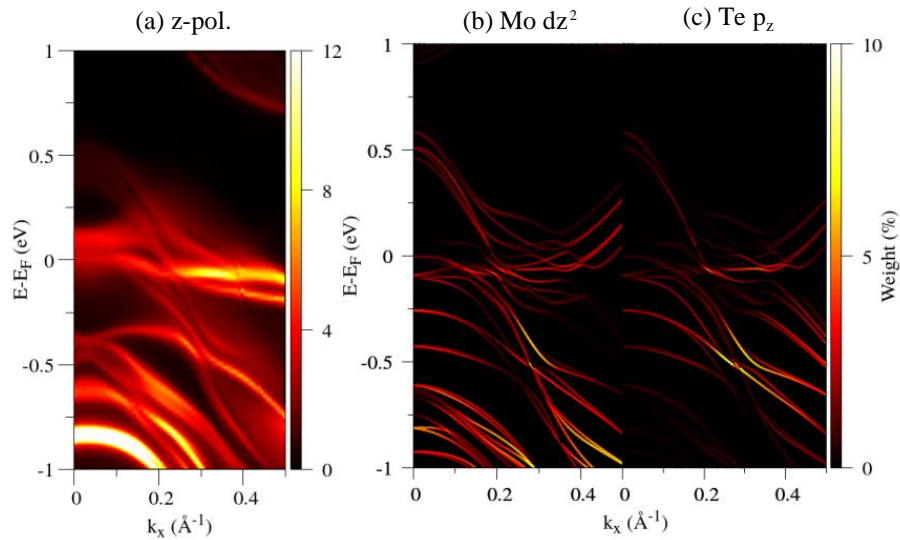


FIGURE 4.11: (a) Calculated ARPES intensity with the linear z-polarization and photon energy $\hbar\omega = 60$ eV. and corresponding possible initial states DOS projected onto the bands (b-c).

is perpendicular to the plane i. e. z-like p-polarized light. Of course, there should be photon energy dependence, however, the photon energy dependence does not play important roll as it will be justified in the next subsection.

4.2.4 Comparison with an experiment

Tamai et al. [34] measured ARPES with p-polarization. In their experiment, the electron pocket is very well seen. Since the p-polarization is made of the matrix element of z-polarization and in-plane polarization, this can be understood as almost z-polarization (Intensity of z-polarization is around four times higher than that of in-plane polarization). The z-polarization has strong intensity at the electron pocket and which is in very good agreement with the experiment by Tamai et al. [34] (see Fig. 3.7 (b)).

Here this subsection compares our analysis with an ARPES experiment of MoTe₂ done by Nakata et. al. of Chiba University. Fig. 4.12 (a) shows the experimental ARPES result which has been performed with 6.27 eV of the photon energy and s-polarized light (the experimental geometry is shown in Fig. 4.6 (c)). The collected electrons correspond to the $\bar{\Gamma} - \bar{X}$ line. The light incident in the xz-plane, thus, this is same situation with y-polarization which is considered in above discussion except the photon energy. The calculated ARPES with the same condition is shown in Fig. 4.12 (b) along with the possible initial states for y-polarization (d)-(f). Actually, there are six features seen from the experimental ARPES marked as 1-6 in the picture. No. 1 is coming from the hole pocket while the No. 5-6 are coming from the electron pocket. As one can see from Fig. 4.12 (b), calculated ARPES are showing they agree well with the experimental result except band No. 2 which has a shift around 0.1 \AA^{-1} along k_x . In this case too, the ARPES intensity is explained by corresponding $l - 1$ transition. Another important feature is a tilted cone-like band structure at around 0.2 \AA^{-1} (Fig. 4.12 (c)). This is also seen in the experiment. The tilted cone-like band dispersion is the main feature of the type-II Weyl semimetal which has been predicted and observed in many studies [24, 29, 33, 34]. In addition to those, when one compares Fig. 4.12 (b) and Fig. 4.10 (a), those have very similar intensity map except magnitude of the intensity. The average intensity is over one order of the magnitude larger than that of 60 eV. Therefore, the map itself is not changed so much and thus, there is no large photon energy dependence compared to polarization dependence.

4.3 Conclusion and future prospect

Firstly, this chapter have introduced some theoretical method and mechanism of ARPES. The main problem in calculations of ARPES is that there is no method which satisfies two condition exact and efficient. Of course, one may use strong approximations such as PWA. However, as seen from Sec. 4.1, even in the simplest one-dimensional potentials, the accuracy of the PWA is

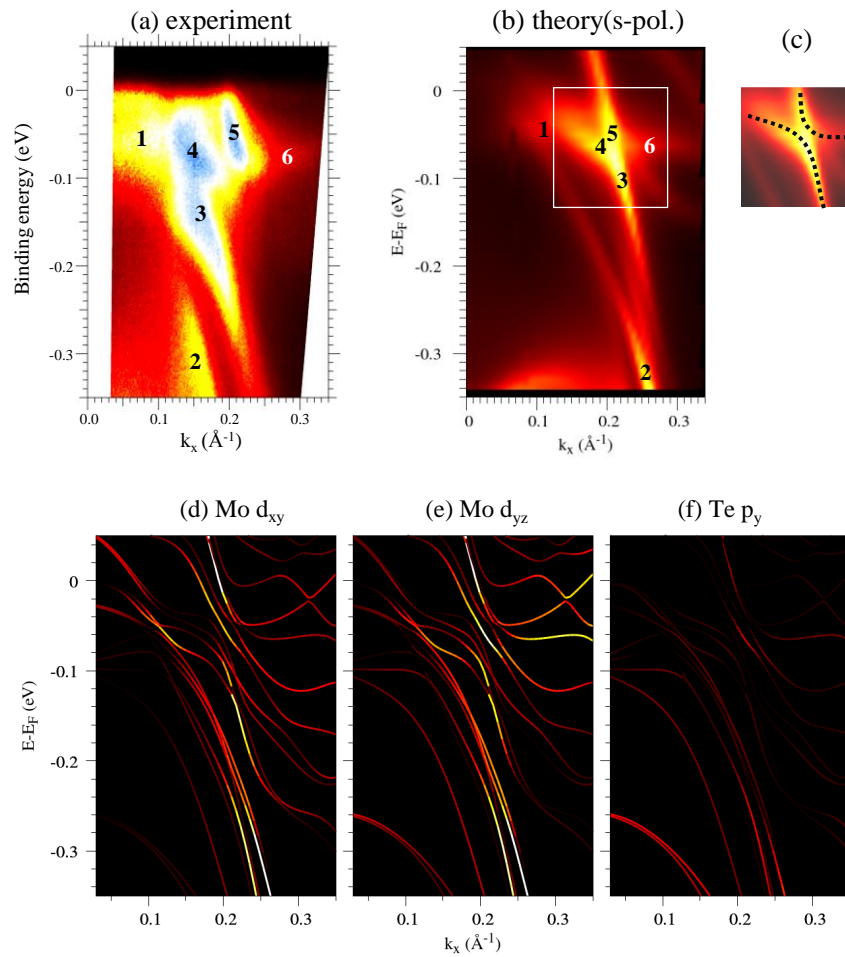


FIGURE 4.12: (a) Experimental ARPES result with photon energy $\hbar\omega = 6.27$ eV and s-polarized light. (b) Calculated ARPES intensity map using same condition with the experiment (a). (c) A clip of the tilted cone-like band dispersion in (b). (d-f) Corresponding possible initial states for y-polarization.

questionable. On the other hand, one-step calculation gives exact final state wave function, this is the biggest advantage of MST, however, the potential shape which is imposed on the MST is the problem. Therefore, second, this chapter have suggested a method which can resolve such situation. The method has successfully been applied to a graphene like one-dimensional box potential. The result showed exact boundary condition should be taken into account for reliable ARPES calculations. Furthermore, the matching method showed a very good agreement with the exact solution of the scattering problem. There are numerical problems to be solved to implement this method to powerful DFT code which has been encountered even in such simple toy model case. However, if the numerical problem is completely solved, the matching method would be a striking method. In the last part, one of the efficient methods, one-step model has successfully been applied to a candidate material of type-II Weyl semimetal, MoTe_2 . The exact final state wave function is quite important in such two-dimensional topological materials because main interest of such materials is very small energy range around the Fermi level. In this work, it is shown that the disadvantage of the one-step model can be resolved by adjusting potential. In particular case of the opened layered structures, one should remove empty spheres inside layers. After that, the meaning of the ARPES intensity has been discussed by means of the orbital projected bands and dipole $l - 1$ selection rule. Quite naturally, the initial states based on the selection rule predict what band will be highlighted. Especially, around the Fermi level, the inherent hole and electron pocket can be selected with suitable light polarization which should be a key for the future ARPES experiments. At the end, the calculated results show how these analysis is correct by making comparison with a recent ARPES experiment. In summary, those analysis shows specific atomic orbital can be highlighted with corresponding light polarization based on $l - 1$ transition.

There is still room for discussions of the information included in ARPES intensities. To reveal the information completely, the exact final state wave function should be taken into account in the ARPES calculation which is still a challenging problem. If the information contained in ARPES intensity is completely revealed, ARPES would be much more fruitful experiment.

Part II

Theory of magnetoelectric effect in $\text{Ba}_2\text{CuGe}_2\text{O}_7$

Chapter 5

Introduction

Controlling materials with the external (electric or magnetic) fields is highly demanding in the context of fundamental physics and applications to new generation electric devices. Maxwell equations suggest, the electric fields and the magnetic fields are strongly coupled, however, the coupling between electronic polarization and magnetization is still non-trivial. In solids, external electric fields induce electronic polarization and external magnetic fields induce magnetization as linear responses. P. Curie has predicted the external electric fields induce not only the electronic polarization, but also the magnetization and vice versa [44] (Fig. 5.1). Later I. E. Dzyaloshinskii has predicted such effect in Cr_2O_3 [45]. Nowadays such effect is known as Magnetoelectric (ME) effect. The origin of the ME effect has been understood from the view point of the symmetry. After the discovery of the linear ME effect, many researchers tried to make the giant (or non-linear) ME effect (Fig. 5.2) which should be a key for applications of such materials. The key character to realize the giant ME effects is so-called multiferroics, namely, spontaneous electric polarization coexists with some spontaneous magnetic order (Fig. 5.3). Recently, such giant ME effect has been found in multiferroic RMnO_3 ($R = \text{rare earth}$) [46–48]. However, microscopic understanding of the giant ME effects is a still non-trivial task. The most widely used mechanisms are fully based on phenomenological theories and lacking theoretical accurate descriptions. Indeed, the existing phenomenological theories fail to describe giant ME effects in some proper screw magnets. Thereby effective and robust theoretical description is highly demanded and finding it is a challenging problem.

Multiferroics part of this thesis is structured as follows. Chapter 6 discusses basic concepts of the multiferroics and the (linear and non-linear) magnetoelectric effects. Chapter 7 describes theoretical methods used for the analysis of the multiferroics. By the way, multiferroics is a property of the strongly correlated materials, therefore, the Chap. 7 describes theoretical methods usually used for strongly correlated materials. Finally, the chapter 8 describes how the controversial non-linear magnetoelectric effects are clearly described in $\text{Ba}_2\text{CuGe}_2\text{O}_7$ as an example. After the analysis, the last chapter conclude what has been revealed already and what can be done in the future.

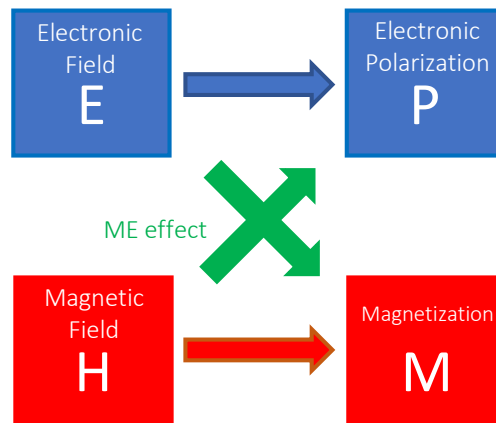


FIGURE 5.1: A schematic of the magnetolectric effect. Green arrows are indicating the magnetolectric effect.

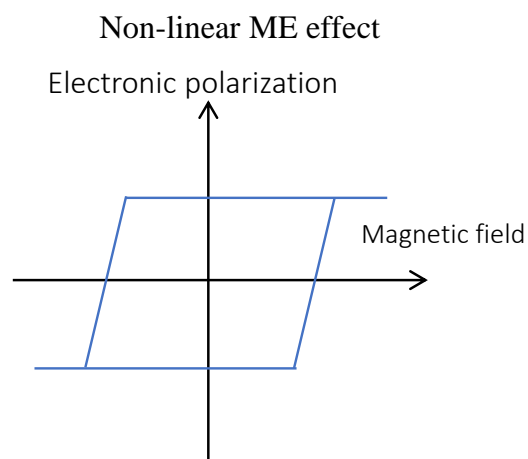


FIGURE 5.2: Conventional nonlinear ME response.

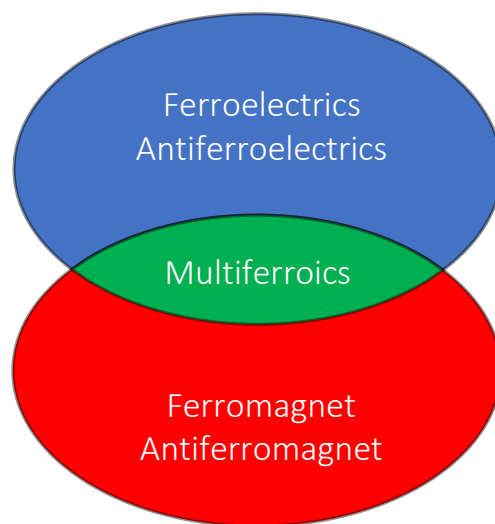


FIGURE 5.3: Venn diagram concerning multiferroics. Green region is the multiferroics which has both electric and magnetic order.

Chapter 6

Multiferroics and magnetoelectric effect

6.1 Linear magnetoelectric effect

The linear ME effect is firstly predicted by P. Curie [44]. The first discovery of the linear ME effect was found in Cr_2O_3 , which was predicted by I. E. Dzyaloshinskii [45] from the viewpoint of time-reversal and parity inversion symmetry. Soon after the prediction, the linear ME effect was realized in Cr_2O_3 [49, 50]. This section shows how the linear ME effect is described from the viewpoint of statistical mechanics.

In general, the free energy of the system is given via Landau expansion as

$$F(E, H) = F_0 - P_i^s E_i - M_i^s H_i - \frac{1}{2} \epsilon_0 \epsilon_{ij} E_i E_j - \frac{1}{2} \mu_0 \mu_{ij} H_i H_j - \alpha_{ij} E_i H_j - \frac{1}{2} \beta_{ijk} E_i H_j H_k - \frac{1}{2} \gamma_{ijk} H_i E_j E_k - \dots \quad (6.1)$$

with spontaneous polarization P^s , spontaneous magnetization M^s , electric susceptibilities $\hat{\epsilon}$, magnetic susceptibilities $\hat{\mu}$ and tensors α_{ij} , β_{ijk} , and γ_{ijk} which depend on the material's symmetric properties. The differentiations of the free energy are given as

$$P_i = -\frac{\partial F}{\partial E_i} = P_i^s + \frac{1}{2} \epsilon_0 \epsilon_{ij} E_j + \alpha_{ij} H_j + \frac{1}{2} \beta_{ijk} H_j H_k + \dots \quad (6.2)$$

and

$$M_i = -\frac{\partial F}{\partial H_i} = M_i^s + \frac{1}{2} \mu_0 \mu_{ij} H_j + \alpha_{ij} E_j + \frac{1}{2} \gamma_{ijk} E_j E_k + \dots, \quad (6.3)$$

where the third terms are the linear ME effect. Therefore, in general, the electronic polarization is linearly induced by not only the electronic fields \mathbf{E} , but also the magnetic fields \mathbf{H} when the tensor $\alpha \neq 0$.

The magnetic fields and the magnetization change their signs under the time-reversal operations, but not under the parity operations. In contrast, the electric fields and the electric polarization change their signs under parity operations, but not under the time-reversal operations. As a consequence, to have finite α , broken time-reversal and parity inversion symmetry are needed.

The microscopic origin of the linear ME effect is still controversial problem. Possible origin is believed toroidal moment, magnetic monopole and magnetic quadrupole. However, this thesis is mainly focusing on the non-linear ME effects. Therefore, this thesis does not elucidate those.

6.2 Ferroelectricity induced by magnetic orders (Giant magnetoelectric effect)

The linear ME effect is a rather small effect. Therefore, dedicated studies to make large ME effects have been done recently. Possible realization of such non-linear ME effects is achieved if the materials have spontaneous ferromagnetism or ferroelectricity. Moreover, roughly speaking, if there are some relations between magnetic orders and ferroelectricities, one can switch the electric polarization by the external magnetic fields. The non-linear ME effects are recently found in many frustrated magnets. The first discovery was in TbMnO_3 [46], which details will be described in Sec. 6.4. In which material, the non-linear ME effect is induced by the magnetic order.

The microscopic origin of the non-linear ME effects is still not completely understood yet. A key to understanding the non-linear ME effects is the symmetries of the materials. The crystal symmetry gives the following conditions for occurrence of spontaneous electric polarization [51, 52].

- The material should not have parity inversion and/or 3, 4 or 6 fold rotoinversion.
- If the material has n -rotational axis and/or mirror plane, only the P parallel to the axis and/or the mirror plane is possible.

From the symmetrical point of view, if the magnetic symmetry breaks such crystal symmetries, the material can have electronic polarization even if the material is forbidden to have the electronic polarization by the point group symmetry.

6.3 Microscopic mechanisms of the magnetically induced ferroelectricity

Microscopic understanding of the non-linear ME effects is the most important part of fundamental physics and applications. This section describes three mechanisms that are nowadays mainly used for understanding of the

magnetically induced ferroelectricities. As mentioned in Chap. 5, the theories are still controversial, and those theories are based on different standing points. However, it sometimes helps us to understand the magnetically induced ferroelectricities. Therefore, it is worthy of discussing those here.

- *Exchange striction mechanism*

There are some multiferroics in which the one-dimensional dimerization occurs. Let's think the substance has one-dimensional chains consist of magnetic ions M_A and M_B (Fig. 6.1(a)). In this system, pairs of M_A and M_B ions comprise spin-triplet pairs (Fig. 6.1(b)), which results in ferroelectricity of the substance. The antiferromagnetic Hamiltonian is then given as

$$H_{AF} = \sum_i J(i, i+1) \mathbf{S}_i \cdot \mathbf{S}_{i+1} \quad (6.4)$$

where the exchange coupling

$$J(i, i+1) \approx J + (u_i - u_{i+1})\alpha. \quad (6.5)$$

u_i is the displacements of atoms caused to acquire energy gains due to the dimerizations, α is a coefficient, respectively. This displacement is known as spin-Peierls instability [53]. This dimerization gives the net electronic polarization. As a result, one can have the following electronic polarization, which arises from isotropic interactions :

$$\mathbf{P}_{ij} \propto \mathbf{\Pi}_{ij}(\mathbf{S}_i \cdot \mathbf{S}_j) \quad (6.6)$$

where the vector $\mathbf{\Pi}_{ij}$ depends on the crystal structures. As real materials, the exchange striction mechanism can be used to describes the ME effect in RMnO_3 ($R = \text{Ho}, \text{Y}$) for example [54] which will be briefly discussed in Sec. 6.4.

- *Inverse Dzyaloshinskii-Moriya mechanism (Spin current mechanism)*

Another mechanism is called Inverse Dzyaloshinskii-Moriya (DM) mechanism. This mechanism is introduced by H. Katsura et. al. to explain magnetically induced ferroelectricity of cycloidal magnets in 2005 [55]. In the inverse DM mechanism, by thinking of the situation where the non-magnetic X ion is located at the center of a bond of the two magnetic ions M (Fig. 6.2(a)). Then the electronic dipole moment is given by

$$\mathbf{P}_{ij} \propto \mathbf{e}_{ij} \times (\mathbf{S}_i \times \mathbf{S}_j) \quad (6.7)$$

where the vector \mathbf{e}_{ij} is the vector connecting two neighboring sites. This mechanism is closely related to the Dzyaloshinskii-Moriya (DM) interaction of the magnetic energy which will be discussed in Sec. 7.4.2. The

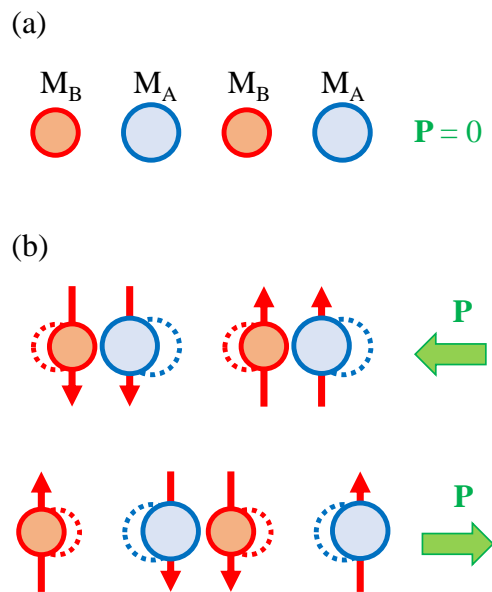


FIGURE 6.1: Schematic pictures of exchange striction mechanism and predicted direction of the electronic polarization by the exchange striction mechanism. Red and blue spheres indicate different two magnetic atoms are one-dimensionally aligned. (a) One-dimensional alignment of two magnetic ions, (b) Spin induced dimerization and (c) Another possible dimerization.

Eq. 6.7 gives the electronic polarization when the material has the cycloidal magnetic orders (See Fig. 6.2(b) and (c)). The inverse DM mechanism can successfully describe the ME effect of TbMnO_3 [48] which is also discussed in Sec. 6.4. The Eq. 6.7 indicates the direction of the electronic polarization induced by spiral magnets depends on the spin spiral propagation vectors.

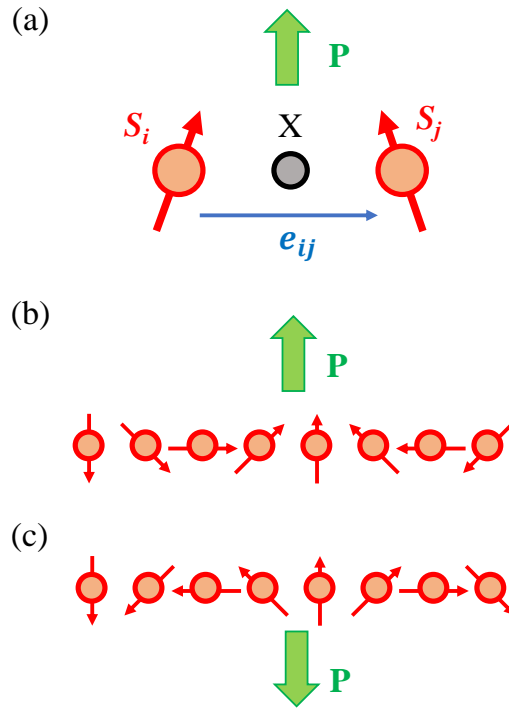


FIGURE 6.2: Schematic pictures of the Inverse DM mechanism. The magnetic ions and non-magnetic ligand ion is shown as red and black spheres, respectively. Blue arrow indicate the direction of the vector connecting neighboring two magnetic ions e_{ij} . Predicted direction of the electronic polarization is indicated by a green arrow in each picture (a-c). (a) The electronic polarization caused by the tilted two magnetic moments. (b,c) Cycloidal magnetic order and direction of the electronic polarization predicted by the inverse DM mechanism. Mirror operation flip the spin and direction of the electronic polarization (b→c).

- *d-p hybridization mechanism*

The last mechanism is called d-p hybridization mechanism [56–58]. The mechanism arises from the hybridization between d-orbital of the transition metals and p-orbital of the negative ions. This theory is based on the fact that this hybridization is modulated by the spins.

This d-p hybridization mechanism is adopted to a multiferroic CuFeO_2 which will be discussed in the following. In CuFeO_2 , hybridization of Fe d-orbital and O p-orbital is modulated by the spins.

Considering the spin-orbital interaction in a bond of the magnetic positive ions (M) and a non-magnetic negative ion (X) as shown in Fig. 6.3. The energy level difference of $l_z = \pm 1$ of d-orbital and p-orbital are perturbed by the spin-orbit interaction. By calculating contributions from d-orbital in a bonding orbital, one can have a spin-dependent part [58]. This indicates the electronic polarization is depending solely on the individual spin of a magnetic ion M which is formally given by

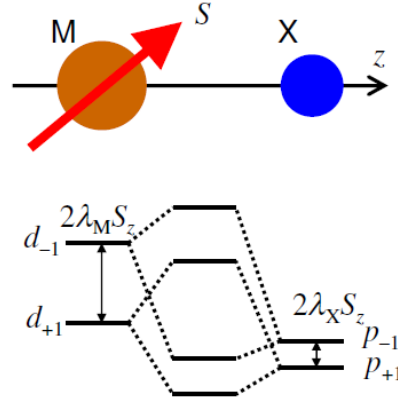


FIGURE 6.3: Schematic picture of the d-p hybridization between a magnetic ion (M) and a ligand ion (X). Bottom figure is showing the hybridization of d-orbital of M and p-orbital of X caused by the SOC. The picture is taken from [58].

$$P_{il} \propto (S_i \cdot e_{il})^2 e_{il} \quad (6.8)$$

where the vector e_{il} is pointing toward the bond direction.

6.4 Examples of multiferroic materials

As is explained, the microscopic theories introduced in the last section are based on the different standing points. However, this section shows the case in which those theories successfully described the magnetically induced electronic polarization as an example.

6.4.1 YMnO₃

A practical example of the multiferroics in which the ME effect is elucidated by the exchange striction mechanism is orthorhombic YMnO₃ [54, 59]. Crystal structure of the YMnO₃ is shown in (Fig. 6.4). The orthorhombic YMnO₃ shows the E-type ($\uparrow\uparrow\downarrow\downarrow$ -type) antiferromagnetic spin order in the low temperature phase (below 21 K). Above 50 K, it turns out to the paramagnetic phase.

In the antiferromagnetic phase, the electronic polarization along a-axis is observed in the experiments, but not in the paramagnetic phase [54, 59]. The antiferromagnetic interactions generate displacements of the oxygen atoms in the ferroelectric phase, but not in the paramagnetic phase (Fig. 6.4(c)). Thus the microscopic origin of the electronic polarization can be understood as the exchange striction mechanism. Direction of the electronic polarization is expected along a-axis as is observed in the experiments.

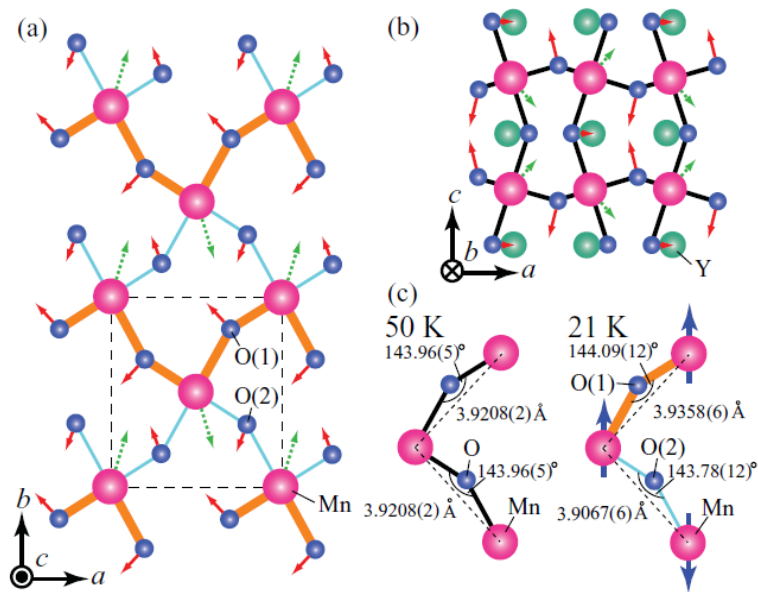


FIGURE 6.4: A schematic pictures of the orthorhombic $YMnO_3$. Large pink spheres and small blue spheres indicate Mn and O atoms, respectively. The expanded lattice in ab plane (a) and ac plane (b) are depicted. A dashed lined rectangle indicates the unit cell. Green dotted arrows and red solid arrows indicate the lattice displacements. (c) Difference of the bonds in the paramagnetic phase (50 K) and in the antiferromagnetic (ferroelectric) phase (21 K). Different bonds species in the antiferromagnetic phase are shown as orange and cyan lines, separately. The pictures are taken from [59].

6.4.2 $TbMnO_3$

T. Kimura et. al., reported the giant ME effect in orthorhombically distorted perovskite $TbMnO_3$ in 2003 [46]. The orthorhombic $TbMnO_3$ shows a sinusoidally modulated commensurate magnetic structure in $28\text{ K} < T < 41\text{ K}$. It turns out to the incommensurate spin spiral structure below 28 K. In the commensurate magnetic phase, ferroelectricity does not appear since the magnetic structure obeys spatial inversion symmetry. On the other hand, the

magnetic structure breaks the inversion symmetry in the spin spiral phase so as to an emergent of the electronic polarization [48].

Another interesting point is that in addition to the multiferroicity of this material, it shows spin spiral and electronic polarization flops upon the external magnetic fields. Fig. 6.5(a) shows the electronic polarization along c and a axis under various strength of the external magnetic fields along b -axis. One can see the electronic polarization is flopped by the external magnetic field along b -axis as $P \parallel c \rightarrow P \parallel a$. The spin spiral plane is also flopped by 90° (Fig. 6.5(b)).

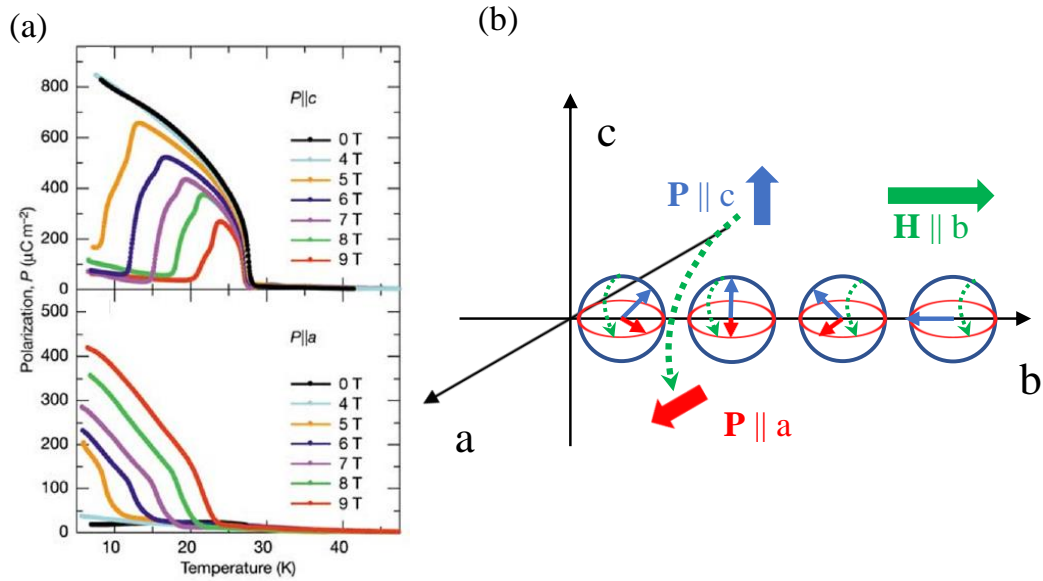


FIGURE 6.5: (a) Variations of the electronic polarization upon the external magnetic fields at the various temperatures along c -axis (above) and a -axis (below). This figure is taken from [46]. (b) A schematic picture of the spin plane flop and the associated electronic polarization flop induced by the external magnetic field along the b -axis.

The inverse DM mechanism successfully describes this ME effect which has been shown by Y. Yamasaki et. al., [60].

6.4.3 CuFeO_2

Kimura et. al., found the multiferroicity in delafossite CuFeO_2 [61]. Crystal structure belongs to rhombohedral space group and the structure is shown in Fig. 6.6. The valence of the Fe and Cu ions in this material are +3 and +1, respectively. Thus the Fe ion is the magnetic ion in this material. The delafossite CuFeO_2 shows a quite complicated magnetic phase. At the ground state, this material has a collinear four-sublattice spin ordering as $\uparrow\uparrow\downarrow\downarrow$ [62]. By applying the external magnetic fields, it shows various incommensurate and

commensurate magnetic structures [63] (Fig:6.7). The most important magnetic phase of this material is realized when the external field H ($7 \text{ T} < H < 13 \text{ T}$) is induced along c -axis. At this situation, the magnetic structure shows incommensurate proper screw order. Only this phase has the spontaneous electronic polarization hence the magnetically induced electronic polarization.

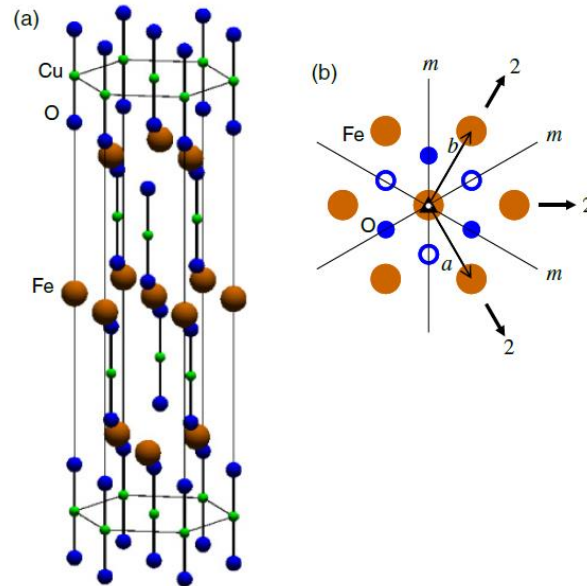


FIGURE 6.6: (a) Crystal structure of the delafossite CuFeO_2 . (b) 2D (001) plane of the Fe atoms. The triangle of the Fe atoms and O atoms are projected. Oxygen atoms belong to the upper and lower oxygen layers are shown as empty and filled blue spheres, respectively. Arrows indicate the twofold rotation axes. Black lines with the character m indicate the mirror planes and threefold rotation axes. The figure is taken from [58].

Important fact was that the observed electronic polarization is perpendicular to the c -axis. This material has an incommensurate spin spiral (proper screw type) magnetic order, therefore, the inverse DM should be able to describe the ME effect of this material. However, with the proper screw type magnetic order, the inverse DM mechanism predicts no electronic polarization. Therefore this system is known as a typical case in which the inverse DM mechanism fails to describe the ME effect. Another possibility is the exchange striction mechanism. However, the exchange striction mechanism is not applicable in this case either because the ferroelectricity appears only in the spin spiral phase and only one magnetic ion is contained in the unit cell.

T. Arima showed the d - p hybridization mechanism describes the ferroelectricity observed in the CuFeO_2 [58]. The d - p hybridization mechanism successfully predicted the electronic polarization along c -axis as observed in the experiments [61].

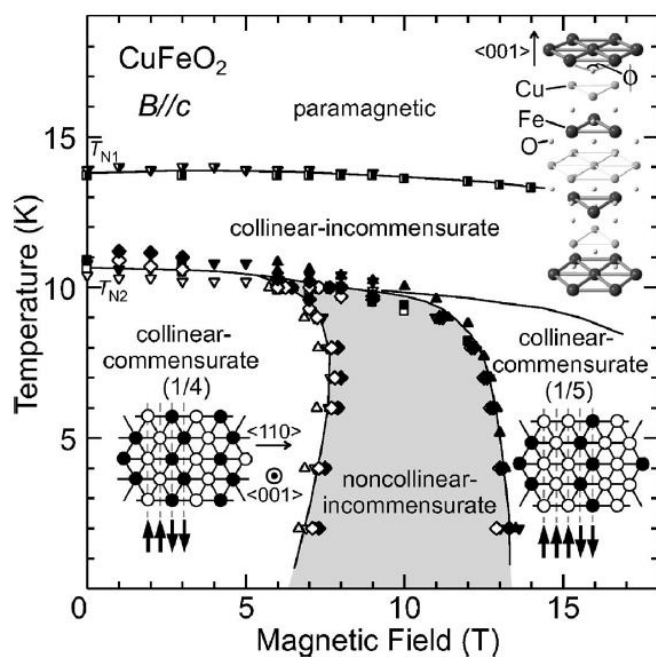


FIGURE 6.7: Magnetic phase diagram of the delafossite CuFeO_2 regarding the external magnetic fields and the temperature. The figure is taken from [61].

Chapter 7

Theory for strongly correlated materials

Chap. 6 described the examples of the multiferroics and already suggested mechanisms. The multiferroicities are the property of strongly correlated materials. Nowadays the first-principle density functional theory (DFT) is widely used to investigate the electronic structure of various materials. DFT is however limited when it treats the strongly correlated materials like multiferroics because of the approximation used in exchange correlation functional. One possible approach is low-energy models in which the electron correlations are taken into account properly. This chapter accesses those theories which are usually used in analysis of the strongly correlated materials and will be used to investigate multiferroic property of the spiral magnet BaCuGe₂O₇ in Chap. 8.

7.1 Hubbard model

As mentioned above, accuracy of the widely used local density approximation (LDA) based DFT is questionable when it treats strongly correlated materials. J. Hubbard introduced an effective lattice model of low-energy bands which treats the electron correlations explicitly [64]. The model is known as Hubbard model and general form is given by

$$\hat{\mathcal{H}} = \sum_{ij} \sum_{\sigma\sigma'} \sum_{ab} t_{ij}^{ab\sigma\sigma'} \hat{c}_{ia\sigma}^\dagger \hat{c}_{jb\sigma'} + \frac{1}{2} \sum_i \sum_{\sigma\sigma'} \sum_{abcd} U^{abcd} \hat{c}_{ia\sigma}^\dagger \hat{c}_{ic\sigma'}^\dagger \hat{c}_{ib\sigma} \hat{c}_{id\sigma'}, \quad (7.1)$$

where $t_{ij}^{ab\sigma\sigma'}$, $\hat{c}_{ia\sigma}^\dagger$, $\hat{c}_{ia\sigma}$ and U^{abcd} are the hopping energies of the electrons at site i to j , the creation operator of the electron with site i , spin σ and orbital a and b , the annihilation operator of it and the on-site screened Coulomb interactions, respectively. Matrix elements of the Coulomb interactions are given by

$$U^{abcd} = \int \int d\mathbf{r} d\mathbf{r}' \phi_a^*(\mathbf{r}) \phi_b^*(\mathbf{r}) W_r(\mathbf{r}, \mathbf{r}') \phi_c(\mathbf{r}') \phi_d(\mathbf{r}') \quad (7.2)$$

with the appropriately chosen atomic-like wave functions ϕ and partially screened Coulomb interaction $W_r(\mathbf{r}, \mathbf{r}')$. The on-site Coulomb matrix U_{abcd}

consists of following three independent parameters

$$U^{mmmm} = U = \int \int d\mathbf{r} d\mathbf{r}' |\phi_m(\mathbf{r})|^2 W_r(\mathbf{r}, \mathbf{r}') |\phi_m(\mathbf{r}')|^2 \quad (7.3)$$

$$U^{mm'm'm'} = U' = \int \int d\mathbf{r} d\mathbf{r}' |\phi_m(\mathbf{r})|^2 W_r(\mathbf{r}, \mathbf{r}') |\phi_{m'}(\mathbf{r}')|^2 \quad (7.4)$$

$$U^{mm'm'm} = J = \int \int d\mathbf{r} d\mathbf{r}' \phi_m^*(\mathbf{r}) \phi_{m'}(\mathbf{r}) W_r(\mathbf{r}, \mathbf{r}') \phi_{m'}^*(\mathbf{r}') \phi_m(\mathbf{r}') \quad (7.5)$$

where U and U' are the on-site intra and inter orbital Coulomb interaction. J is the intra atomic Hund's exchange coupling constant. A simple cartoon of the model is depicted in Fig. 7.1. The first term of the Eq. 7.1, the one-electron part of the Hamiltonian, gives "band effect" which is the result of the moves of the electrons around the lattice. The second term is the Coulomb interactions. The diagonal elements of the one-electron part $t_{ij}^{ab\sigma\sigma'}$ represent the crystal field splittings and/or relativistic spin-orbit interactions.

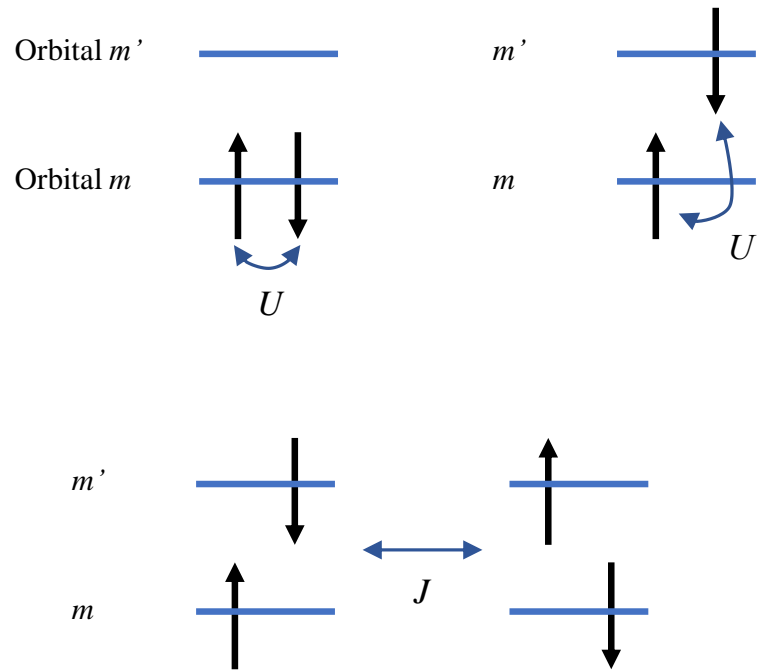


FIGURE 7.1: Schematic pictures of meanings of each Coulomb interaction parameter.

Thus, the one-electron part is decomposed as :

$$\hat{\mathcal{H}}_{\text{one}} = \hat{\mathcal{H}}_{\text{kin}} + \hat{\mathcal{H}}_{\text{CF}} + \hat{\mathcal{H}}_{\text{SOC}}, \quad (7.6)$$

where $\hat{\mathcal{H}}_{\text{kin}}$ is kinetic energy, $\hat{\mathcal{H}}_{\text{CF}}$ is crystal-field splittings and $\hat{\mathcal{H}}_{\text{SOC}}$ is the relativistic spin-orbit interaction.

7.1.1 One-electron part in d-orbital case

This subsection shows a practical form of the the one-electron part of the Hubbard model. Main interest of this thesis is the d-orbital, therefore, d-orbital is chosen as the model. Here we assume the cubic symmetry, then, the on-site term (crystal-field and spin-orbit interaction) is given as

$$\hat{\mathcal{H}}_{\text{CF}} + \hat{\mathcal{H}}_{\text{SOC}} = \begin{pmatrix} \mu_{t_{2g}} & 0 & 0 & 0 & 0 \\ 0 & \mu_{t_{2g}} & 0 & 0 & 0 \\ 0 & 0 & \mu_{e_g} & 0 & 0 \\ 0 & 0 & 0 & \mu_{t_{2g}} & 0 \\ 0 & 0 & 0 & 0 & \mu_{e_g} \end{pmatrix} \hat{\sigma}_0 + \frac{\zeta}{2} i \begin{pmatrix} 0 & \hat{\sigma}_y & 0 & -\hat{\sigma}_x & 2\hat{\sigma}_z \\ -\hat{\sigma}_y & 0 & -\sqrt{3}\hat{\sigma}_x & -\hat{\sigma}_z & -\hat{\sigma}_x \\ 0 & \sqrt{3}\hat{\sigma}_x & 0 & -\sqrt{3}\hat{\sigma}_y & 0 \\ \hat{\sigma}_x & -\hat{\sigma}_z & -\sqrt{3}\hat{\sigma}_y & 0 & -\hat{\sigma}_y \\ -2\hat{\sigma}_x & i\hat{\sigma}_x & 0 & \hat{\sigma}_y & 0 \end{pmatrix}, \quad (7.7)$$

where $\mu_{e_g} - \mu_{t_{2g}}$ is the crystal field splitting between t_{2g} and e_g orbital, $\hat{\sigma}_0$ is the unit matrix, ζ is the spin-orbit coupling constant and $\hat{\sigma} = (\hat{\sigma}_x, \hat{\sigma}_y, \hat{\sigma}_z)$ is the vector of the Pauli matrices, respectively [65]. The orbital order of these matrices is d_{xy} , d_{yz} , d_{z^2} , d_{zx} and $d_{x^2-y^2}$. This indicates the energy level is splitted by the crystal-field, then, it will be splitted further by the spin-orbit couplings. The kinetic energy term $\hat{\mathcal{H}}_{\text{kin}}$ is given as the off-site term ($i \neq j$).

7.2 Wannier function

How to adapt the Hubbard model to real materials? Since the DFT calculations are considered enough to describe the one-electron part of the Hamiltonian, one of the most reliable procedure is to use the electronic structures obtained from DFT calculations as the starting points and construct effective low-energy models. This procedure is called realistic modeling and used in numerous studies (e.g. [65–67]). As a practical procedure, one construct atomic-like wave functions as the basis function from the electronic structures. Most successful and widely used function is Wannier function [68].

Main concept of the Wannier functions is the Fourier transformation of the Bloch functions which is given by

$$|\mathbf{R}n\rangle = \frac{V}{(2\pi)^3} \int d\mathbf{k} e^{-i\mathbf{k}\cdot\mathbf{R}} |\psi_{n\mathbf{k}}\rangle, \quad (7.8)$$

so that

$$|\psi_{n\mathbf{k}}\rangle = \sum_{\mathbf{R}} e^{i\mathbf{k}\cdot\mathbf{R}} |\mathbf{R}n\rangle. \quad (7.9)$$

Here \mathbf{R} is lattice vectors and V is the unit cell volume. Here \mathbf{R} is lattice vectors and V is the unit cell volume. The periodic part of Bloch function is defined as

$$u_{n\mathbf{k}}(\mathbf{r}) = e^{-i\mathbf{k}\cdot\mathbf{r}} \psi_{n\mathbf{k}}(\mathbf{r}). \quad (7.10)$$

An important fact is that the Wannier function has an arbitrariness. This can be easily realized from the Bloch function Eq. 7.10 with an arbitrary gauge $e^{i\phi_n(\mathbf{k})}$. Bloch function is then given by

$$|\tilde{\psi}_{n\mathbf{k}}\rangle = e^{i\phi_n(\mathbf{k})} |\psi_{n\mathbf{k}}\rangle \quad (7.11)$$

or equivalently

$$|\tilde{u}_{n\mathbf{k}}\rangle = e^{i\phi_n(\mathbf{k})} |u_{n\mathbf{k}}\rangle. \quad (7.12)$$

This Bloch orbital describes the same physics. Then the Wannier function is given as

$$|\mathbf{R}n\rangle = \frac{V}{(2\pi)^3} \int e^{i\phi_n(\mathbf{k})} e^{-i\mathbf{R}\cdot\mathbf{k}} |\psi_{n\mathbf{k}}\rangle d\mathbf{k}. \quad (7.13)$$

This Wannier function gives different shape and spreads with those of Eq. 7.8. Namely, Wannier function is not unique, but still valid. In multi-band cases, this gauge freedom is given by a unitary matrix as

$$|\tilde{\psi}_{n\mathbf{k}}\rangle = \sum_{m=1}^N U_{mn}^{(\mathbf{k})} |\psi_{m\mathbf{k}}\rangle, \quad (7.14)$$

where N is the number of bands in the set of bands and $U_{mn}^{(\mathbf{k})}$ is the $N \times N$ unitary matrix. Algorithms to produce desired unitary matrix or, equivalently, the set of Wannier functions will be discussed below.

7.2.1 Maximally localized Wannier function

Marzari et. al., introduced an algorithm to construct maximally localized Wannier functions (MLWF) [69, 70]. In the MLWF procedure, Wannier functions are constructed to minimize the spread functional which is defined as

$$\Omega \equiv \sum_n [\langle \mathbf{0}n | r^2 | \mathbf{0}n \rangle - \langle \mathbf{0}n | \mathbf{r} | \mathbf{0}n \rangle^2] = \sum_n [\langle r^2 \rangle_n - \bar{r}_n^2] \quad (7.15)$$

where $\langle r^2 \rangle_n$ and \bar{r}_n are the matrix elements of the position operator and the square of the position operator. Those are generally given as

$$\langle \mathbf{R}n | \mathbf{r} | \mathbf{0}m \rangle = i \frac{V}{(2\pi)^3} \int d\mathbf{k} e^{i\mathbf{k}\cdot\mathbf{R}} \langle u_{n\mathbf{k}} | \nabla_{\mathbf{k}} | u_{m\mathbf{k}} \rangle \quad (7.16)$$

and

$$\langle \mathbf{R}n | r^2 | \mathbf{0}m \rangle = -\frac{V}{(2\pi)^3} \int d\mathbf{k} e^{i\mathbf{k}\cdot\mathbf{R}} \langle u_{n\mathbf{k}} | \nabla_{\mathbf{k}}^2 | u_{m\mathbf{k}} \rangle, \quad (7.17)$$

respectively [71]. A simple condition can be derived as the consequence by introducing matrix elements of the Bloch functions as

$$M_{mn}^{(\mathbf{k},\mathbf{b})} = \langle u_{m\mathbf{k}} | u_{n\mathbf{k}+\mathbf{b}} \rangle, \quad (7.18)$$

where \mathbf{b} is a vector connecting each \mathbf{k} -point to its neighbors. The condition is then given as a minimization of

$$G_{mn}^{(\mathbf{k})} = \frac{d\Omega}{dW_{mn}^{(\mathbf{k})}} = 4 \sum_{\mathbf{b}} w_{\mathbf{b}} (A[R_{mn}^{(\mathbf{k},\mathbf{b})}] - S[T_{mn}^{(\mathbf{k},\mathbf{b})}]), \quad (7.19)$$

where $dW_{mn}^{(\mathbf{k})}$ is an infinitesimal gauge transformation defined as

$$U_{mn}^{(\mathbf{k})} = \delta_{mn} + dW_{mn}^{(\mathbf{k})}, \quad (7.20)$$

$R_{mn}^{(\mathbf{k},\mathbf{b})}$ and $\tilde{R}_{mn}^{(\mathbf{k},\mathbf{b})}$ are defined as

$$R_{mn}^{(\mathbf{k},\mathbf{b})} = dM_{mn}^{(\mathbf{k},\mathbf{b})} dM_{nn}^{(\mathbf{k},\mathbf{b})*} \quad \text{and} \quad \tilde{R}_{mn}^{(\mathbf{k},\mathbf{b})} = \frac{dM_{mn}^{(\mathbf{k},\mathbf{b})}}{dM_{nn}^{(\mathbf{k},\mathbf{b})*}}, \quad (7.21)$$

$T_{mn}^{(\mathbf{k},\mathbf{b})}$ is defined as

$$T_{mn}^{(\mathbf{k},\mathbf{b})} = \tilde{R}_{mn}^{(\mathbf{k},\mathbf{b})} q_n^{(\mathbf{k},\mathbf{b})}, \quad (7.22)$$

with

$$q_n^{(\mathbf{k},\mathbf{b})} = \text{Im} \ln M_{nn}^{(\mathbf{k},\mathbf{b})} + \mathbf{b} \cdot \bar{\mathbf{r}}_n \quad (7.23)$$

$w_{\mathbf{b}}$ is an associated weight for each shell $|\mathbf{b}| = b$ such that $\sum_{\mathbf{b}} w_{\mathbf{b}} b_{\alpha} b_{\beta} = \delta_{\alpha\beta}$ (see Appendix B of [69] for the notations), respectively. $A[R_{mn}^{(\mathbf{k},\mathbf{b})}]$ and $S[T_{mn}^{(\mathbf{k},\mathbf{b})}]$ are given by the following relations

$$\frac{d\text{tr}[dWB]}{dW} = B, \quad (7.24)$$

$$\frac{d\text{Re tr}[dWB]}{dW} = A[B], \quad (7.25)$$

$$\frac{d\text{Im tr}[dWB]}{dW} = S[B], \quad (7.26)$$

where $A[B] = (B - B^{\dagger})/2$ and $S[B] = (B + B^{\dagger})/2i$.

General form of the tight-binding hopping parameters of the Hubbard model in Eq. 7.1 is given via the Wannier functions as

$$t_{nm}(\mathbf{R}) = \langle \mathbf{R}n | \hat{\mathcal{H}}_{\text{one}} | \mathbf{0}m \rangle, \quad (7.27)$$

where $\hat{\mathcal{H}}_{\text{one}}$ is the one-electron Hamiltonian which is used in the DFT calculations. An usual setting is to use local density approximation [38] based approximations as $\hat{\mathcal{H}}_{\text{one}} = \hat{\mathcal{H}}_{\text{LDA}}$.

7.2.2 Selectively localized Wannier function

Another approach is introduced by Wang et. al. [72]. This approach is called selectively localized Wannier function (SLWF) method. In the SLWF approach, with an additional constraint on the spread functional Eq. 7.15, one can force the Wannier functions to have some condition. For example, force the Wannier functions centers to be on the exact atomic positions. The condition of the spread functional with the additional constraint Ω_c is then given by

$$\Omega_c = \sum_n [\langle r^2 \rangle_n - \bar{r}_n^2 + \lambda_c (\bar{r}_n - \mathbf{r}_{0n})^2] \quad (7.28)$$

where λ_c is a Lagrange multiplier, \mathbf{r}_{0n} is a constraint of the n th Wannier function.

7.2.3 Modified maximally localized Wannier function

The MLWF method is the most straightforward algorithm to construct localized atomic-like Wannier functions. One problem is there is no condition regarding the crystal structures in MLWF method. This gives unphysical results because the Hamiltonian should have crystallographic symmetry properties of the materials. Therefore, we have introduced a modification of MLWF [73]. In this method, the spread functional of the Wannier functions Ω_{mod} is defined as

$$\begin{aligned} \Omega_{\text{mod}} &\equiv \sum_n \langle (\mathbf{r} - \mathbf{r}_{0i})^2 \rangle_n \\ &= \sum_n [\langle r^2 \rangle_n - 2\mathbf{r}_{0i} \cdot \bar{\mathbf{r}}_n + r_{0i}^2] \\ &= \sum_n [\langle r^2 \rangle_n - r_{0i}^2], \end{aligned} \quad (7.29)$$

where

$$\mathbf{r}_{0i} = \frac{1}{N_i} \sum_{n \in i} \bar{\mathbf{r}}_n \quad (7.30)$$

is an averaged Wannier center over a set of N_i Wannier functions of an atom i . Minimization of the modified spread functional Eq. 7.29 is easily realized

just by replacing a modified $q_n^{(k,b)}$ instead of original $q_n^{(k,b)}$ Eq. 7.23. $q_n^{(k,b)}$ in this modified MLWF method is given by

$$(q_n^{(k,b)})_{\text{mod}} = \text{Im} \ln M_{nn}^{(k,b)} + \mathbf{b} \cdot \mathbf{r}_{0i}. \quad (7.31)$$

With a condition $\mathbf{r}_{0i} = \bar{\mathbf{r}}_n$ this method coincides with the original MLWF method.

7.3 Constrained Random Phase Approximation

The remaining parameters of the model Eq. 7.1 are the on-site Hubbard U . Since the screened U is a purely many-body effect, the question is how to calculate U from the one-electron DFT calculations. A simple approach is determining these parameters by hand. This approach is widely used especially in LDA+U method [74]. However, this approach is not reliable as the parameters are adjusted just from the view point of the consistency of the electronic structure with experiments. One of the logical procedure is including many body effects as the screenings and downfolding degrees of freedoms out of range of the low-energy region (far from the Fermi level). This approach is introduced by Aryasetiawan et. al. [75, 76]. The approach is called constrained Random Phase Approximation (cRPA).

The fully screened Coulomb interaction W in the matrix form is given by Random Phase Approximation (RPA) as

$$W = v + v\chi_0v + v\chi_0v\chi_0v + \dots = (1 - v\chi_0)^{-1}v, \quad (7.32)$$

where v is the bare Coulomb interactions, χ_0 is the independent particle polarization function. By dividing the polarization function in the model Hilbert space (d) and the rest of it (r), the polarization function is represented as

$$\chi_0 = \chi_0^d + \chi_0^r. \quad (7.33)$$

Fig. 7.2 shows a schematic picture of the model and rest subspace.

From Eq. 7.32 and Eq. 7.33, one can have

$$W = (1 - v\chi_0^d - v\chi_0^r)^{-1}v \quad (7.34)$$

$$= \left[\epsilon_r (1 - \epsilon_r^{-1}v\chi_0^d) \right]^{-1} v \quad (7.35)$$

$$= (1 - \epsilon_r^{-1}v\chi_0^d) \epsilon_r^{-1}v \quad (7.36)$$

$$= (1 - W_r\chi_0^d)W_r, \quad (7.37)$$

where ϵ is the dielectric function defined as

$$\epsilon = 1 - v\chi_0 \quad (7.38)$$

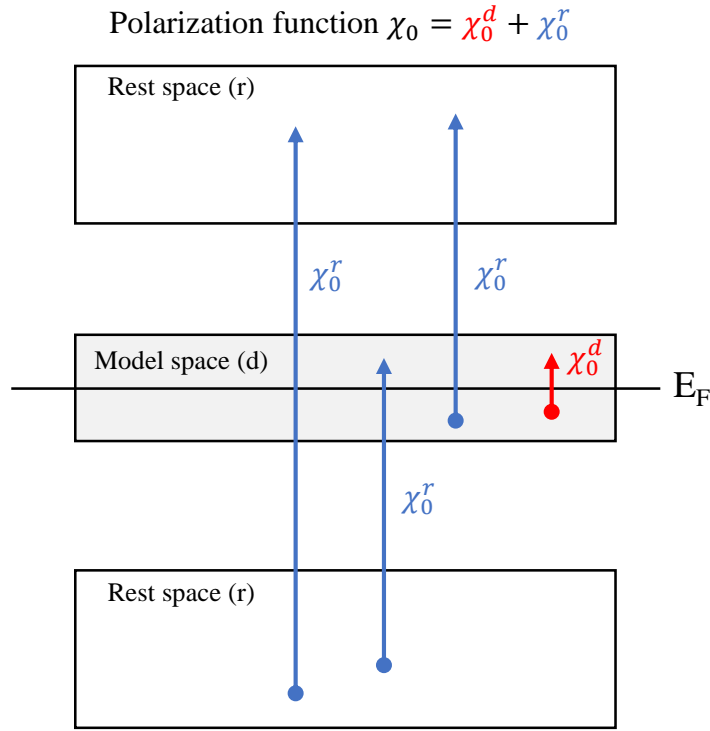


FIGURE 7.2: Schematic picture of the transition between model (d) and rest (r) subspace.

of the subspace r ϵ_r , relations

$$W = \epsilon^{-1}v \quad (7.39)$$

and

$$W_r = (1 - v\chi_0^r)^{-1}v = \epsilon_r^{-1}v \quad (7.40)$$

are used implicitly.

The Eq. 7.37 indicates the screening in the model χ_0^d gives fully screened Coulomb interaction, therefore, one can realize W_r is equivalent to Hubbard U . Hence, the Eq. 7.2 is justified. However, in practice, the Hubbard U is frequently dependent due to time dependent perturbations caused by an external electron which result in retarded screening effects. A static limit defined as

$$W_r(\mathbf{r}, \mathbf{r}'; 0) \equiv W_r(\mathbf{r}, \mathbf{r}') \quad (7.41)$$

can be used in practice.

7.3.1 Practical case

A practical calculation of the Hubbard U is shown in the following.

From the generalized relation of Eq. 7.9:

$$\psi_{\alpha k}(\mathbf{r}) = \sum_{m, \mathbf{R}} e^{i\mathbf{k} \cdot \mathbf{R}} U_{m\alpha}^{\dagger(\mathbf{k})} w_{\mathbf{R}m}(\mathbf{r}) \quad (7.42)$$

with a unitary matrix $U_{m\alpha}^{(\mathbf{k})}$ and m th Wannier function $w_{\mathbf{R}m}(\mathbf{r})$, one can have the polarization function of the model subspace χ_0^d as

$$\begin{aligned} \chi_0^d(\mathbf{r}, \mathbf{r}') &= 2 \sum_{\alpha, \beta \in d} \sum_{\mathbf{k}, \mathbf{k}'} \frac{f_{\beta \mathbf{k}'} - f_{\alpha \mathbf{k}}}{\epsilon_{\beta \mathbf{k}'} - \epsilon_{\alpha}} \psi_{\alpha \mathbf{k}}^*(\mathbf{r}) \psi_{\beta \mathbf{k}'}(\mathbf{r}) \psi_{\beta \mathbf{k}'}^*(\mathbf{r}') \psi_{\alpha \mathbf{k}}(\mathbf{r}') \quad (7.43) \\ &= 2 \sum_{m \cdots p} \sum_{\mathbf{R}_1, \cdots, \mathbf{R}_4} \sum_{\alpha \beta \in d} \sum_{\mathbf{k}, \mathbf{k}'} \frac{f_{\beta \mathbf{k}'} - f_{\alpha \mathbf{k}}}{\epsilon_{\beta \mathbf{k}'} - \epsilon_{\alpha}} e^{-i\mathbf{k} \cdot (\mathbf{R}_1 - \mathbf{R}_4)} e^{i\mathbf{k}' \cdot (\mathbf{R}_2 - \mathbf{R}_3)} \\ &\times \left(U_{m\alpha}^{\dagger(\mathbf{k})} \right)^* U_{n\beta}^{\dagger(\mathbf{k}')} \left(U_{o\beta}^{\dagger(\mathbf{k}')} \right)^* U_{p\alpha}^{\dagger(\mathbf{k})} w_{\mathbf{R}_1 m}^*(\mathbf{r}) w_{\mathbf{R}_2 n}(\mathbf{r}) w_{\mathbf{R}_3 o}^*(\mathbf{r}') w_{\mathbf{R}_4 p}(\mathbf{r}'), \quad (7.44) \end{aligned}$$

where $m - p$, $\mathbf{R}_1 - \mathbf{R}_4$ and $\{f_{\alpha \mathbf{k}}\}$ are the orbital, the lattice indices and the occupancies [77]. The coefficient 2 of the polarization comes from the sum of spins. The rest of the polarization function is then calculated from Eq. 7.33 with

$$\chi_0(\mathbf{r}, \mathbf{r}') = 2 \sum_{\alpha, \beta} \sum_{\mathbf{k}, \mathbf{k}'} \frac{f_{\beta \mathbf{k}'} - f_{\alpha \mathbf{k}}}{\epsilon_{\beta \mathbf{k}'} - \epsilon_{\alpha}} \psi_{\alpha \mathbf{k}}^*(\mathbf{r}) \psi_{\beta \mathbf{k}'}(\mathbf{r}) \psi_{\beta \mathbf{k}'}^*(\mathbf{r}') \psi_{\alpha \mathbf{k}}(\mathbf{r}'). \quad (7.45)$$

Then the Hubbard U is evaluated from Eq. 7.40 with bare Coulomb interaction v . Matrix elements of the bare Coulomb interaction are given by

$$v_{m'n'o'p'} = \int d\mathbf{r} d\mathbf{r}' w_{\mathbf{R}_1 m}^*(\mathbf{r}) w_{\mathbf{R}_2 n}(\mathbf{r}) \frac{1}{|\mathbf{r} - \mathbf{r}'|} w_{\mathbf{R}_3 o}^*(\mathbf{r}') w_{\mathbf{R}_4 p}(\mathbf{r}'), \quad (7.46)$$

where $m' - p'$ are combined indices of $m - n$ and $\mathbf{R}_1 - \mathbf{R}_4$. Then, one has Coulomb interactions between all sites, however, for the Hubbard model, only on-site Coulomb interactions are needed. Therefore, one can have much simpler forms with the on-site condition $\mathbf{R}_1 = \mathbf{R}_2 = \mathbf{R}_3 = \mathbf{R}_4$.

7.4 Spin Hamiltonian

Strong correlations give rise to certain magnetic orders as widely known. Magnetism is a property of the materials. The most straightforward way to understand the macroscopic magnetic property is evaluating it by a physical parameter magnetization M . The magnetization M is determined from a macroscopic average of microscopic magnetic moments $\{\boldsymbol{\mu}\}$ as

$$M \propto \langle \boldsymbol{\mu} \rangle. \quad (7.47)$$

The microscopic magnetic moment of an atom i is given as

$$\boldsymbol{\mu}_i = -g\mu_B\mathbf{S}_i, \quad (7.48)$$

where g is so-called Landé g -factor (approximately $g \approx 2$), μ_B is the Bohr magneton which is defined as

$$\mu_B = \frac{e\hbar}{2mc} \quad (7.49)$$

and \mathbf{S}_i is the composed spin moment concerning the atom i . As a consequence, understanding microscopic spins are the essential problem of the magnetism. In the field of the magnetism, so-called spin Hamiltonian approach is used to investigate microscopic magnetism of the materials. In the spin Hamiltonian approach, the ground states are solely determined by spins of the magnetic ions.

The practical form of the spin Hamiltonian will be rigorously derived from exchange interactions in the following subsections.

7.4.1 Heisenberg model

The most widely known spin Hamiltonian is so-called Heisenberg model which is given by

$$\hat{\mathcal{H}}_{\text{Heis}} = -\sum_{i,j} J_{ij}\mathbf{S}_i \cdot \mathbf{S}_j. \quad (7.50)$$

This expression can be obtained from direct exchange mechanism as shown in the following.

Consider only two electrons and its orbital ϕ_a and ϕ_b for the sake of simplicity (see Fig. 7.3 for a simple cartoon). As is well known, the eigenstates are spin-singlet ($\mathbf{S} = 0$) and spin-triplet ($\mathbf{S} = 1$). By introducing ket vector for the spinor (e.g. $|\uparrow\downarrow\rangle$ is up spin at site a and down spin at site b), spin-singlet and triplet states are given as :

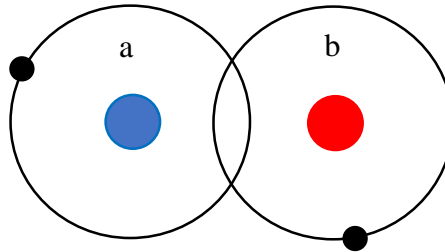


FIGURE 7.3: Simple cartoon of the two orbital model.

- Singlet : $S = 0$

$$\frac{1}{\sqrt{2}}(|\uparrow\downarrow\rangle - |\downarrow\uparrow\rangle) \quad (7.51)$$

- Triplet : $S = 1$

$$\begin{aligned} & |\uparrow\uparrow\rangle, \\ & \frac{1}{\sqrt{2}}(|\uparrow\downarrow\rangle + |\downarrow\uparrow\rangle), \\ & |\downarrow\downarrow\rangle. \end{aligned} \quad (7.52)$$

With the orbital parts of the spin-singlet ϕ_s and spin-triplet ϕ_t

$$\phi_s(\mathbf{r}, \mathbf{r}') = \frac{1}{\sqrt{2}}(\phi_a(\mathbf{r})\phi_b(\mathbf{r}') + \phi_b(\mathbf{r})\phi_a(\mathbf{r}')), \quad (7.53)$$

$$\phi_t(\mathbf{r}, \mathbf{r}') = \frac{1}{\sqrt{2}}(\phi_a(\mathbf{r})\phi_b(\mathbf{r}') - \phi_b(\mathbf{r})\phi_a(\mathbf{r}')). \quad (7.54)$$

$$(7.55)$$

Coulomb interactions for singlet and triplet states are then

$$\epsilon_{\text{singlet}} = \langle \phi_s | \frac{1}{|\mathbf{r} - \mathbf{r}'|} | \phi_s \rangle = U'_{ab} + J_{ab} \quad (7.56)$$

and

$$\epsilon_{\text{triplet}} = \langle \phi_t | \frac{1}{|\mathbf{r} - \mathbf{r}'|} | \phi_t \rangle = U'_{ab} - J_{ab}, \quad (7.57)$$

where

$$U'_{ab} = \int \int d\mathbf{r} d\mathbf{r}' |\phi_a(\mathbf{r})|^2 \frac{1}{|\mathbf{r} - \mathbf{r}'|} |\phi_b(\mathbf{r}')|^2 \quad (7.58)$$

$$J_{ab} = \int \int d\mathbf{r} d\mathbf{r}' \phi_a^*(\mathbf{r})\phi_b(\mathbf{r}) \frac{1}{|\mathbf{r} - \mathbf{r}'|} \phi_b^*(\mathbf{r}')\phi_a(\mathbf{r}'). \quad (7.59)$$

As an explicit representation regarding spins, by a relation of the spin operators

$$\mathbf{S}^2 = S(S+1) = (\mathbf{S}_a + \mathbf{S}_b)^2 = \mathbf{S}_a^2 + \mathbf{S}_b^2 + 2\mathbf{S}_a \cdot \mathbf{S}_b = \frac{3}{2} + 2\mathbf{S}_a \cdot \mathbf{S}_b, \quad (7.60)$$

the energies can be expressed as

$$E = U'_{ab} - \frac{J_{ab}}{2} - 2J_{ab}\mathbf{S}_a \cdot \mathbf{S}_b \quad (7.61)$$

$\mathbf{S}_a \cdot \mathbf{S}_b = -\frac{3}{4}$ and $\mathbf{S}_a \cdot \mathbf{S}_b = \frac{1}{4}$ are corresponding to spin-singlet and spin-triplet, respectively.

Only the last term of Eq. 7.61 is spin dependent. This term is called isotropic Heisenberg interaction. Thus the general form of the Heisenberg interaction is given by Eq. 7.50. A practical evaluation of the exchange parameter J_{ab} will be shown in the following.

Another mechanism is kinetic exchange. In the kinetic exchange, energy difference between a pair of parallel spins ϵ_p and anti-parallel spins ϵ_a is given as

$$\epsilon_a - \epsilon_p = 2J. \quad (7.62)$$

In the large U limit of Hubbard model, meaning $U \gg t$, the energy gain acquired by virtual hopping from orbital a to b and vice versa (See Fig. 7.4 for a simple image) is given by the second order perturbation as

$$\epsilon_a = \frac{\langle b | \hat{\mathcal{H}}_{\text{one}} | a \rangle \langle a | \hat{\mathcal{H}}_{\text{one}} | b \rangle}{U'_{ab} - U_b} = \frac{|t_{ab}|^2}{U'_{ab} - U_b}, \quad (7.63)$$

with the hopping parameter t_{ab} between orbital a and b and U_b is the intra orbital Coulomb interaction defined as

$$U_b = \int \int d\mathbf{r} d\mathbf{r}' |\phi_b(\mathbf{r})|^2 \frac{1}{|\mathbf{r} - \mathbf{r}'|} |\phi_b(\mathbf{r}')|^2. \quad (7.64)$$

Since there is no hopping amplitudes for the parallel spins, J is simply given as Eq. 7.63. Usually, $U_b > U'_{ab}$, thus the antiferromagnetic interaction. If the virtual hopping is mediated by a non-magnetic ion, the mechanism is called superexchange mechanism. Details of the superexchange mechanism is described in Sec. 7.5.

7.4.2 Dzyaloshinskii-Moriya interaction

Another well known interaction between spins is Dzyaloshinskii-Moriya (DM) interaction. It is given by

$$\mathbf{D}_{ij} \cdot (\mathbf{S}_i \times \mathbf{S}_j) \quad (7.65)$$

where \mathbf{D}_{ij} is so-called DM vector between the site i and j . Firstly, I. E. Dzyaloshinskii introduced this mechanism from the phenomenological point of view in order to describe weak ferromagnetism in α -FeO₃, MnCO₃ and CoCO₃ [78]. Soon after that, T. Moriya logically formulated it with respect to Anderson's superexchange theory [79, 80]. Therefore, this interaction is called Dzyaloshinskii-Moriya interaction. It is also sometimes called anisotropic exchange interaction, while Heisenberg interaction is isotropic interaction. Microscopic origin of the DM interaction is the spin-orbit coupling. Derivation of the DM interaction is given in the following.

As the starting point, let's think of the kinetic exchange due to the electron virtual hopping which coexists with the on-site spin-orbit interactions. As the minimal model, we consider two site model. Then, the Hamiltonian is

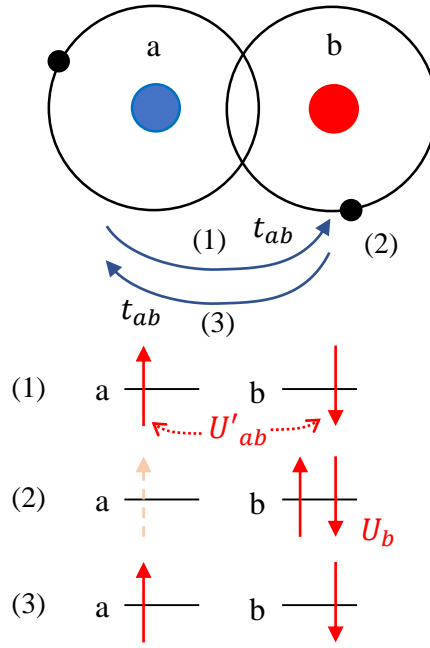


FIGURE 7.4: Schematic picture of the kinetic exchange. (1) Initial state where anti-parallel spins are lied in orbital a and b , respectively. (2) Excited state where one of the electron hopped from a to b . (3) Hopping back to the initial state alignment.

given by spin-orbit interactions and exchange interaction as

$$\hat{\mathcal{H}}' = \lambda \mathbf{L}_a \cdot \mathbf{S}_a + \lambda \mathbf{L}_b \cdot \mathbf{S}_b + V_{\text{ex}} \quad (7.66)$$

where first and second term are the relativistic spin-orbit interaction and the last term is the exchange interaction. The next step is to estimate the energy gains by means of the perturbation theory. In the first order perturbation, the energy gain is solely the exchange interaction which is given as $\langle 0 | \hat{\mathcal{H}}' | 0 \rangle = \langle V_{\text{ex}} \rangle$. In the explicit form, one may write the isotropic exchange interaction as

$$V_{\text{ex}} = \hat{\mathbf{J}} \mathbf{S}_a \cdot \mathbf{S}_b. \quad (7.67)$$

In the second order perturbation, intermediate states appear. By introducing ket vectors of the ground states $|g_a g_b\rangle$ and the excited states $|n_a n_b\rangle$, the energy gains are given by

$$\begin{aligned} \Delta E = & - \sum_{n_a} \frac{\langle g_a g_b | \lambda \mathbf{L}_a \cdot \mathbf{S}_a | n_a g_b \rangle \langle n_a g_b | V_{\text{ex}} | g_a g_b \rangle}{E_{n_a g_b} - E_{g_a g_b}} + [\text{permutation}] \\ & - \sum_{n_b} \frac{\langle g_a g_b | \lambda \mathbf{L}_b \cdot \mathbf{S}_b | g_a n_b \rangle \langle g_a n_b | V_{\text{ex}} | g_a g_b \rangle}{E_{g_a n_b} - E_{g_a g_b}} + [\text{permutation}], \end{aligned} \quad (7.68)$$

where permutation meaning the term $\lambda \mathbf{L} \cdot \mathbf{S}$ and V_{ex} are exchanged. The first term indicates the spin \mathbf{S}_1 is excited via the spin-orbit interaction. Then,

the excited state comes back to the ground state via the exchange interaction. Permutation indicates the spin S_1 is excited via the exchange interaction. Then, the excited state comes back to the ground state via the spin-orbit interaction. With the notation for the exchange interactions $\langle n_a g_b | \hat{J} | g_a g_b \rangle = J_{n_a g_b g_a g_b} = J_{g_a g_b n_a g_b}$, the Eq. 7.68 can be rewritten as

$$\Delta E = -2\lambda \left[\sum_{n_a} \left(\frac{J_{n_a g_b g_a g_b} \langle g_a | \mathbf{L}_a | n_a \rangle}{E_{n_a g_b} - E_{g_a g_b}} \right) [\mathbf{S}_a, (\mathbf{S}_a \cdot \mathbf{S}_b)] - \sum_{n_b} \left(\frac{J_{g_a n_b g_a g_b} \langle g_b | \mathbf{L}_b | n_b \rangle}{E_{g_a n_b} - E_{g_a g_b}} \right) [\mathbf{S}_b, (\mathbf{S}_b \cdot \mathbf{S}_a)] \right]. \quad (7.69)$$

By the commutation relation of the spin operators :

$$[\mathbf{S}_a, (\mathbf{S}_a \cdot \mathbf{S}_b)] = -i \mathbf{S}_a \times \mathbf{S}_b, \quad (7.70)$$

one can furthermore rewrite the Eq. 7.69 in a simple form as

$$-2\lambda i \left[\sum_{n_a} \left(\frac{J_{n_a g_b g_a g_b} \langle g_a | \mathbf{L}_a | n_a \rangle}{E_{n_a g_b} - E_{g_a g_b}} \right) + \sum_{n_b} \left(\frac{J_{g_a n_b g_a g_b} \langle g_b | \mathbf{L}_b | n_b \rangle}{E_{g_a n_b} - E_{g_a g_b}} \right) \right] [\mathbf{S}_a \times \mathbf{S}_b]. \quad (7.71)$$

This leads to the DM interaction 7.65 with the DM vector $\mathbf{D}_{ab} = \{D_{ab\mu}\}$ ($\mu = x, y, z$) given by

$$D_{ab\mu} = -2i\lambda \left(\sum_{n_a} \frac{J_{n_a g_b g_a g_b} \langle g_a | L_{a\mu} | n_a \rangle}{E_{n_a g_b} - E_{g_a g_b}} + \sum_{n_b} \frac{J_{g_a n_b g_a g_b} \langle g_b | L_{b\mu} | n_b \rangle}{E_{g_a n_b} - E_{g_a g_b}} \right). \quad (7.72)$$

The DM interaction is the first-order in the spin-orbit interaction. Usually, DM interaction is smaller than the isotropic Heisenberg interaction, however, this interaction is important as it induces important phenomena such as spin spiral states. Stable spin structure with the DM interaction is when the spins \mathbf{S}_a and \mathbf{S}_b are perpendicular to the DM vector \mathbf{D}_{ab} . Thus this interaction breaks isotropy of the spins. Furthermore, contrary to the isotropic Heisenberg interaction, perpendicular spin structure is stabilized by the DM interaction.

Another important aspect of the DM interaction is the symmetric property. Before going into detail of the symmetric property of the DM interaction, let this section to introduce the symmetric property of the spin under symmetric operations.

Crystals are periodic systems, thus they can be invariant under various symmetric operations. Spins act as axial vectors with respect to symmetry operations. Spin is an angular momentum, thus the time-reversal operation reverses the spin direction. If the spin is transferred by the mirror plane which contains the spin direction, then the spin is flipped due to the reverses of the ring current caused by the spin (Fig. 7.5 (a)). On the other hand, if the mirror plane is perpendicular to the spin direction, the ring current is

not reversed so as to the same spin direction (Fig. 7.5 (b)). This fact leads to conservation of the spin component perpendicular to the mirror plane, while the parallel component is flipped.

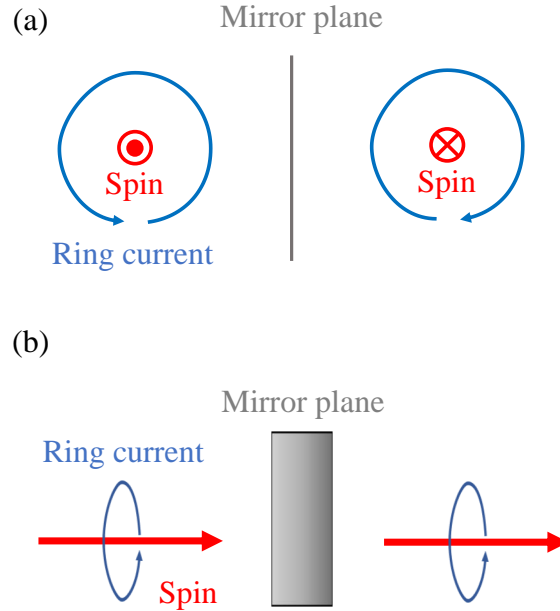


FIGURE 7.5: Schematic picture of the ring current model of the spin.

As is suggested, symmetric property of the DM interaction are important. Considering the symmetric property of the spin, one should have constraints on the DM interactions. Here the rest of this section discusses symmetric property of the DM interaction.

For the sake of simplicity, let's think of only two spins S_a and S_b . Assume these are aligned along x-axis where middle of these spins are located at the origin (Fig. 7.6 (a)).

Now introducing the chirality vector κ_{ab} defined as $\kappa_{ab} = S_a \times S_b$. DM interaction is then given as $D \cdot \kappa_{ab}$. If the inversion center is at the origin $x = 0$ (Fig. 7.6 (b)). Spins are invariant under the parity inversion operations. However, spins are exchanged as $S_a \rightarrow S_b$ and $S_b \rightarrow S_a$. Since the DM interaction should not be changed, this fact implies $D = 0$. This is one of the well known constraint of the DM interaction. There are other symmetric constraints as described in the following.

If the mirror plane is the yz-plane (Fig. 7.6 (c)), the spins are transferred as

$$S_a \rightarrow (S_{bx}, -S_{by}, -S_{bz}) \quad (7.73)$$

and the same relation concerning \mathbf{S}_b . These imply the change of the DM interaction as

$$\mathbf{D} \cdot \boldsymbol{\kappa}_{ab} \rightarrow \mathbf{D} \cdot (-\kappa_{abx}, \kappa_{aby}, \kappa_{abz}). \quad (7.74)$$

This leads to $D_x = 0$ meaning DM vector is in the yz-plane.

Another situation is when the mirror plane is the xy-plane (Fig. 7.6 (d)). With this mirror operation, the site a and b will not be changed, however the xy-components of the spins are reversed. Thus this mirror operation leads

$$\mathbf{S}_a \rightarrow (-S_{ax}, -S_{ay}, S_{az}) \quad (7.75)$$

and the same relation concerning \mathbf{S}_b . This gives

$$\mathbf{D} \cdot \boldsymbol{\kappa}_{ab} \rightarrow \mathbf{D} \cdot (-\kappa_{abx}, -\kappa_{aby}, \kappa_{abz}). \quad (7.76)$$

This leads $D_x = 0$ and $D_y = 0$ meaning the DM vector is perpendicular to the mirror plane.

Another important situation is when the rotation axes exist (Fig. 7.6 (e)). Assuming the x-axis is the n -fold rotational axis. With this rotation, spins are transferred

$$\mathbf{S}_a \rightarrow (S_{ax}, -S_{ay}, -S_{az}) \quad (7.77)$$

and the same relation concerning \mathbf{S}_b as usual. This leads $D_y = 0$ and $D_z = 0$ meaning the DM vector is x-axis direction.

The last situation is when the n -fold rotational axis is along y-axis (Fig. 7.6 (f)). Since the spin acts as an usual vector with respect to the rotational operations, $n = 2$ is the only possible situation in this case. In this case, the spins are transferred as

$$\mathbf{S}_a \rightarrow (-S_{bx}, S_{by}, -S_{bz}) \quad (7.78)$$

and the same relation concerning \mathbf{S}_b as usual. This leads $D_y = 0$ and $D_z = 0$ meaning the DM vector is again x-axis direction.

These are the well known symmetric constraints of the DM interactions derived by T. Moriya [79]. The most important point is that the symmetric operations allowed by the crystal structures do not change the DM interaction. The DM interaction is subjected to the crystallographic symmetries.

7.5 Superexchange theory in spin $\frac{1}{2}$ systems

Solving the Hubbard model is one of the challenging problem of the strongly correlated materials. The effective approach to this problem was invented by P. W. Anderson [80], and is called Superexchange theory. In reality, the magnetic ions are usually surrounded by some negative ions. His idea is that if the electron hopping is mediated by those negative ions, anti parallel spin can hop like that. Then, the energy gain can be estimated by the second-order

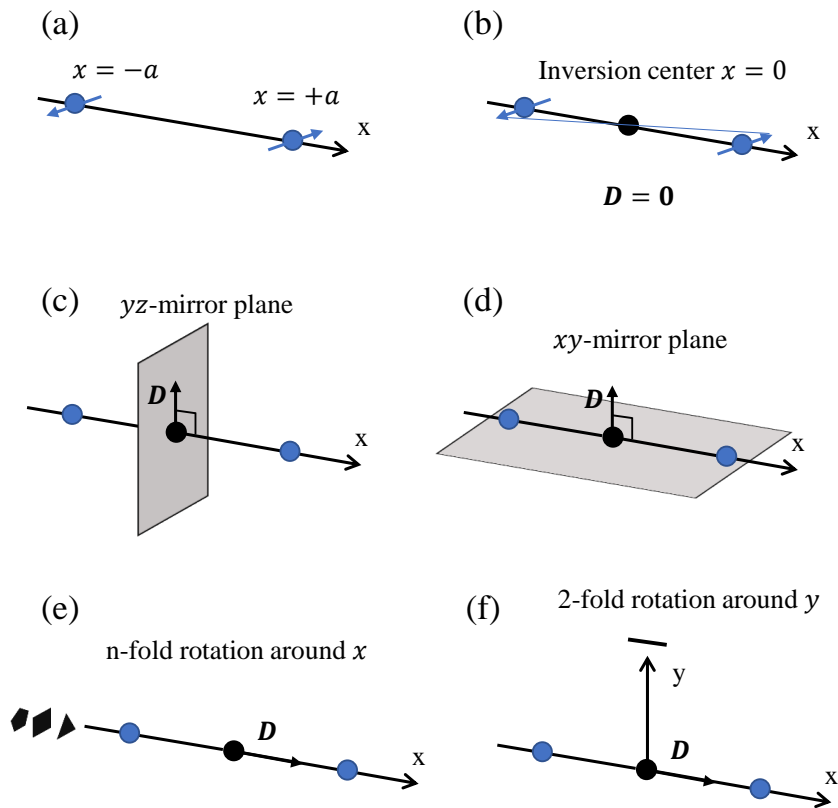


FIGURE 7.6: Symmetric property of the DM interaction in a simple two spin case. The blue spheres indicate magnetic sites aligned along x-axis. (a) Spin alignment, (b) With an inversion center exists at the bond center, (c) With a mirror plane in yz-plane, (d) With a mirror plane in xy-plane, (e) With a n-fold rotation around x-axis and (f) With a two-fold rotation around y-axis.

perturbation theory with respect to this virtual electron hopping. The energy gain can be mapped onto a general classical spin model which is given by

$$\hat{\mathcal{H}}_s = \sum_{\langle i,j \rangle} e_i \hat{A}_{ij} e_j \quad (7.79)$$

where \hat{A}_{ij} is the 3×3 tensor and e_i is a classical spin direction of the lowest Kramers doublet at site i . The tensor is expressed by 9-independent parameters as

$$\hat{\mathcal{H}}_s = \sum_{\langle i,j \rangle} (-J_{ij} e_i \cdot e_j + \mathbf{D}_{ij} \cdot (e_i \times e_j) + e_i \hat{\Gamma}_{ij} e_j), \quad (7.80)$$

for the magnetic sites i and j . Where the first term indicates isotropic Heisenberg interactions, the second term indicates DM interaction, the last term indicates traceless symmetric anisotropy, respectively. For the spin $\frac{1}{2}$ systems, one can introduce spin direction at site i as

$$e_i = \frac{\langle \alpha_i | \hat{\sigma} | \alpha_i \rangle}{|\langle \alpha_i | \hat{\sigma} | \alpha_i \rangle|} \quad (7.81)$$

with the lowest Kramers doublet α_i and vector of the Pauli matrices $\hat{\sigma}$.

In principle, the superexchange mechanism stands for the electron's hopping in the second order of the hopping parameters such as $i \rightarrow j \rightarrow i$. The electronic structure can be mapped onto the spin model 7.80 as follows.

In the second order perturbation theory, one can estimate the kinetic energy gain caused by the virtual hopping from site i to site j and vice versa as

$$\hat{t}_{ij} = - \langle G_{ij} | \hat{t}_{ij} \left(\sum_M \frac{\hat{P}_j |jM\rangle \langle jM| \hat{P}_j}{E_{jM}} \right) \hat{t}_{ji} + [\text{permutation}] | G_{ij} \rangle \quad (7.82)$$

where \hat{P}_j is the projector operator which enforces the Pauli principle, $\hat{t}_{ij} \equiv \{t_{ij}^{ab}\}$ is the off-site kinetic energy which does not depend on the spin indices, permutation indicates a term i and j are exchanged. $|G_{ij}\rangle$ is a Slater determinant in spin $\frac{1}{2}$ case, which is given by

$$G_{ij}(1,2) = \frac{1}{2} [\phi_i(1)\phi_j(2) - \phi_i(2)\phi_j(1)], \quad (7.83)$$

where ϕ_i and ϕ_j are the lowest Kramers doublet which are obtained after diagonalizing on-site one-electron Hamiltonian $\hat{\mathcal{H}}_{\text{CF}} + \hat{\mathcal{H}}_{\text{SOC}}$.

Intermediate state is given by the possible on-site Slater determinants. In spin $\frac{1}{2}$ case, one can have ${}_6C_2 = 15$ such Slater determinants for t_{2g} states. The intermediate states are obtained by diagonalizing the Coulomb interaction matrix. Therefore, the intermediate state $|jM\rangle$ and energy E_{jM} are taking into account correct atomic multiplet structures (M th Slater determinant of the excited two-electron configuration at site j). There is a problem of such

intermediate states, which is that if you have 15 such cases, these states contains physically meaningless states. Namely, if one of the intermediate state does not have the initial state of site j , it is a meaningless state. Therefore, we need \hat{P}_j which erase meaningless states. In other words, the projection chooses the states which contain ϕ_j at least. In practice, it projects $|jM\rangle$ onto a subspace of the Slater determinants as

$$\hat{P}_j |jM(1,2)\rangle = \frac{1}{\sqrt{2}}[\psi_j(1)\phi_j(2) - \psi_j(2)\phi_j(1)], \quad (7.84)$$

where ψ_j and ϕ_j are an unoccupied orbital and the occupied orbital, respectively. The unoccupied orbital can be reached from ϕ_i via the hopping \hat{t}_{ij} .

Then, with the existence of the spin-orbit interaction, tensor \hat{t}_{ij} is obtained by considering all maximum projection along $\pm x$, $\pm y$ and $\pm z$ of the linear combination of the Kramers states these are denoted as ϕ_i^1 and ϕ_i^2 here. Then, one can consider the linear combination of them as

$$\phi^{\pm\mu} = \alpha\phi_i^1 + \beta\phi_i^2. \quad (7.85)$$

The index μ is the direction of the pseudo spins as $\pm\mu = \pm x, \pm y, \pm z$. By finding coefficients α and β which maximize $\langle\phi^{\pm\mu}|\sigma|\phi^{\pm\mu}\rangle$, one can have $6 \times 6 = 36$ parameters of $\hat{t}_{\phi^{\pm\mu}\phi^{\pm\nu}}$. This 6 tensor is mapped onto the spin-model Eq. 7.80 by replacing spin vectors to unit unit spin vectors, one can have 9-independent parameters which are used in Eq. 7.80. This strategy has been applied in several papers [65–67, 73, 81–87].

7.6 Berry phase (Wannier) expression for the macroscopic electronic polarization

This section discusses a rigorous theory for the macroscopic electronic polarization in solid systems which is introduced by King-Smith and Vanderbilt [88]. Then, it is expanded in the Wannier basis by Resta [89, 90]. For the convenience of the physical meanings, here this section mainly describes expression in Wannier function.

This section starts from a controversy that the definition of the electronic polarization can not be applied to the crystal systems.

In a finite system such as molecules, the dipole moment d is defined as

$$d = \sum_i q_i \mathbf{r}_i, \quad (7.86)$$

where q_i is a charge at position \mathbf{r}_i . In the continuum states, the dipole moment is given by a integral of the number density $n(\mathbf{r})$ as

$$d = \int d\mathbf{r} \, e n(\mathbf{r}). \quad (7.87)$$

This quantity may be defined within the unit cell volume in crystal systems. It should be normalized by the unit cell volume.

Then, a problem arises from the arbitrariness of how one chooses the unit cell. In the Fig. 7.7, a positive charge and a negative charge is aligned periodically. As one can see from the picture, there are infinite choice of the unit cell definition. Nevertheless, the electronic polarization (dipole per an unit cell) has a different value which depends on the choice of the unit cell.

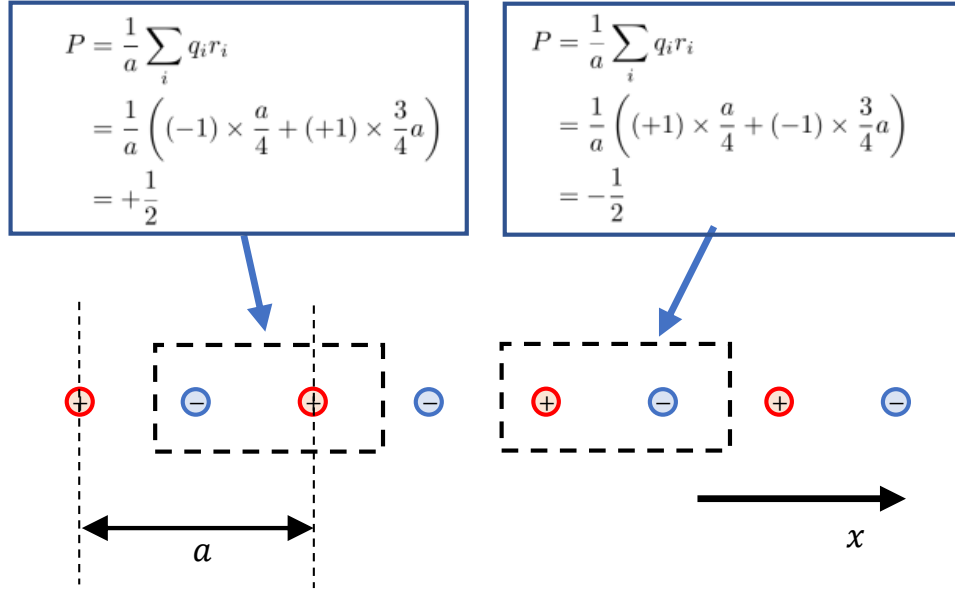


FIGURE 7.7: Arbitrariness of the electronic polarization in solid systems.

Another thing which we have to realize is that what is measured in a measurement. According to King-Smith, Vanderbilt and Resta, only measurable well-defined electronic polarization is a change of it. Thus, the absolute value of it does not matter.

In one-dimensional case, one can have the absolute electronic polarization as the sum of the point charges on the ions and centers of each occupied Wannier function as

$$p = \frac{1}{a} \left(\sum_i (q_i x_i)^{\text{ions}} + \sum_n^{\text{occ}} (q_n \bar{r}_n)^{\text{WFs}} \right), \quad (7.88)$$

where a is a length of the unit 1D-cell, the first term is the point charges on the ions and the second term is the electronic charge at the Wannier centers \bar{r}_n of the occupied orbital which is given by Eq. 7.16. The second term indicates a shift of point charges induced by an external electric field [91].

Consequently, since the measured electronic polarization is a change of it, well defined electronic polarization in general solids is given by

$$P = \frac{e}{V} \sum_n^{\text{occ}} \bar{\mathbf{r}}_n = \frac{e}{V} \sum_n^{\text{occ}} \langle w_n | \mathbf{r} | w_n \rangle, \quad (7.89)$$

where V and w_n are the volume of the unit cell and n th occupied band Wannier function, respectively [89, 90, 92]. Since the position operator is defined relative to the origin of the crystal, the sum should not be affected by the definition.

7.7 Superexchange theory for the magnetoelectric effect

Microscopic understanding of the non-linear ME effects are still non-trivial task. It should be done in a systematic way, however, the theories suggested so far are mainly phenomenological theories which are sometimes efficient and sometimes not. The most rigorous theory of the electronic polarization is the Berry phase (Wannier) expression of the electronic polarization which has already been described in Sec. 7.6. However, what we wish to know is the origin (or mechanism) of the electronic polarization. Therefore, this section shows how the spin-model of the electronic polarization is logically derived from rigorous Berry phase expression of the electronic polarization.

At the beginning, assume the atomic-like Wannier functions are well localized. Thus, there is no overlap between Wannier functions (Fig. 7.8 (a)). Now, think of the physical meaning of the Berry phase expression of the electronic polarization. The Berry phase expression of the electronic polarization is the shifts of the Wannier function centers relative to the ion centers and those are given by the Wannier densities (e.g. if one has ferromagnetic alignment, the Wannier density is symmetric and thus there is no electronic polarization. However, if one flips the spin at the one of the neighboring sites, the electronic polarization should be finite as the hopping amplitude will be differed Fig. 7.8 (b) and (c)). Therefore, one can logically estimate those shifts as the first-order of the hopping so that the desired Wannier functions to have a form

$$|w_i\rangle \approx |\alpha_i\rangle + |\alpha_{i \rightarrow j}\rangle. \quad (7.90)$$

The first term is the atomic-limit Wannier function at site i and the second term is a tail of the desired Wannier function spreading to the neighboring site j . Practically, such tails can be obtained by the first-order of the hopping by considering the virtual hopping to the unoccupied states at the site j and vice versa. This is exactly the SE theory, therefore, one can estimate those

tails as

$$|\alpha_{i \rightarrow j}\rangle = \sum_M \frac{\hat{P}_j |jM\rangle \langle jM| \hat{P}_j}{E_{jM}} \hat{t}_{ji} |\alpha_i\rangle. \quad (7.91)$$

Then, substituting Eq. 7.90 to Eq. 7.89 allows one to write the electronic polarization as a pair-wise form as

$$\mathbf{P} = \sum_{\langle i,j \rangle} \mathbf{P}_{ij}, \quad (7.92)$$

where

$$\mathbf{P}_{ij} = \frac{e}{V} \boldsymbol{\tau}_{ji} (\langle \alpha_{j \rightarrow i} | \alpha_{j \rightarrow i} \rangle - \langle \alpha_{i \rightarrow j} | \alpha_{i \rightarrow j} \rangle), \quad (7.93)$$

where $\boldsymbol{\tau}_{ji} = \mathbf{R}_j - \mathbf{R}_i$ is a vector connecting neighboring sites.

$\langle \alpha_{i \rightarrow j} | \alpha_{i \rightarrow j} \rangle$ is given by

$$\langle \alpha_{i \rightarrow j} | \alpha_{i \rightarrow j} \rangle = \langle \alpha_i | \hat{t}_{ij} \left(\sum_M \frac{\hat{P}_j |jM\rangle \langle jM| \hat{P}_j}{E_{jM}} \right)^2 \hat{t}_{ji} | \alpha_i \rangle. \quad (7.94)$$

Therefore, one can map onto the spin model with the same analogy to the magnetic energy. Then, we have

$$\mathbf{P} = \sum_{\langle i,j \rangle} \epsilon_{ji} (\mathcal{P}_{ij} \mathbf{e}_i \cdot \mathbf{e}_j + \mathcal{P}_{ij} [\mathbf{e}_i \times \mathbf{e}_j] + \mathbf{e}_i \Pi_{ij} \mathbf{e}_j), \quad (7.95)$$

where $\epsilon_{ji} = \boldsymbol{\tau}_{ji} / |\boldsymbol{\tau}_{ji}|$ the first term is the isotropic interaction, the second term is the antisymmetric interaction and the last term is the traceless symmetric anisotropy, respectively. This is exactly the analogue of the spin model for the magnetic energy, but with the directional information of the bonds ϵ_{ji} .

7.8 Spin-current Mechanism

The inverse DM mechanism Eq. 6.7 and the second term of Eq. 7.95 are sometimes referred as the spin-current mechanism. Let's think of the motions of the spins. This can be understood from the Heisenberg equation of motion with respect to Heisenberg spin Hamiltonian $\hat{\mathcal{H}}_{\text{Heis}}$ (Eq. 7.50) and spin as

$$\frac{dS_i^\mu}{dt} = \frac{i}{\hbar} [\hat{\mathcal{H}}_{\text{Heis}}, S_i^\mu] = -2 \sum_{\mu, \alpha, \beta} \sum_{\langle i,j \rangle}^{\text{x,y,z}} \epsilon_{\mu\alpha\beta} J_{ij} S_i^\alpha S_j^\beta, \quad (7.96)$$

where $\epsilon_{\mu\alpha\beta}$ is the antisymmetric Levi-Civita tensor. Continuity equation gives

$$\frac{dS_i^\mu}{dt} + \sum_j J_{ij}^{S^\mu} = 0, \quad (7.97)$$

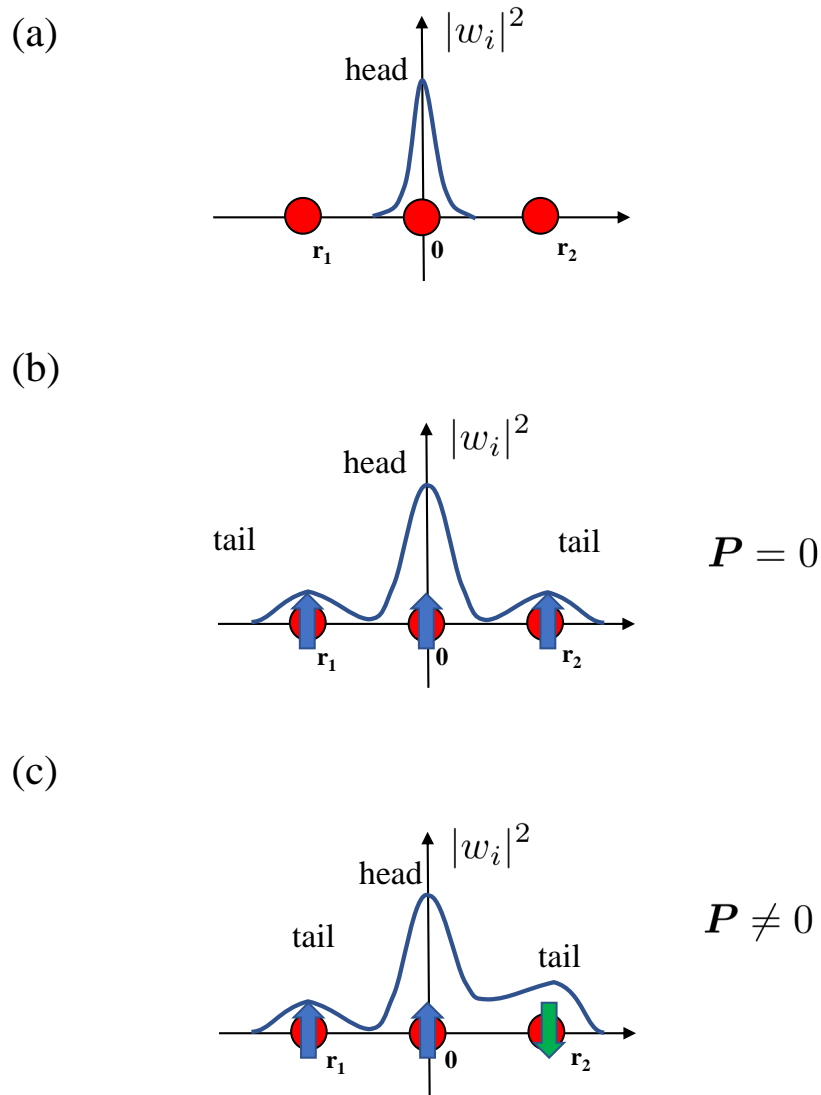


FIGURE 7.8: Wannier density of (a) Only atomic limit (head), (b) After inclusion of tails and (c) After one spin is flipped. Red spheres indicate magnetic site at the origin and neighbors (r_1 and r_2).

therefore, the spin-current j_{ij}^s is given as

$$j_{ij}^s \propto \mathbf{S}_i \times \mathbf{S}_j. \quad (7.98)$$

As a result, noncollinear spin alignments coupled with exchange interactions lead to the spin-current [55, 93]. Fig. 7.9 shows the relation between the spin-current j_{ij}^s and predicted direction of the electronic polarization by the inverse DM mechanism Eq. 6.7.

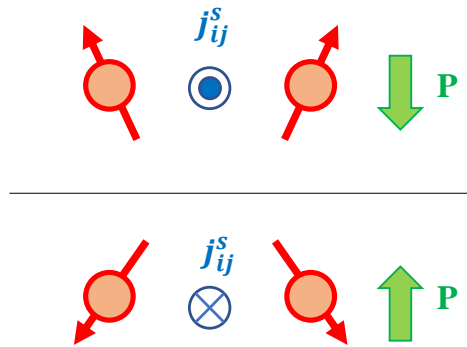


FIGURE 7.9: Schematic picture of the spin-current generated from the noncollinear spin pairs. The green arrows indicate the direction of the electronic polarization predicted by the inverse DM mechanism.

Chapter 8

Magnetoelectric effect of a spiral magnet $\text{Ba}_2\text{CuGe}_2\text{O}_7$

8.1 Multiferroic $\text{Ba}_2\text{CuGe}_2\text{O}_7$

One of the interesting examples of the multiferroic material is $\text{Ba}_2\text{XGe}_2\text{O}_7$ ($\text{X}=\text{Mn}, \text{Cu}, \text{Co}$). In those materials, magnetically induced non-linear ME effect has been observed [94–97]. As we saw in Chap. 6, there are three suggested mechanisms so far which can give electronic polarization induced by the magnetic orders. $\text{Ba}_2\text{XGe}_2\text{O}_7$ has a spin spiral order in the ground state, therefore, this is a typical case where the inverse DM mechanism should predict the correct ME effect. However, as explained in the Chap. 6, suggested mechanisms are still controversial. Actually, the mechanism of the non-linear ME effect in those materials have been described by means of the d-p hybridization mechanism by Murakawa et. al. [97]. However, it should be noted the d-p hybridization mechanism is an analogue of the single ion anisotropy in magnetic energies, and it does not exist in spin $\frac{1}{2}$ system such as $\text{Ba}_2\text{CuGe}_2\text{O}_7$. Thus it makes a conjecture that the d-p hybridization mechanism probably does not exist in the spin $\frac{1}{2}$ system. Indeed, as a consequence of the Kramers degenerate, such single ion contribution in the electronic polarization cannot exist in spin $\frac{1}{2}$ systems. This will be justified in Sec. 8.4. Theoretical understanding of the ME effect in $\text{Ba}_2\text{CuGe}_2\text{O}_7$ is, hence, quite controversial. Therefore, this chapter discusses the ME effect in spin $\frac{1}{2}$ $\text{Ba}_2\text{CuGe}_2\text{O}_7$.

$\text{Ba}_2\text{CuGe}_2\text{O}_7$ crystallizes in non-polar $P\bar{4}2_1m$ (No. 113) space group [98–100]. Crystal structure of $\text{Ba}_2\text{CuGe}_2\text{O}_7$ is shown in Fig. 8.1. As seen from Fig. 8.1 (a), the crystal structure is forming quasi two-dimensional plane which lies in xy -plane. The $P\bar{4}2_1m$ space group contains 8 symmetry elements. This can be obtained by a combination of \hat{S}_4^z and $\hat{C}_2^x + (\frac{1}{2}, \frac{1}{2}, 0)$. These are 4-fold rotoinversion around z -axis and 2-fold rotation around x -axis followed by the shift in the unit of the lattice parameter a , respectively. These symmetries imply some constraint on the DM vector which will be discussed later.

$\text{Ba}_2\text{CuGe}_2\text{O}_7$ exhibit a spin spiral state in the ground state. Besides the multiferroicity, this material has interesting magnetic properties. The spin spiral state is caused by the competition between isotropic Heisenberg interaction and anisotropic Dzyaloshinskii-Moriya interaction with the spin spiral

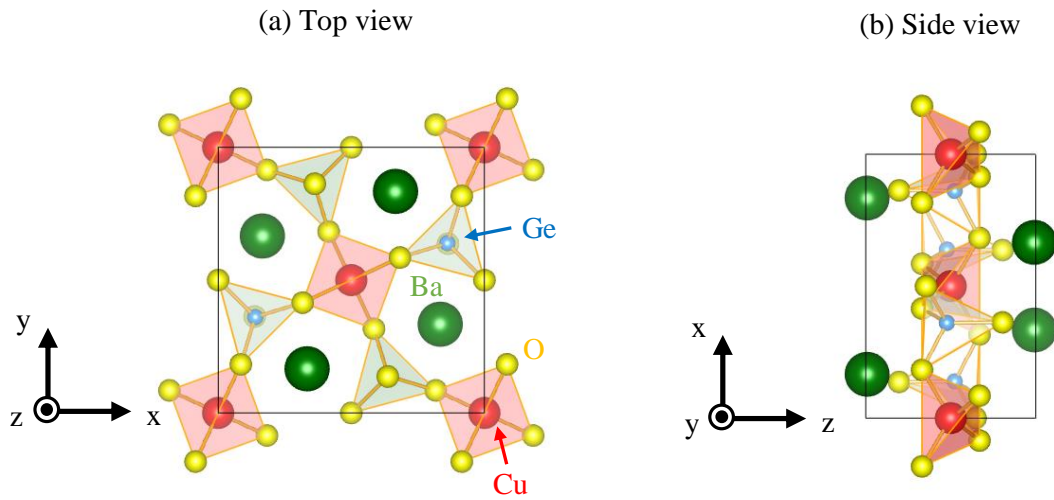


FIGURE 8.1: Crystal structure of $Ba_2CuGe_2O_7$. Red, green, blue and yellow spheres indicate Cu, Ba, Ge and Oxygen atoms, respectively. (a) Top view and (b) Side view.

propagation vector $(1 + \zeta, \zeta, 0)$ ($\zeta = 0.027$) [101]. Another interesting observation is that when an external magnetic field is applied in the plane of spin rotation. Upon such external magnetic field, the ground state incommensurate spin structure transit to the commensurate C-type antiferromagnet [102, 103]. Indeed, such transition is due to the out-of-plane component of the DM vectors. From a symmetry constraint, out-of-plane component of the DM vector should be opposite direction (Fig. 8.2). Due to this fact, the C-type AFM is stabilized by the external magnetic field along c-axis (Fig. 8.3).

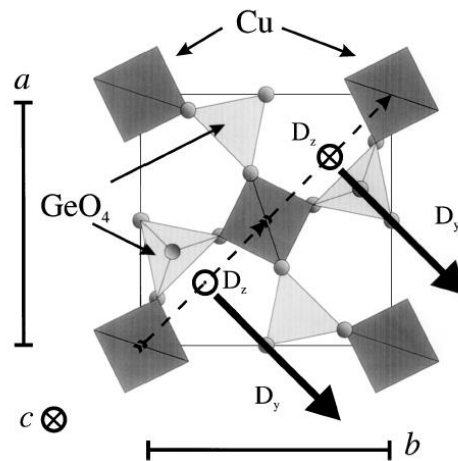


FIGURE 8.2: Direction of the in-plane and out-of plane DM interactions. The picture is taken from [103].

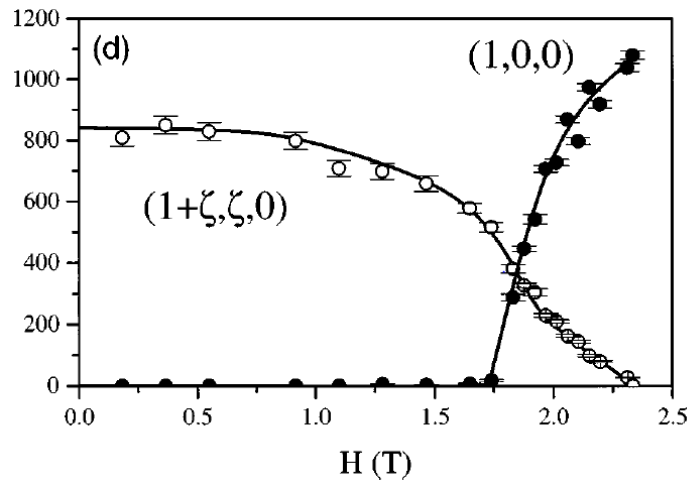


FIGURE 8.3: Observed IC-C (incommensurate-commensurate) transition of $Ba_2CuGe_2O_7$ upon the external magnetic field along c -axis. These show incommensurate phase $(1 + \zeta, \zeta, 0)$ and commensurate Néel $(1, 0, 0)$ peak. The picture is taken from [103].

Furthermore, $Ba_2CuGe_2O_7$ shows a complicated magnetic phase diagram regarding other direction of the magnetic fields (Fig. 8.4) [104].

$Ba_2CuGe_2O_7$ also shows quite interesting non-linear ME effect. By the \hat{S}_4^z symmetry element alone, this material is forbidden to have spontaneous electronic polarization. However, electronic polarization is observed. Thus, it is magnetically induced electronic polarization. Remarkable character is observed by Murakawa et al. [96]. Their experiment revealed that by inducing the magnetic field along some direction (parallel to the quasi two dimensional plane), one can flip the direction of the electronic polarization as $\mathbf{P} \parallel [001] \rightarrow [00\bar{1}]$ (see Fig. 8.5).

This chapter investigates the controversial ME-effect in $Ba_2CuGe_2O_7$ by means of a microscopical point of view.

8.2 Symmetric property of $Ba_2CuGe_2O_7$

As it is described in a very simple model in Sec. 7.4.2, spin is an axial vector, thereby, tensor of the spin model should be subjected to symmetric properties of crystals. This section describes symmetric properties enforced on the spin model of $Ba_2CuGe_2O_7$.

As explained in Sec. 8.1, $Ba_2CuGe_2O_7$ crystallizes in $P\bar{4}2_1m$ (No. 113) space group and it consists of \hat{S}_4^z and $\hat{C}_2^x + (\frac{1}{2}, \frac{1}{2}, 0)$ symmetry elements. Therefore, DM vectors between the nearest-neighbor of this model have a symmetric constraint as

$$\mathbf{D}_{0j} = (-1)^j d^{xy} [\boldsymbol{\epsilon}_{j0} \times \mathbf{n}^z] + d^z \iota_{j0} \mathbf{n}^z, \quad (8.1)$$

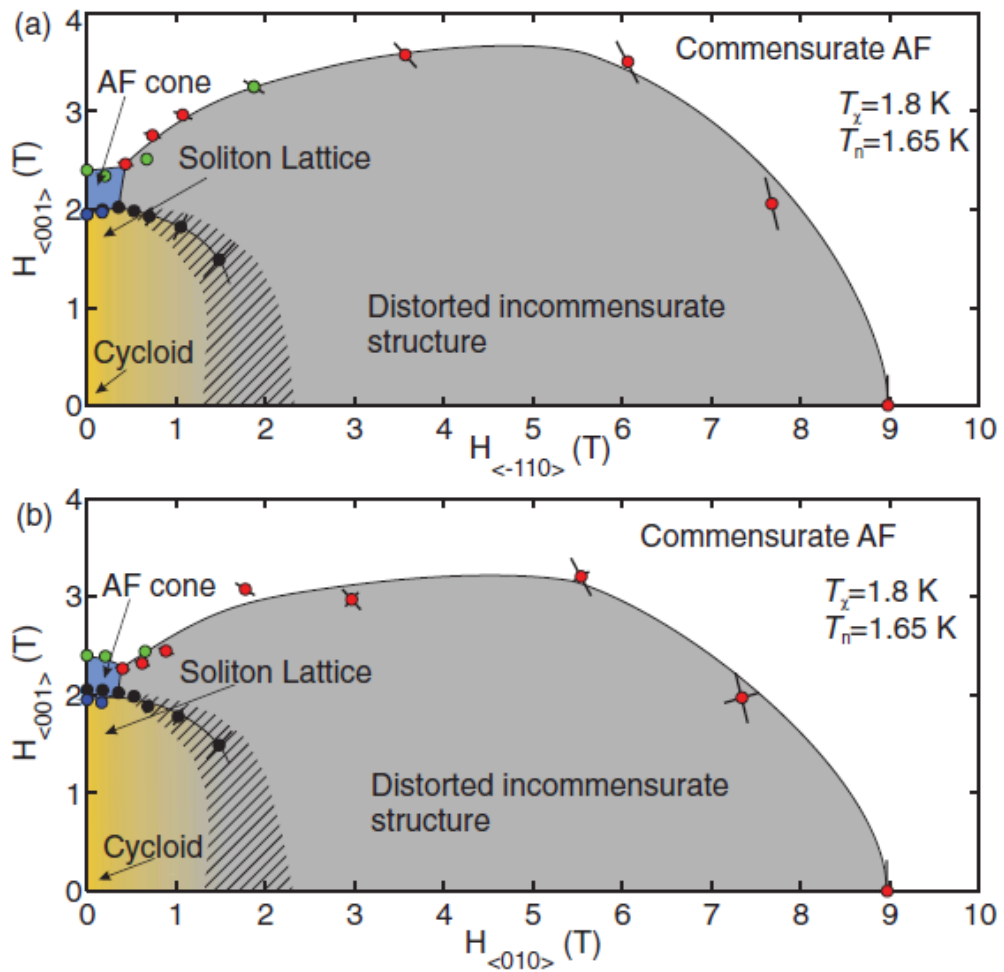


FIGURE 8.4: Magnetic phase diagram of $Ba_2CuGe_2O_7$ regarding two direction of the external magnetic fields. (a) $[001]$ and $[110]$. (b) $[001]$ and $[010]$. The figure is taken from [104].

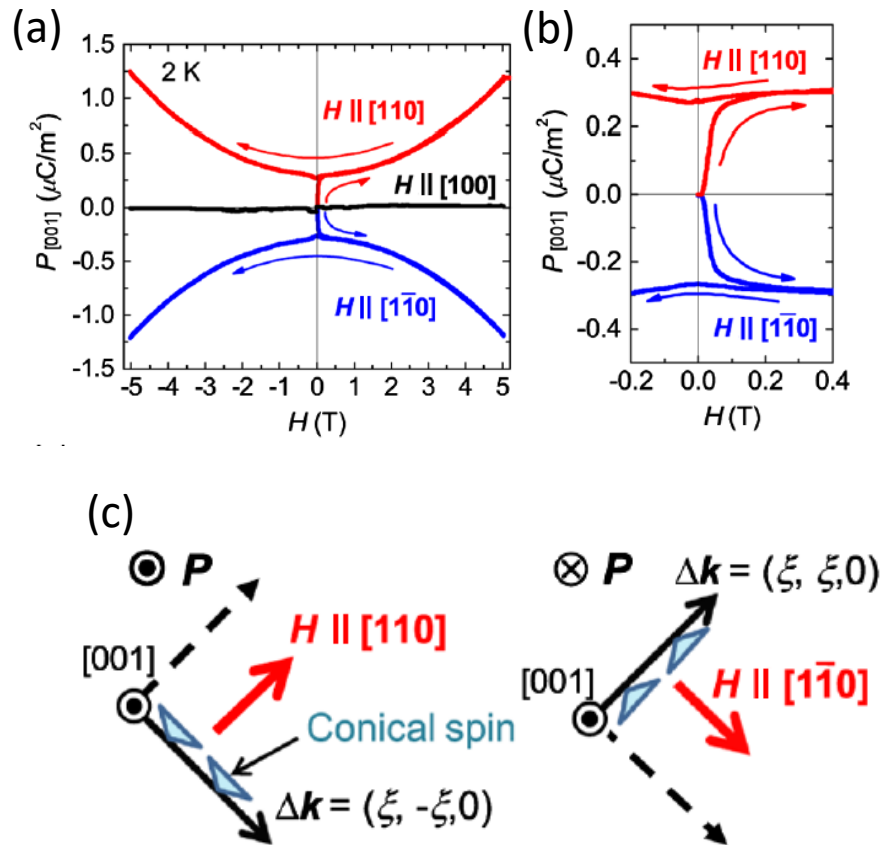


FIGURE 8.5: Flipping of the out-of-plane electronic polarization by the external magnetic fields. (a) Observed hysteresis of the electronic polarization. (b) Closed view around the critical region. (c) Schematic picture of the flipping of the electronic polarization and spin structure. The figures are adopted from [96].

where 0 index indicates the Cu ion at the center of the unit cell while $j = -8, \dots, +8$ is the nearest-neighbors of it (see Fig. 8.6 (a) for the notations) [105]. \mathbf{n}^z is a unit vector perpendicular to the quasi-two-dimensional plane. t_{j0} is an antisymmetric scalar of the ion index which is defined as

$$t_{ij} = \frac{i-j}{|i-j|} \quad (8.2)$$

which satisfies the condition $|t_{ij}| = 1$ and $t_{ij} = -t_{ji}$. \hat{S}_4^z is responsible for the $[\epsilon_{j0} \times \mathbf{n}^z]$ and a prefactor $(-1)^j$, where the former indicates 4-fold rotation symmetry while the latter indicates rotoinversion symmetry [105] (see Fig. 8.6 (b)).

About the spin model of the electronic polarization which is introduced in Sec. 7.7, it has similar properties, however, an additional prefactor compared to the magnetic energy, the unit vector along the bonds $\epsilon_{ji} = \tau_{ji}/|\tau_{ji}|$ leads different behavior.

Let's think of the nearest-neighbor sites. The isotropic (the first term of Eq. 7.95) P_{ij} should vanish because of the symmetry constraint of this material. There are some other contribution from next nearest-neighboring sites ($\pm a/2, \pm a/2, \pm c$) which are located at the different plane. Those are given as

$$P_{0j} = (-1)^j t_{j0} p_{\perp}^0 \quad (8.3)$$

where p_{\perp}^0 is the parameter of the isotropic Heisenberg-like interaction of Eq. 7.95, but between out-of-plane bonds which is denoted as \perp (see Fig. 8.6 (d) for the notations).

The antisymmetric part of the electronic polarization \mathcal{P}_{ij} has finite value between the nearest neighboring sites and which is given by

$$\mathcal{P}_{0j} = (-1)^j p_{\parallel}^{xy} t_{j0} \epsilon_{j0}, \quad (8.4)$$

where p_{\parallel}^{xy} is the parameter of such antisymmetric interactions and ϵ_{ji} is a unit vector which has already been defined in Sec. 7.7 (see Fig. 8.6 (c)). Furthermore, we will have some contribution from the next-nearest neighboring sites as

$$\mathcal{P}_{0j} \approx p_{\perp}^{xy} t_{j0} [\epsilon_{j0} \times \mathbf{n}^z] + (-1)^j p_{\perp}^z \mathbf{n}^z, \quad (8.5)$$

where the approximate \approx meaning the neglect of the small difference between x - and y -components (see Fig. 8.6 (d)).

This section concludes that these parameters for equivalent sites (e.g. four nearest-neighbors) can be characterized with a small set of independent parameters, but should obey the symmetric properties of $\text{Ba}_2\text{CuGe}_2\text{O}_7$.

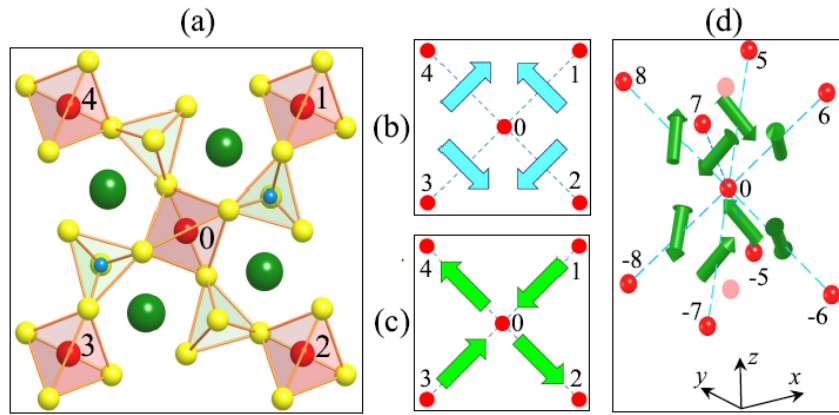


FIGURE 8.6: Symmetric property of the $\text{Ba}_2\text{CuGe}_2\text{O}_7$. (a) Numbering of the nearest-neighboring sites. (b) Direction of the in-plane DM vector of $\text{Ba}_2\text{CuGe}_2\text{O}_7$ between nearest-neighbors (Cu-Cu). (c) Direction of the vector of the antisymmetric part of the in-plane electronic polarization \mathcal{P} . (d) Direction of \mathcal{P} between out-of-plane next-nearest neighbors with the sites numbering.

8.3 Electronic structure

As the preliminary step, plane-wave basis DFT electronic structure calculations [106] have been performed for the $\text{Ba}_2\text{CuGe}_2\text{O}_7$. An experimental crystal structure ($P4_21m$ (No. 113) space group) and lattice parameter $a = 8.466 \text{ \AA}$ and $c = 5.445 \text{ \AA}$ are used in all calculations [99]. The relativistic spin-orbit coupling (SOC) is taken into account in all the following calculations.

Fig. 8.7 shows the electronic structure calculated by Quantum Espresso code [107] with the ultra-soft pseudo potential [108, 109]. In the DFT calculation, $10 \times 10 \times 10$ k -point mesh and Perdew-Burke-Ernzerhof (PBE) exchange correlation potential [110–112] are used. Fig. 8.7 also shows density of states (DOS) projected onto atomic wave function of Cu-3d along the electronic band structure. The projected DOS (PDOS) shows the states around the Fermi level are clearly dominated by Cu-3d states and thus, these states can be used in the magnetic model.

Next step is to construct the tight-binding model (Wannier function) which will be used to construct low-energy Hubbard model (Eq. 7.1). Cu-3d states and thus, the usual procedure of the Wannier function can be adopted easily. The most well established procedure of constructions of Wannier functions is the maximally localized Wannier function method (MLWF) which has already been described in Sec. 7.2. To construct Wannier functions by the MLWF procedure wannier90 code is used [70, 113, 114]. As one can see from the electronic structure of Fig. 8.7, one can have whole 3d 5-orbital model. Therefore, the 5-orbital model is used in the following.

However, one can encounter a numerical problem, namely, the MLWF

procedure can give physically meaningless Wannier functions as it is explained in Sec. 7.2. Indeed, such problem has been encountered in this case. The problem can be seen from the Wannier centers which is shown in the first column of Tab. 8.1. As it is seen from the table, the Wannier functions constructed from MLWF method are not obeying symmetric property of the material, therefore, Hamiltonian of this Wannier functions should be meaningless.

TABLE 8.1: Wannier function centers of Cu $3d$ orbital constructed by MLWF, SLWF and modified MLWF. Corresponding Cu sites are located at (0.00000, 0.00000, 2.72250) for the first 10-orbital and (4.23300, 4.23300, 2.72250) for the rest. $\lambda = 10^7$ is used as the Lagrange multiplier in SLWF.

Index	MLWF	SLWF	modified MLWF
1	(-0.006315, -0.027387, 2.550192)	(0.000000, 0.000000, 2.722500)	(0.000000, 0.000000, 2.722500)
2	(-0.001291, -0.348851, 2.717052)	(0.000000, 0.000000, 2.722500)	(-0.000000, -0.000000, 2.728547)
3	(-0.308735, 0.156248, 2.712695)	(0.000000, 0.000000, 2.722499)	(-0.000000, 0.000000, 2.716452)
4	(-0.001740, 0.095520, 2.879435)	(0.000000, 0.000000, 2.722500)	(-0.000000, -0.000000, 2.722500)
5	(0.318229, 0.124647, 2.753190)	(-0.000000, -0.000000, 2.722500)	(0.000000, -0.000000, 2.722500)
6	(-0.004957, -0.036423, 2.530031)	(0.000000, 0.000000, 2.722500)	(-0.000000, -0.000000, 2.722500)
7	(0.020153, -0.347561, 2.714671)	(-0.000000, 0.000000, 2.722500)	(-0.000000, 0.000000, 2.728547)
8	(-0.312473, 0.149647, 2.711788)	(0.000000, -0.000000, 2.722499)	(0.000000, 0.000000, 2.716452)
9	(-0.007079, 0.075499, 2.904120)	(0.000000, 0.000000, 2.722499)	(-0.000000, -0.000000, 2.722500)
10	(0.304736, 0.158933, 2.751786)	(-0.000000, 0.000000, 2.722500)	(0.000000, 0.000000, 2.722500)
11	(4.235473, 4.212861, 2.753223)	(4.232999, 4.232999, 2.722500)	(4.233000, 4.233000, 2.722500)
12	(4.063818, 4.535646, 2.712022)	(4.232999, 4.232999, 2.722499)	(4.233000, 4.233000, 2.716452)
13	(4.580456, 4.259862, 2.719744)	(4.232999, 4.232999, 2.722500)	(4.233000, 4.233000, 2.728547)
14	(4.118174, 4.257500, 2.682343)	(4.232999, 4.232999, 2.722499)	(4.233000, 4.233000, 2.722500)
15	(4.166723, 3.898971, 2.745528)	(4.232999, 4.232999, 2.722500)	(4.233000, 4.233000, 2.722500)
16	(4.232983, 4.253596, 2.840994)	(4.232999, 4.232999, 2.722500)	(4.233000, 4.233000, 2.722500)
17	(4.219105, 4.581820, 2.726701)	(4.232999, 4.232999, 2.722499)	(4.233000, 4.233000, 2.716452)
18	(3.926197, 4.072980, 2.731743)	(4.232999, 4.232999, 2.722500)	(4.233000, 4.233000, 2.728547)
19	(4.227884, 4.120724, 2.620337)	(4.232999, 4.232999, 2.722499)	(4.233000, 4.233000, 2.722500)
20	(4.559433, 4.135747, 2.692391)	(4.232999, 4.232999, 2.722500)	(4.233000, 4.233000, 2.722500)

The other possibility is selectively Localized Wannier function (SLWF) method and modified MLWF. These obtain qualitatively good Wannier functions (see the second and third column of Tab. 8.1). As seen from Tab. 8.1, modified MLWF method gave slightly shifted Wannier functions, however, these centers are reflecting the symmetric property of $Ba_2CuGe_2O_7$. Hence, the modified MLWF will be used in the all of the later analysis of the 5-orbital model.

The tight-binding band structures of the 5-orbital models constructed modified MLWF are plotted is cyan solid lines in Fig. 8.7. Those are showing nice agreement with the DFT band structure.

8.4 Nonexistence of single ion contributions in spin 1/2 system

One of the problem of the existing analyses of the $Ba_2CuGe_2O_7$ is that many people believe the d-p hybridization model can describe the non-linear ME effect of the spin $\frac{1}{2}$ system such as Cu^{+2} based oxides.

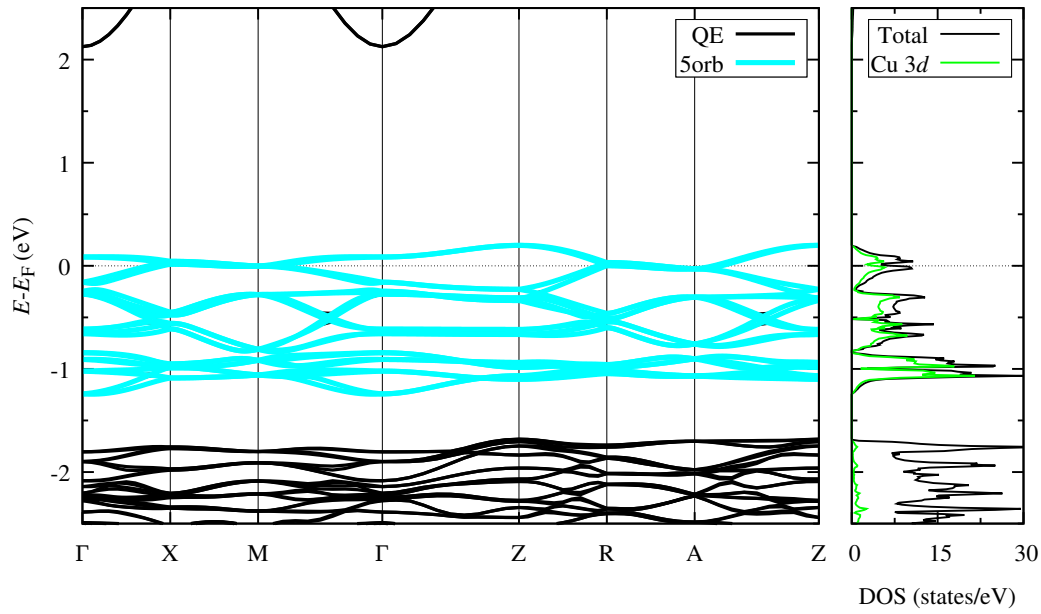


FIGURE 8.7: Band structure and DOS of $\text{Ba}_2\text{CuGe}_2\text{O}_7$. Cyan lines indicate the band structure obtained from tight-binding model constructed from modified MLWF.

The d-p hybridization mechanism is an analogue of the single ion anisotropy in the magnetic energy. The single ion anisotropy for the spin $\frac{1}{2}$ does not exist because of the Kramers states. This can be understood easily from the fact that the matrix elements of the orbital angular momentum operator for the Kramers states $|+\rangle$ and $|-\rangle$ quench [115]. This is formally allowed by the requirement for the Kramers states $\langle +|\mathcal{H}_{\text{soc}}|-\rangle = \langle -|\mathcal{H}_{\text{soc}}|+\rangle = 0$. Since the single ion anisotropy arises from the second order, it is zero. This fact leads to a conjecture that the single ion contribution to the electronic polarization does not probably exist either.

As explained in Sec. 8.1, non-linear ME effect in $\text{Ba}_2\text{CuGe}_2\text{O}_7$ is investigated by means of the d-p hybridization mechanism which only contains the spin of the individual ions [97]. This means it is the single ion contribution. The rest of this section proves the non-existence of the single ion contribution in spin $\frac{1}{2}$ systems.

Starting from the general Berry-phase expression for the macroscopic electronic polarization which is given by Eq. 7.89. This expression can be further rewritten as

$$\mathbf{P} = -\frac{e}{V}\text{Tr}\{\hat{\mathbf{r}}\hat{\mathbf{D}}\}, \quad (8.6)$$

where $\hat{\mathbf{r}}$ and $\hat{\mathbf{D}}$ are the position matrix and the density matrix for the hole state $|\alpha\rangle$ in the basis of the Kramers states [116]. This is identical to the change caused by the d-p hybridization mechanism. The hole state $|\alpha\rangle$ is given by a

linear combination of the Kramers states e. g.

$$|\alpha\rangle = a|+\rangle + b|-\rangle \quad (8.7)$$

with coefficients a and b . Now the density matrix of the hole state is given by

$$\hat{D} = |\alpha\rangle\langle\alpha| \quad (8.8)$$

$$= (a|+\rangle + b|-\rangle)(a^*\langle+| + b^*\langle-|) \quad (8.9)$$

$$= \begin{pmatrix} |a|^2 & ab^* \\ a^*b & |b|^2 \end{pmatrix}. \quad (8.10)$$

The spin is rotated by SU(2) rotation matrices and the direction is given by Eq. 7.81. This rotation changes the coefficients a and b , however, trace of the density matrix gives $|a|^2 + |b|^2$ and is a constant. Remaining term is the position operator. Kramers states are related to each other via the time reversal operation as $\hat{T}|+\rangle = -|-\rangle$ and $\hat{T}|-\rangle = |+\rangle$ where the time-reversal operator is given by $\hat{T} = -i\hat{\sigma}_y\hat{K}$ with the conjugate operator \hat{K} . For any spin-less operator r , the Kramers states have following relations

$$\langle+|\mathbf{r}|+\rangle = \langle-|\mathbf{r}|-\rangle \quad (8.11)$$

and

$$\langle+|\mathbf{r}|-\rangle = \langle-|\mathbf{r}|+\rangle = 0. \quad (8.12)$$

The relation of the off-diagonal elements Eq. 8.12 can be realized from the fact that a Kramers doublet with the explicit spins (\uparrow, \downarrow) has following general forms

$$|+\rangle = |+\uparrow\rangle + |+\downarrow\rangle \quad (8.13)$$

$$= \cos\frac{\theta}{2}|\uparrow\rangle + \sin\frac{\theta}{2}e^{i\phi}|\downarrow\rangle \quad (8.14)$$

$$= \begin{pmatrix} \cos\frac{\theta}{2} \\ \sin\frac{\theta}{2}e^{i\phi} \end{pmatrix} \quad (8.15)$$

and

$$|-\rangle = |-\uparrow\rangle + |-\downarrow\rangle \quad (8.16)$$

$$= -\sin\frac{\theta}{2}e^{-i\phi}|\uparrow\rangle + \cos\frac{\theta}{2}|\downarrow\rangle \quad (8.17)$$

$$= \begin{pmatrix} \sin\frac{\theta}{2}e^{-i\phi} \\ \cos\frac{\theta}{2} \end{pmatrix} \quad (8.18)$$

for any spin direction θ and ϕ . The relation of the Kramers doublet $\hat{T} |+\rangle = -|-\rangle$ leads to the relations

$$|-\downarrow\rangle = \hat{K} |+\uparrow\rangle \quad (8.19)$$

$$|-\uparrow\rangle = -\hat{K} |+\downarrow\rangle. \quad (8.20)$$

Substitution of these relations to $\langle +|\mathbf{r}|-\rangle$ gives

$$\begin{aligned} \langle +|\mathbf{r}|-\rangle &= \langle +\uparrow|\mathbf{r}|-\uparrow\rangle + \langle +\downarrow|\mathbf{r}|-\downarrow\rangle \\ &= -\langle +\uparrow|\mathbf{r}\hat{K}|+\downarrow\rangle + \langle +\downarrow|\mathbf{r}\hat{K}|+\uparrow\rangle \\ &= 0. \end{aligned} \quad (8.21)$$

Therefore, the position operator is proportional to the unit matrix. Thus the expectation value of position operator does not depend on the spin. As a consequence, the electronic polarization from single ion contribution is written as

$$\mathbf{P} = -\frac{e}{V} \text{Tr} \begin{pmatrix} |a|^2 \langle +|\mathbf{r}|+\rangle & 0 \\ 0 & |b|^2 \langle +|\mathbf{r}|+\rangle \end{pmatrix}, \quad (8.22)$$

and thus independent of the spin. This proof disproves the d-p hybridization mechanism in spin $\frac{1}{2}$ systems.

8.5 5-orbital model

In Sec. 8.3, we have introduced the 5-orbital model. This section shows how is the spin-related property such as the magnetism and electronic polarization of this 5-orbital model in $\text{Ba}_2\text{CuGe}_2\text{O}_7$.

The one-electron part of the Hubbard model is constructed from calculated modified MLWFs. After diagonalizing the one-electron part, four groups of the crystal field splitting are obtained as -0.36, -0.34, 0.08 and 0.55 eV. First two levels are the e_g states while the rest is the t_{2g} states.

The Coulomb interactions are calculated by the constrained RPA method which is described in Sec. 7.40. The obtained parameters are $U \approx 0.405$ eV and $J \approx 0.97$ eV.

Then, the superexchange theory is applied to this model. The practical procedure is described in Sec. 7.5. After mapping the 3×3 tensor onto the general spin model Eq. 7.80, parameters are obtained as $J_{ij} = -0.430$ meV, $d_{xy} = 0.109$ meV and $d_z = -0.007$ meV. The traceless symmetric anisotropy $\hat{\Gamma}$ is found quite small values (e.g. the largest value $\Gamma^{xy} = 0.005$ meV) and does not play important role, therefore, it will not be considered in the following. With those parameters, one can have a spin spiral state.

Generally, angle of the spins between nearest-neighbors caused by the DM interaction is given as

$$\theta = \left| \tan^{-1} \left(\frac{d^{xy}}{J} \right) \right| \approx \left| \frac{d^{xy}}{J} \right|. \quad (8.23)$$

It is estimated as $\theta \approx 14.5^\circ$ in the 5-orbital model which is in good agreement with the experimental value of Ref. [103] (9.8°). Details of the spin spiral state will be discussed in the following subsection.

8.5.1 Spin spiral state

DM interaction causes cants of spins. Here an analytical expression of spin-spiral states will be discussed.

Spin spiral states are characterized by spin-spiral propagation \mathbf{q} -vector. The \mathbf{q} -vector specifies the direction of spin-spiral states (Fig. 8.8). Assuming the spins are aligned as a spiral order. Then, a very general definition of the \mathbf{q} -vector is

$$\mathbf{e}_i = \mathbf{n}^1 \cos(\mathbf{q} \cdot \mathbf{R}_i) + \mathbf{n}^2 \sin(\mathbf{q} \cdot \mathbf{R}_i) \quad (8.24)$$

where \mathbf{n}^1 and \mathbf{n}^2 are the unit vectors along a space where the spin plane is spanned in. A vector \mathbf{R}_i denotes a position of the site i which has a classical spin \mathbf{e}_i . Generally, this state can be specified with another vector \mathbf{n}^\perp which is orthogonal to \mathbf{n}^1 and \mathbf{n}^2 .

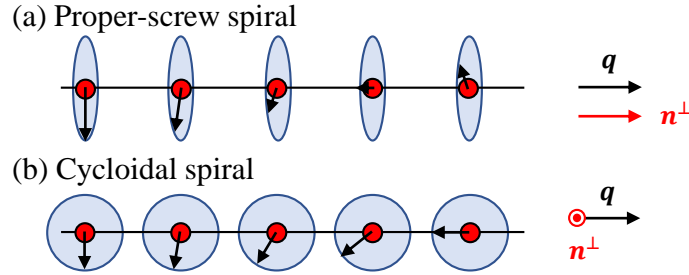


FIGURE 8.8: Two different type of the spin-spiral state with different \mathbf{n}^\perp and same \mathbf{q} -vector. Red spheres and black arrows indicate magnetic sites and spin direction, respectively. Those spin orders are discussed in this chapter. (a) Proper-screw spiral. (b) Cycloidal spiral.

In collinear antiferromagnet state in $Ba_2CuGe_2O_7$ (where two magnetic sites are included in a unit cell, vector \mathbf{R}_i for those sites are $(\pm\frac{1}{2}a, \pm\frac{1}{2}a, 0)$), the \mathbf{q} -vector in the xy -plane is given as $\mathbf{q}_{AFM} = (2\pi/a, 0, 0)$ where a is the lattice parameter. Therefore, one can assume that the spin cants are caused in this plane. Then, the \mathbf{q} -vector is generally given as

$$\mathbf{q} = \mathbf{q}_{AFM} + \delta\mathbf{q} = \left(\frac{2\pi + \delta q_x}{a}, \frac{\delta q_y}{a}, 0 \right) \quad (8.25)$$

with a modulation of the spins $\delta\mathbf{q} = (\delta q_x/a, \delta q_y/a, 0)$. To specify the modulation, consider a general situation that the spins are rotating in a plane one of the \mathbf{n}^1 or \mathbf{n}^2 is $\mathbf{n}^z = (0, 0, 1)$ while another vector is in the xy -plane. In such assumption, the vector normal to this plane is given by

$$\mathbf{n}^\perp = (-\sin\phi, \cos\phi, 0) \quad (8.26)$$

with the azimuth angle ϕ [85]. Then, spin cants are given by Eq. 8.24. Therefore, by considering only nearest-neighbors, one can have an analytical form of the energies of isotropic Heisenberg interaction E_H and DM interaction E_{DM} after some calculation as

$$E_H = 2J - \frac{J}{4}[(\delta q_x)^2 + (\delta q_y)^2] \quad (8.27)$$

and

$$E_{DM} = -\frac{d^{xy}}{\sqrt{2}}(\delta q_x \sin \phi + \delta q_y \cos \phi). \quad (8.28)$$

Then the energy of this system is given as $E_H + E_{DM}$, therefore, minimizing it leads to the analytical expression of the ground state. The condition

$$\frac{\partial(E_H + E_{DM})}{\partial \delta q_x} = 0 \quad (8.29)$$

gives another condition

$$\delta q_x = -\frac{d^{xy}\sqrt{2}}{J} \sin \phi. \quad (8.30)$$

Similarly, another condition

$$\frac{\partial(E_H + E_{DM})}{\partial \delta q_y} = 0 \quad (8.31)$$

gives

$$\delta q_y = -\frac{d^{xy}\sqrt{2}}{J} \cos \phi. \quad (8.32)$$

This result leads to an analytical expression of the modulation of the \mathbf{q} -vector as

$$\delta \mathbf{q} = \delta q(\sin \phi, \cos \phi, 0), \quad (8.33)$$

where $\delta q = -\frac{d^{xy}\sqrt{2}}{J}$. In addition to the modulation vector, minimization of the energy with respect to ϕ , which is given by the condition

$$\frac{\partial(E_H + E_{DM})}{\partial \phi} = 0 \quad (8.34)$$

leads

$$\tan \phi = \frac{\delta q_x}{\delta q_y}. \quad (8.35)$$

Therefore the energy does not depend on ϕ in classical spin model. This can be easily realized by calculating the modulation dependent part of the energy

$$\delta E = -\frac{J}{4}(\delta q)^2 - \frac{d^{xy}}{\sqrt{2}}\delta q = \frac{(d^{xy})^2}{2J}. \quad (8.36)$$

This is corresponding to the energy change caused by the DM interaction.

The important fact here is that not only \mathbf{n}^\perp , but also $\delta \mathbf{q}$ depends on ϕ . Because of this ϕ dependence, one can have several spin spiral structure. For instance, if one chooses $\phi = n \times \frac{\pi}{2} + \frac{\pi}{4}$ where n is an integer. In this situation, one has $\mathbf{n}^\perp = \frac{1}{\sqrt{2}}(\pm 1, \pm 1, 0)$ and $(\delta \mathbf{q} \perp \mathbf{n}^\perp)$ which leads the cycloidal spin spiral order. As another situation, the rotation $\phi = n \times \frac{\pi}{2}$ leads proper screw spin spiral state with $\mathbf{n}^\perp = (\pm 1, 0, 0)$ or $\mathbf{n}^\perp = (0, \pm 1, 0)$ where $(\delta \mathbf{q} \parallel \mathbf{n}^\perp)$. See Fig. 8.9 for the picture of these situation.

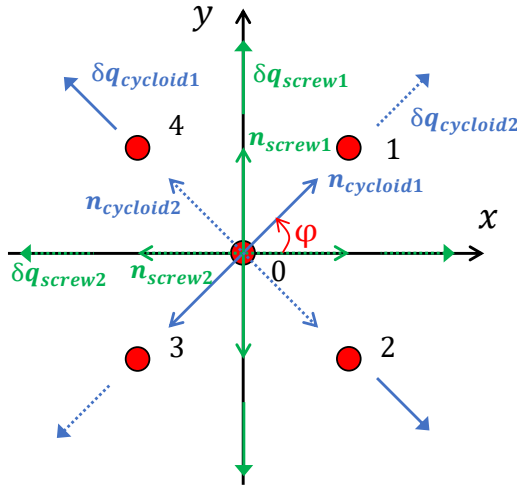


FIGURE 8.9: ϕ dependence of the spin-spiral order in the quasi two-dimensional plane. Direction of the $\delta \mathbf{q}$ and \mathbf{n}^\perp are indicated by solid and dotted arrows. By changing ϕ , one can have two types of the spin-spiral order.

Indeed, this arbitrariness is a consequence of the 4-fold rotoinversion symmetry. If one has 4-fold rotation along z -axis instead, which leads to the change of the symmetric property of DM interaction. This results in a cycloidal spin spiral order for all ϕ .

8.5.2 Without SOC

Another important interaction is the isotropic interaction between layers (next-nearest neighbors). In this case, the constant of such isotropic interaction is found as $J_\perp^2 = -0.010$ meV and thus the interaction between those is antiferromagnetic. As for the isotropic interaction between the 1st neighbor, it was found as $J_\perp^1 = 0.0001$ meV and thus weakly ferromagnetic (see Fig. 8.10).

Therefore, the combination of isotropic interactions between those sites leads to the magnetic structure to a C-type collinear antiferromagnet without SOC. This result coincides with the experimental result [103].

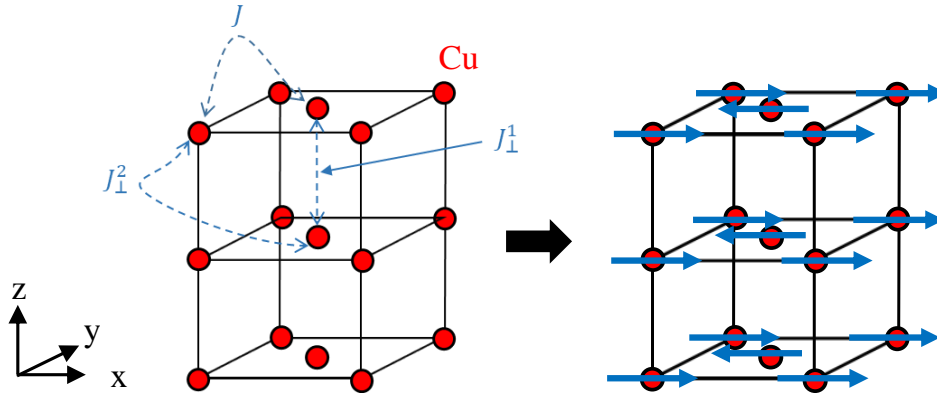


FIGURE 8.10: A picture when without SOC (only isotropic interactions). Only Cu atoms are explicitly shown as Red spheres. Blue arrows on the right panel are indicating the direction of spins. The isotropic interactions stabilize a C-type AFM magnetic structure (Right panel).

8.5.3 Ferroelectricity

This section discusses the magnetically induced ferroelectricity of this material.

Sec. 8.2 has already described that the electronic polarization has some symmetric constraint. Owing to this constraint, the electronic polarization between the nearest neighboring sites of this material only have antisymmetric part \mathcal{P}_{0j} . In addition to this, the sum of the antisymmetric interactions between the nearest-neighbors $\sum_{j \in nn} \mathcal{P}_{0j}$ vanishes. Therefore, as a result, only z -component (out-of-plane component) of the net electronic polarization P_z survives.

The P_z consists of the isotropic interaction P_z^I and the antisymmetric interaction P_z^A . First, let's think of the antisymmetric interaction of the electronic polarization, the second term of Eq. 7.95. This is an analogue of the DM interaction of the magnetic energy. This interaction is originated from the spin-current ($e_i \times e_j$). Then, adopt the same strategy with the analysis of the spin spiral states.

Consider the vector normal to the spin rotation plane Eq. 8.26 and spin spiral propagation vector Eq. 8.33. Furthermore, assume the spin at the site 0 is $e_0 = (0, 0, 1)$. Then, the spin at the site j can be written by using Eq. 8.24 as

$$e_j = n^1 \cos(\mathbf{q} \cdot \mathbf{R}_j) + n^2 \sin(\mathbf{q} \cdot \mathbf{R}_j), \quad (8.37)$$

where $\mathbf{n}^1 = (0, 0, 1)$ and $\mathbf{n}^2 = (\cos \phi, \sin \phi, 0)$. The next-nearest neighboring sites at adjacent planes are given as

$$\mathbf{R}_j = \epsilon_{j0} \sqrt{\frac{1}{2}a^2 + c^2}, \quad (8.38)$$

where the unit vector ϵ_{j0} for those neighbors are given as $\epsilon_{j0} = \frac{\tau_{j0}}{|\tau_{j0}|}$ with the vectors connecting those sites $\tau_{j0} = (\pm \frac{1}{2}a, \pm \frac{1}{2}a, \pm c)$ (see Fig. 8.6 (d) for the situation).

With these considerations, the outer products of spins at those sites are

$$\begin{aligned} \mathbf{e}_0 \times \mathbf{e}_j &= -\mathbf{n}^x \sin \phi \sin(\mathbf{q} \cdot \mathbf{R}_j) + \mathbf{n}^y \cos \phi \sin(\mathbf{q} \cdot \mathbf{R}_j) \\ &= \mathbf{n}^\perp \sin(\mathbf{q} \cdot \mathbf{R}_j) \\ &\approx \mathbf{n}^\perp(\mathbf{q} \cdot \mathbf{R}_j) \\ &= -\mathbf{n}^\perp \delta q \sqrt{\frac{1}{2}a^2 + c^2} (\epsilon_{j0}^x \sin \phi + \epsilon_{j0}^y \cos \phi), \end{aligned} \quad (8.39)$$

where \mathbf{n}^x and \mathbf{n}^y are the unit vector along x and y , respectively. Now, use the analytical expression for the antisymmetric interaction between next-nearest neighbors Eq. 8.5. Then, one can have

$$\begin{aligned} \mathcal{P}_{0j} \cdot \mathbf{n}^\perp &= \pm p_\perp^{xy} \mathbf{n}^\perp \cdot [\epsilon_{j0} \times \mathbf{n}^z] \\ &= \mp p_\perp^{xy} (\epsilon_{j0}^y \sin \phi + \epsilon_{j0}^x \cos \phi). \end{aligned} \quad (8.40)$$

By using this expression, one can derive analytical expression for the antisymmetric contribution of the electronic polarization between next-nearest neighbors as

$$\mathcal{P}_{0j} \cdot [\mathbf{e}_0 \times \mathbf{e}_j] = \pm \delta q \frac{p_\perp^{xy}}{4\sqrt{\frac{1}{2}a^2 + c^2}} (\sin 2\phi + (-1)^{j+1}), \quad (8.41)$$

where the relations $(\epsilon_{j0}^x)^2 = (\epsilon_{j0}^y)^2 = \frac{a^2}{2a^2+4c^2}$ and $\epsilon_{j0}^x \epsilon_{j0}^y = (-1)^{j+1} \frac{a^2}{2a^2+4c^2}$ are used. Then, by summing up this expression for all next-nearest neighbors, one can have a desired form for the z -component of the net electronic polarization of the antisymmetric part as

$$\begin{aligned} P_z^A &= \sum_{j \in \text{next-nn}} \epsilon_{j0}^z (\mathcal{P}_{0j} \cdot [\mathbf{e}_0 \times \mathbf{e}_j]) \\ &= \frac{4p_\perp^{xy} ac}{a^2 + 2c^2} \delta q \sin 2\phi \\ &= -\frac{4\sqrt{2}p_\perp^{xy} ac}{a^2 + 2c^2} \frac{d^{xy}}{J} \sin 2\phi. \end{aligned} \quad (8.42)$$

The important character is the $\sin 2\phi$ dependence of the electronic polarization. This is a consequence of two different ϕ -dependence. Namely, the outer

product ($e_i \times e_j$) gives $\sin \phi$ dependence. Besides it, the spin spiral propagation \mathbf{q} -vector has $\sin \phi$ and $\cos \phi$ dependence which result in the rotoinversion symmetry. Thus, these lead to the $\sin 2\phi$ dependence.

Similar procedure can be applied to the isotropic part of the electronic polarization. Now, think of the inner product of spins between next-nearest neighbors:

$$\begin{aligned}
\mathbf{e}_0 \cdot \mathbf{e}_j &= \cos(\mathbf{q} \cdot \mathbf{R}_j) \\
&= -\cos \left(\frac{1}{a} \sqrt{\frac{1}{2}a^2 + c^2} \left(\epsilon_{j0}^x \delta q \sin \phi + \epsilon_{j0}^y \delta q \cos \phi \right) \right) \\
&\approx -1 + \frac{(\delta q)^2}{2a^2} \left(\frac{1}{2}a^2 + c^2 \right) (\epsilon_{j0}^x \sin \phi + \epsilon_{j0}^y \cos \phi)^2 \\
&= -1 + \frac{(\delta q)^2}{8} \left(1 + (-1)^{j+1} \sin 2\phi \right)
\end{aligned} \tag{8.43}$$

Subsequently, z-component of the net electronic polarization of the isotropic interaction P_z^I is given by summing it up for all next-nearest neighbors as

$$\begin{aligned}
P_z^I &= \sum_{j \in \text{next-nn}} \epsilon_{j0}^z P_{0j} (\mathbf{e}_0 \cdot \mathbf{e}_j) \\
&= \sum_{j \in \text{next-nn}} \epsilon_{j0}^z \left((-1)^j t_{j0} p_{\perp}^0 \frac{(\delta q)^2}{8} (-1)^{j+1} \sin 2\phi \right) \\
&= -\frac{2\sqrt{2}c}{\sqrt{a^2 + c^2}} \left(\frac{d^{xy}}{J} \right)^2 p_{\perp}^0 \sin 2\phi.
\end{aligned} \tag{8.44}$$

Again, the isotropic part also has the $\sin 2\phi$ dependence.

As a consequence, the total non-zero electronic polarization $P_z = P_z^A + P_z^I$ gives $\sin 2\phi$ dependence. Due to the $\sin 2\phi$ dependence, this theoretical analysis reproduces a switching of a direction of the electronic polarization as it has been experimentally seen in Ref. [96]. With $\phi = \frac{\pi}{4}$, the spin spiral structure is cycloidal and it is experimentally observed spin structure. In such configuration, the electronic polarization of the z-component is positive. This spin structure will be stabilized with the magnetic field for instance, along $[\bar{1}, \bar{1}, 0]$ with a canting of spins (see Fig. 8.11 (b)). In contrast, a magnetic field along $[1, 1, 0]$ stabilizes the cycloidal spin spiral structure with $\phi = -\frac{\pi}{4}$ and also cants of spins. Indeed, this spin structure gives the z-component of the electronic polarization with the opposite sign (negative) (see Fig. 8.11 (c)). This behavior is exactly what has been observed in Ref. [96].

Concerning the value, the value observed in the experiment [96] is $|P_z| \approx 0.3 \mu\text{C}/m^2$. Theoretical values calculated from 5-orbital model are rather small $P_z^A + P_z^I \approx 0.505 p_{\perp}^{xy} - 0.086 p_{\perp}^0 = 0.02 \mu\text{C}/m^2$ ($\phi = \frac{\pi}{4}$) with $p_{\perp}^{xy} = 0.046 \mu\text{C}/m^2$ and $p_{\perp}^0 = 0.037 \mu\text{C}/m^2$. An attention should be paid that these values are really sensitive to details of the calculation, therefore, there are many possibilities for the reason of this discrepancy. For example, quality of the Wannier functions constructed from MLWF method for this material is

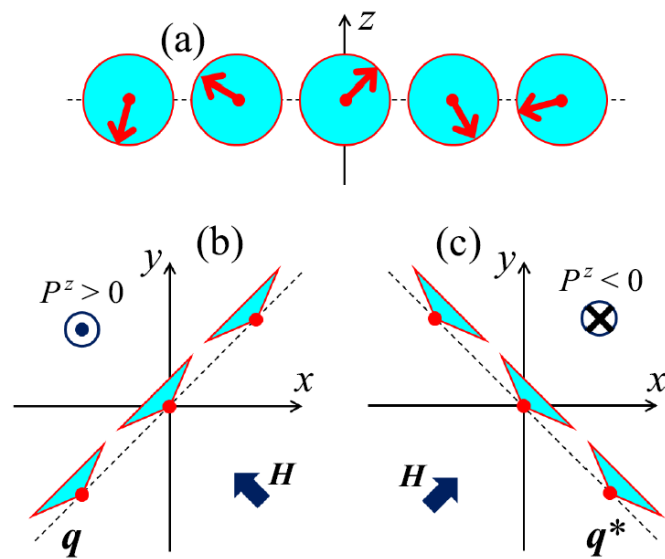


FIGURE 8.11: Suggested flip of the out-of-plane electronic polarization by the external magnetic field in the spin-spiral state. (a) Side view of the spin-spiral states. (b) and (c) are top-view of the spin-spiral alignment along side with the electronic polarization suggested by the SE theory for the electronic polarization.

quite bad, therefore, modified MLWF method is employed. Wannier function should play a crucial role of the models. Another possibility is the Coulomb interaction. In this work, it has been calculated by constrained RPA method and which also should play an important role.

Another important fact is that the antisymmetric contribution of the electronic polarization P_z^A is much larger than that of the isotropic interaction P_z^I . Therefore, the magnetically induced electronic polarization of $\text{Ba}_2\text{CuGe}_2\text{O}_7$ is almost solely induced by the spin-current mechanism. This is completely different from the analysis done by Murakawa et al. [97]; their argument was that the origin of the ME effect in $\text{Ba}_2\text{CuGe}_2\text{O}_7$ is induced by the d-p hybridization mechanism, but here the spin-current mechanism is the origin.

8.5.4 Response to external fields in collinear C-type AFM phase

Another interesting behavior of this material is observed when one applies a magnetic field perpendicular to the quasi two dimensional surface, magnetic structure transits as incommensurate spin spiral \rightarrow commensurate AFM (C-type) [102]. This section performs a thought experiment and predict the electronic polarization caused during this incommensurate-commensurate (IC-C) transition.

As it has been observed in the experiment [102], spins lie in the quasi two-dimensional plane in the commensurate phase. With the C-type antiferromagnet alone, the electronic polarization is not induced, however, the external magnetic field further causes cants of spins along z-axis. In other words, the C-type antiferromagnetic alignment lowers the the 4-fold rotoinversion \hat{S}_4^z to time-reversal and 2-fold rotation $\hat{T}\hat{C}_2^z$, thus, it allows one to have an in-plane electronic polarization P_{xy} [100]. Then, further cants of the spins break this symmetry. To see this behavior more closely, a quantitative analysis will be given. The spin cants are estimated by the equilibrium condition between isotropic interaction and Zeeman effect as

$$e^z = -\frac{\mu_B H}{8J}, \quad (8.45)$$

where μ_B is the Bohr magneton and H is the strength of the external magnetic perpendicular to the plane.

Since the next nearest neighbor bonds contribute to out-of-plane electronic polarization P_z , one can assume the in-plane electronic polarization is mainly coming from the in-plane nearest neighboring bonds. Now, assume the spin at the site 0 is $e_0 = (\cos \phi, \sin \phi, e^z)$ and its neighboring sites $e_j = (-\cos \phi, -\sin \phi, e^z)$. This is a special case of the spin spiral where the spin spiral q -vector is collinear antiferromagnetic. With a canting e^z . The outer product of these spins is then

$$e_0 \times e_j = 2e^z(\sin \phi, -\cos \phi, 0). \quad (8.46)$$

From Eq. 8.4, one can have the desired form of the in-plane electronic polarization \mathbf{P}_{xy} :

$$\begin{aligned} \mathbf{P}_{xy} &= \sum_{j \in nn} \epsilon_{j0} \mathcal{P}_{0j} [\mathbf{e}_0 \times \mathbf{e}_j] \\ &= \sum_{j \in nn} \epsilon_{j0} 2(-1)^j e^z p_{\parallel}^{xy} (\epsilon_{j0}^x \sin \phi - \epsilon_{j0}^y \cos \phi) \\ &= -\frac{\mu_B H p_{\parallel}^{xy}}{2J} (\cos \phi, -\sin \phi, 0). \end{aligned} \quad (8.47)$$

The 5-orbital model gives $p_{\parallel}^{xy} = 0.597 \mu C/m^2$. This is the linear effect as it gives a linear dependence of the external magnetic field. In the ground state configuration where $\phi = n \times \frac{\pi}{2} + \frac{\pi}{4}$ where n is an integer, the C-type AFM can have four possible formations. In all cases, this theoretical analysis predicts several direction of the in-plane electronic polarization (Fig. 8.12). Therefore, this subsection concludes there is another possibility of the electronic polarization controlled by external magnetic fields. This provides another possibility of the application of $Ba_2CuGe_2O_7$.

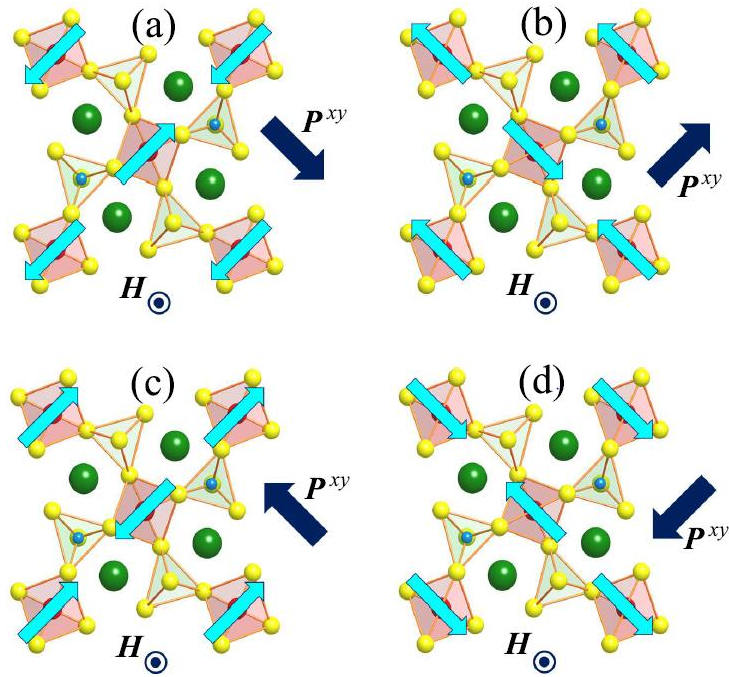


FIGURE 8.12: (a-d) All possible in-plane electronic polarization predicted by the SE theory for the electronic polarization caused by IC-C transition and additional spin cants.

8.6 Conclusion and future prospect

In the last part of this thesis, first, conventional linear ME effect has been introduced. After that, present theories and controversy of those have been discussed. At the end, mechanism of the non-linear ME effect in $\text{Ba}_2\text{CuGe}_2\text{O}_7$ has been revealed by combining one-electron approximation and many-body theory. Furthermore, this part showed contrary to the wide spread belief, the single site mechanism of the electronic polarization cannot exist in spin $\frac{1}{2}$ system such as $\text{Ba}_2\text{CuGe}_2\text{O}_7$. At this point, we saw in the atomic-limit, by expanding atomic-limit Wannier functions by means of the first order of the hopping, one can have tails spreading to neighboring sites. By using these tails and rigorous Berry phase expression for the electronic polarization in solids, one can systematically derive spin model of the electronic polarization. In contrast to the present phenomenological theories, this is the first logically derived spin model of the electronic polarization. The derived SE theory for the electronic polarization is the analogue of the well known SE theory for the magnetic energy. The difference is only the vector which gives information of symmetry property of the crystal. One of the character of the SE theory for the electronic polarization is that this theory treats isotropic and antisymmetric contributions to the electronic polarization on an equal footing. Moreover, the advantage is that we can use same parameters which used in the SE theory of the magnetic energies. The theory has nicely described the experimental multiferroic behavior of $\text{Ba}_2\text{CuGe}_2\text{O}_7$. Moreover, the theory predicts interesting in-plane polarization switching. Another interesting suggestion in this part is a new algorithm for the construction of the Wannier functions which obey symmetric property of the crystal. This is crucially important for microscopic modelings from the first-principle calculations. This section conclude the proposed theory revealed that the origin of the ME effect in $\text{Ba}_2\text{CuGe}_2\text{O}_7$ is the spin-current mechanism.

Finally, let me discuss the future prospect. The suggested SE theory for the electronic polarization is successful theory, however, it seems still there are some mechanism missing in the theory. One of the crucial assumption of the SE theory for the electronic polarization is that the overlap between tail and head $\langle a_i | \mathbf{r} | a_{i \rightarrow j} \rangle$ can be ignored. However, one should be careful of this because this is the first-order of the hopping, thus, may have more contribution than second-order of the hopping. Indeed, if one takes into account such effects, one should have better agreement of the value for the electronic polarization (it was not in agreement in the SE theory, actually). This thesis concludes if those controversies are solved, it would be a significant step forward for applications in future electronic devices.

Chapter 9

Summary

First, this thesis provided the matching method for Angle-Resolved Photoemission Spectroscopy (ARPES) which can be used in combination with the surface slab model Density Functional Theory calculations. After the suggestion, the method is adopted to a graphene-like one-dimensional periodic potential model. The result showed good agreement with the analytical solution.

Next, this thesis showed how the hole and electron pocket of T_d phase MoTe_2 can be selected in ARPES experiments by means of the dipole selection rule and suggested suitable ARPES setting for the future ARPES experiments.

Finally, this thesis introduced a SE theory for magnetically induced electronic polarization. The theory is successfully adopted to a controversial multiferroics $\text{Ba}_2\text{CuGe}_2\text{O}_7$ and the mechanism of the magnetoelectric effect in $\text{Ba}_2\text{CuGe}_2\text{O}_7$ is explained.

Bibliography

- [1] P. Puschnig, S. Berkebile, A. J. Fleming, G. Koller, K. Emtsev, T. Seyller, J. D. Riley, C. Ambrosch-Draxl, F. P. Netzer, and M. G. Ramsey, “Reconstruction of molecular orbital densities from photoemission data”, *Science* **326**, 702 (2009).
- [2] J. Braun, “The theory of angle-resolved ultraviolet photoemission and its applications to ordered materials”, *Rep. on Prog. in Phys.* **59**, 1267 (1996).
- [3] J. Braun, J. Minár, and H. Ebert, “Correlation, temperature and disorder: recent developments in the one-step description of angle-resolved photoemission”, *Physics Reports* **740**, 1 (2018).
- [4] K. Kambe, “A KKR method for two-dimensional lattices and its application to band calculation”, in *Computational methods in band theory: proceedings of a conference held at the ibm thomas j. watson research center, yorktown heights, new york, may 14–15, 1970, under the joint sponsorship of ibm and the american physical society*, edited by P. M. Marcus, J. F. Janak, and A. R. Williams (Springer US, Boston, MA, 1971), pp. 409–415.
- [5] F. Máca and M. Scheffler, “Surface green’s function for a ruffled crystal surface”, *Computer Physics Communications* **51**, 381 (1988).
- [6] B. A. Bernevig, T. L. Hughes, and S.-C. Zhang, “Quantum spin hall effect and topological phase transition in hgte quantum wells”, *Science* **314**, 1757 (2006).
- [7] H. Nielsen and M. Ninomiya, “The adler-bell-jackiw anomaly and weyl fermions in a crystal”, *Phys. Lett. B* **130**, 389 (1983).
- [8] H.-J. Kim, K.-S. Kim, J.-F. Wang, M. Sasaki, N. Satoh, A. Ohnishi, M. Kitaura, M. Yang, and L. Li, “Dirac versus weyl fermions in topological insulators: adler-bell-jackiw anomaly in transport phenomena”, *Phys. Rev. Lett.* **111**, 246603 (2013).
- [9] P. Hosur, S. A. Parameswaran, and A. Vishwanath, “Charge transport in weyl semimetals”, *Phys. Rev. Lett.* **108**, 046602 (2012).
- [10] S. A. Parameswaran, T. Grover, D. A. Abanin, D. A. Pesin, and A. Vishwanath, “Probing the chiral anomaly with nonlocal transport in three-dimensional topological semimetals”, *Phys. Rev. X* **4**, 031035 (2014).
- [11] S. Hüfner, *Photoelectron Spectroscopy: Principles and Applications* (Springer Science and Business Media, 2003).
- [12] H. Hertz, “Über strahlen electricischer kraft”, *Annalen der Physik* **272**, 769 (1889).

- [13] A. Einstein, "Über die von der molekularkinetischen theorie der wärme geforderte bewegung von in ruhenden flüssigkeiten suspendierten teilchen", *Annalen der Physik* **322**, 549 (1905).
- [14] D. R. Penn, "Electron mean-free-path calculations using a model dielectric function", *Phys. Rev. B* **35**, 482 (1987).
- [15] J. B. Pendry, "Theory of photoemission", *Surf. Sci.* **57**, 679 (1976).
- [16] P. Puschnig and D. Lüftner, "Simulation of angle-resolved photoemission spectra by approximating the final state by a plane wave: from graphene to polycyclic aromatic hydrocarbon molecules", *Journal of Electron Spectroscopy and Related Phenomena* **200**, 193 (2015).
- [17] A. M. Bradshaw and D. P. Woodruff, "Molecular orbital tomography for adsorbed molecules: is a correct description of the final state really unimportant?", *New Journal of Physics* **17**, 013033 (2015).
- [18] G. Kresse and J. Furthmüller, "Efficient iterative schemes for ab initio total-energy calculations using a plane-wave basis set", *Phys. Rev. B* **54**, 11169 (1996).
- [19] R. Ono and P. Krüger, "A one-dimensional model for photoemission calculations from plane-wave band structure codes", *e-Journal of Surface Science and Nanotechnology* **16**, 49 (2018).
- [20] C. L. Kane and E. J. Mele, "Quantum spin hall effect in graphene", *Phys. Rev. Lett.* **95**, 226801 (2005).
- [21] T. Wehling, A. Black-Schaffer, and A. Balatsky, "Dirac materials", *Advances in Physics* **63**, 1 (2014).
- [22] M. V. Berry, "Quantal phase factors accompanying adiabatic changes", *Proceedings of the Royal Society of London. Series A, Mathematical and Physical Sciences* **392**, 45 (1984).
- [23] R. Okugawa and S. Murakami, "Dispersion of fermi arcs in weyl semimetals and their evolutions to dirac cones", *Phys. Rev. B* **89**, 235315 (2014).
- [24] A. A. Soluyanov, D. Gresch, Z. Wang, Q. Wu, M. Troyer, X. Dai, and B. A. Bernevig, "Type-II Weyl semimetals", *Nature* **527**, 495 (2015).
- [25] M. N. Ali, J. Xiong, S. Flynn, J. Tao, Q. D. Gibson, L. M. Schoop, T. Liang, N. Haldolaarachchige, M. Hirschberger, N. P. Ong, and R. J. Cava, "Large, non-saturating magnetoresistance in WTe₂", *Nature* **514**, 205 (2014).
- [26] H. Weng, C. Fang, Z. Fang, B. A. Bernevig, and X. Dai, "Weyl semimetal phase in noncentrosymmetric transition-metal monophosphides", *Phys. Rev. X* **5**, 011029 (2015).
- [27] Z. Li, H. Chen, S. Jin, D. Gan, W. Wang, L. Guo, and X. Chen, "Weyl semimetal taas: crystal growth, morphology, and thermodynamics", *Crystal Growth & Design* **16**, 1172 (2016).

- [28] B. Q. Lv, H. M. Weng, B. B. Fu, X. P. Wang, H. Miao, J. Ma, P. Richard, X. C. Huang, L. X. Zhao, G. F. Chen, Z. Fang, X. Dai, T. Qian, and H. Ding, "Experimental discovery of weyl semimetal taas", *Phys. Rev. X* **5**, 031013 (2015).
- [29] Y. Sun, S.-C. Wu, M. N. Ali, C. Felser, and B. Yan, "Prediction of weyl semimetal in orthorhombic MoTe_2 ", *Phys. Rev. B* **92**, 161107 (2015).
- [30] F. Y. Bruno, A. Tamai, Q. S. Wu, I. Cucchi, C. Barreateau, A. de la Torre, S. McKeown Walker, S. Riccò, Z. Wang, T. K. Kim, M. Hoesch, M. Shi, N. C. Plumb, E. Giannini, A. A. Soluyanov, and F. Baumberger, "Observation of large topologically trivial fermi arcs in the candidate type-ii weyl semimetal WTe_2 ", *Phys. Rev. B* **94**, 121112 (2016).
- [31] L. Brixner, "Preparation and properties of the single crystalline ab2-type selenides and tellurides of niobium, tantalum, molybdenum and tungsten", *Journal of Inorganic and Nuclear Chemistry* **24**, 257 (1962).
- [32] A. Jain, S. P. Ong, G. Hautier, W. Chen, W. D. Richards, S. Dacek, S. Cholia, D. Gunter, D. Skinner, G. Ceder, and K. a. Persson, "Commentary: The Materials Project: A materials genome approach to accelerating materials innovation", *APL Materials* **1**, 011002 (2013).
- [33] A. Crepaldi, G. Autès, A. Sterzi, G. Manzoni, M. Zacchigna, F. Cilento, I. Vobornik, J. Fujii, P. Bugnon, A. Magrez, H. Berger, F. Parmigiani, O. V. Yazyev, and M. Grioni, "Persistence of a surface state arc in the topologically trivial phase of MoTe_2 ", *Phys. Rev. B* **95**, 041408 (2017).
- [34] A Tamai, Q. S. Wu, I Cucchi, F. Y. Bruno, S Riccò, T. K. Kim, M Hoesch, C Barreateau, E Giannini, C Besnard, A. A. Soluyanov, and F Baumberger, "Fermi arcs and their topological character in the candidate type-ii weyl semimetal MoTe_2 ", *Phys. Rev. X* **6**, 31021 (2016).
- [35] D. Di Sante, P. K. Das, C. Bigi, Z. Ergönenc, N. Gürtler, J. A. Krieger, T. Schmitt, M. N. Ali, G. Rossi, R. Thomale, C. Franchini, S. Picozzi, J. Fujii, V. N. Strocov, G. Sangiovanni, I. Vobornik, R. J. Cava, and G. Panaccione, "Three-dimensional electronic structure of the type-ii weyl semimetal WTe_2 ", *Phys. Rev. Lett.* **119**, 026403 (2017).
- [36] G. Kresse and D. Joubert, "From ultrasoft pseudopotentials to the projector augmented-wave method", *Phys. Rev. B* **59**, 1758 (1999).
- [37] P. E. Blöchl, "Projector augmented-wave method", *Phys. Rev. B* **50**, 17953 (1994).
- [38] J. P. Perdew and A. Zunger, "Self-interaction correction to density-functional approximations for many-electron systems", *Phys. Rev. B* **23**, 5048 (1981).
- [39] Y. Qi, P. G. Naumov, M. N. Ali, C. R. Rajamathi, W. Schnelle, O. Barkalov, M. Hanfland, S.-C. Wu, C. Shekhar, Y. Sun, V. Süß, M. Schmidt, U. Schwarz, E. Pippel, P. Werner, R. Hillebrand, T. Förster, E. Kampert, S. Parkin, R. J. Cava, C. Felser, B. Yan, and S. A. Medvedev, "Superconductivity in weyl semimetal candidate mote_2 ", *Nature Communications* **7**, 11038 (2016).

- [40] H Ebert, D Ködderitzsch, and J Minár, “Calculating condensed matter properties using the KKR-green’s function method—recent developments and applications”, *Rep. on Prog. in Phys.* **74**, 096501 (2011).
- [41] M. Fanciulli, J. Schusser, M.-I. Lee, Z. E. Youbi, O. Heckmann, M. C. Richter, C. Cacho, C. Spezzani, D. Bresteau, J.-F. m. c. Hergott, P. D’Oliveira, O. Tcherbakoff, T. Ruchon, J. Minár, and K. Hricovini, “Spin, time, and angle resolved photoemission spectroscopy on WTe₂”, *Phys. Rev. Research* **2**, 013261 (2020).
- [42] J. Schusser, L. Nicolai, M. Fanciulli, M. I. Lee, Z. E. Youbi, O. Heckmann, C. Richter, K. Hricovini, and J. Minár, “Angle-resolved photoemission calculations of WTe₂ compared to experiment”, *AIP Conf. Proc.* **2131**, 20041 (2019).
- [43] S. Goldberg, C. Fadley, and S. Kono, “Photoionization cross-sections for atomic orbitals with random and fixed spatial orientation”, *Journal of Electron Spectroscopy and Related Phenomena* **21**, 285 (1981).
- [44] Curie, P., “Sur la symétrie dans les phénomènes physiques, symétrie d’un champ électrique et d’un champ magnétique”, *J. Phys. Theor. Appl.* **3**, 393 (1894).
- [45] I. E. Dzyaloshinskii, “On the magneto-electrical effect in antiferromagnets”, *Journal of Experimental and Theoretical Physics* **10**, 628 (1960).
- [46] T. Kimura, T. Goto, H. Shintani, K. Ishizaka, T. Arima, and Y. Tokura, “Magnetic control of ferroelectric polarization”, *Nature* **426**, 55 (2003).
- [47] T. Goto, T. Kimura, G. Lawes, A. P. Ramirez, and Y. Tokura, “Ferroelectricity and giant magnetocapacitance in perovskite rare-earth manganites”, *Phys. Rev. Lett.* **92**, 257201 (2004).
- [48] M. Kenzelmann, A. B. Harris, S. Jonas, C. Broholm, J. Schefer, S. B. Kim, C. L. Zhang, S.-W. Cheong, O. P. Vajk, and J. W. Lynn, “Magnetic inversion symmetry breaking and ferroelectricity in TbMnO₃”, *Phys. Rev. Lett.* **95**, 087206 (2005).
- [49] D. N. Astrov, “The magnetoelectric effect in antiferromagnetics”, *Journal of Experimental and Theoretical Physics* **11**, 708 (1960).
- [50] V. J. Folen, G. T. Rado, and E. W. Stalder, “Anisotropy of the magneto-electric effect in Cr₂O₃”, *Phys. Rev. Lett.* **6**, 607 (1961).
- [51] S. Kasap, *Principles of electronic materials and devices*, 3rd ed. (McGraw-Hill, Inc., USA, 2005).
- [52] J. F. Alexander K. Tagantsev L. Eric Crossi, *Domains in ferroic crystals and thin films*, 1st ed. (Springer-Verlag New York, 2010).
- [53] M. C. Cross and D. S. Fisher, “A new theory of the spin-peierls transition with special relevance to the experiments on ttfcubdt”, *Phys. Rev. B* **19**, 402 (1979).
- [54] B. Lorenz, Y.-Q. Wang, and C.-W. Chu, “Ferroelectricity in perovskite HoMnO₃ and YMnO₃”, *Phys. Rev. B* **76**, 104405 (2007).

- [55] H. Katsura, N. Nagaosa, and A. V. Balatsky, "Spin current and magnetoelectric effect in noncollinear magnets", *Phys. Rev. Lett.* **95**, 057205 (2005).
- [56] C. Jia, S. Onoda, N. Nagaosa, and J. H. Han, "Bond electronic polarization induced by spin", *Phys. Rev. B* **74**, 224444 (2006).
- [57] C. Jia, S. Onoda, N. Nagaosa, and J. H. Han, "Microscopic theory of spin-polarization coupling in multiferroic transition metal oxides", *Phys. Rev. B* **76**, 144424 (2007).
- [58] T.-h. Arima, "Ferroelectricity induced by proper-screw type magnetic order", *Journal of the Physical Society of Japan* **76**, 073702 (2007).
- [59] D. Okuyama, S. Ishiwata, Y. Takahashi, K. Yamauchi, S. Picozzi, K. Sugimoto, H. Sakai, M. Takata, R. Shimano, Y. Taguchi, T. Arima, and Y. Tokura, "Magnetically driven ferroelectric atomic displacements in orthorhombic YMnO_3 ", *Phys. Rev. B* **84**, 054440 (2011).
- [60] Y. Yamasaki, H. Sagayama, T. Goto, M. Matsuura, K. Hirota, T. Arima, and Y. Tokura, "Electric control of spin helicity in a magnetic ferroelectric", *Phys. Rev. Lett.* **98**, 147204 (2007).
- [61] T. Kimura, J. C. Lashley, and A. P. Ramirez, "Inversion-symmetry breaking in the noncollinear magnetic phase of the triangular-lattice antiferromagnet CuFeO_2 ", *Phys. Rev. B* **73**, 220401 (2006).
- [62] S. Mitsuda, N. Kasahara, T. Uno, and M. Mase, "Partially disordered phase in frustrated triangular lattice antiferromagnet CuFeO_2 ", *Journal of the Physical Society of Japan* **67**, 4026 (1998).
- [63] G. Quirion, M. J. Tagore, M. L. Plumer, and O. A. Petrenko, "Evidence of soft modes in magnetoelectric CuFeO_2 : ultrasonic velocity measurements and Landau theory", *Phys. Rev. B* **77**, 094111 (2008).
- [64] J. Hubbard, "Electron correlations in narrow energy bands", *Proc. R. Soc. Lond. A* **276**, 238 (1963).
- [65] S. A. Nikolaev and I. V. Solovyev, "Microscopic theory of electric polarization induced by skyrmionic order in GaV_4S_8 ", *Phys. Rev. B* **99**, 100401 (2019).
- [66] I. V. Solovyev, "Combining DFT and many-body methods to understand correlated materials", *Journal of Physics: Condensed Matter* **20**, 293201 (2008).
- [67] S. A. Nikolaev, I. V. Solovyev, A. N. Ignatenko, V. Y. Irkhin, and S. V. Streltsov, "Realization of the anisotropic compass model on the diamond lattice of Cu^{2+} in CuAl_2O_4 ", *Phys. Rev. B* **98**, 201106 (2018).
- [68] G. H. Wannier, "The structure of electronic excitation levels in insulating crystals", *Phys. Rev.* **52**, 191 (1937).
- [69] N. Marzari and D. Vanderbilt, "Maximally localized generalized Wannier functions for composite energy bands", *Phys. Rev. B* **56**, 12847 (1997).

- [70] N. Marzari, A. A. Mostofi, J. R. Yates, I. Souza, and D. Vanderbilt, "Maximally localized wannier functions: theory and applications", *Rev. Mod. Phys.* **84**, 1419 (2012).
- [71] E. Blount, in , Vol. 13, edited by F. Seitz and D. Turnbull, Solid State Physics (Academic Press, 1962), pp. 305–373.
- [72] R. Wang, E. A. Lazar, H. Park, A. J. Millis, and C. A. Marianetti, "Selectively localized wannier functions", *Phys. Rev. B* **90**, 165125 (2014).
- [73] R. Ono, S. Nikolaev, and I. Solovyev, "Fingerprints of spin-current physics on magnetoelectric response in the spin- $\frac{1}{2}$ magnet $\text{Ba}_2\text{CuGe}_2\text{O}_7$ ", *Phys. Rev. B* **102**, 064422 (2020).
- [74] A. I. Liechtenstein, V. I. Anisimov, and J. Zaanen, "Density-functional theory and strong interactions: orbital ordering in mott-hubbard insulators", *Phys. Rev. B* **52**, R5467 (1995).
- [75] F. Aryasetiawan, M. Imada, A. Georges, G. Kotliar, S. Biermann, and A. I. Lichtenstein, "Frequency-dependent local interactions and low-energy effective models from electronic structure calculations", *Phys. Rev. B* **70**, 195104 (2004).
- [76] F. Aryasetiawan, K. Karlsson, O. Jepsen, and U. Schönberger, "Calculations of hubbard u from first-principles", *Phys. Rev. B* **74**, 125106 (2006).
- [77] Y. Nomura, M. Kaltak, K. Nakamura, C. Taranto, S. Sakai, A. Toschi, R. Arita, K. Held, G. Kresse, and M. Imada, "Effective on-site interaction for dynamical mean-field theory", *Phys. Rev. B* **86**, 085117 (2012).
- [78] I. Dzyaloshinsky, "A thermodynamic theory of "weak" ferromagnetism of antiferromagnetics", *Journal of Physics and Chemistry of Solids* **4**, 241 (1958).
- [79] T. Moriya, "Anisotropic superexchange interaction and weak ferromagnetism", *Phys. Rev.* **120**, 91 (1960).
- [80] P. W. Anderson, "New approach to the theory of superexchange interactions", *Phys. Rev.* **115**, 2 (1959).
- [81] I. V. Solovyev, "Lattice distortion and magnetism of $3d - t_{2g}$ perovskite oxides", *Phys. Rev. B* **74**, 054412 (2006).
- [82] I. V. Solovyev, "First-principles wannier functions and effective lattice fermion models for narrow-band compounds", *Phys. Rev. B* **73**, 155117 (2006).
- [83] I. V. Solovyev, "Spin-orbital superexchange physics emerging from interacting oxygen molecules in KO_2 ", *New Journal of Physics* **10**, 013035 (2008).
- [84] I. V. Solovyev, "Superexchange interactions in orthorhombically distorted titanates RTiO_3 ($r = y, \text{gd}, \text{sm}$ and la)", *New Journal of Physics* **11**, 093003 (2009).
- [85] I. V. Solovyev, "Self-consistent linear response for the spin-orbit interaction related properties", *Phys. Rev. B* **90**, 024417 (2014).

- [86] I. V. Solovyev, "Superexchange theory of electronic polarization driven by relativistic spin-orbit interaction at half filling", *Phys. Rev. B* **95**, 214406 (2017).
- [87] S. A. Nikolaev and I. V. Solovyev, "Skyrmionic order and magnetically induced polarization change in lacunar spinel compounds GaV_4S_8 and GaMo_4S_8 : comparative theoretical study", *Phys. Rev. B* **102**, 014414 (2020).
- [88] R. D. King-Smith and D. Vanderbilt, "Theory of polarization of crystalline solids", *Phys. Rev. B* **47**, 1651 (1993).
- [89] R. Resta, "Theory of the electric polarization in crystals", *Ferroelectrics* **136**, 51 (1992).
- [90] R. Resta, "Quantum-mechanical position operator in extended systems", *Phys. Rev. Lett.* **80**, 1800 (1998).
- [91] N. A. Spaldin, "A beginner's guide to the modern theory of polarization", *Journal of Solid State Chemistry* **195**, 2 (2012).
- [92] R. Resta, "Electrical polarization and orbital magnetization: the modern theories", *Journal of Physics: Condensed Matter* **22**, 123201 (2010).
- [93] Y. Tokura, S. Seki, and N. Nagaosa, "Multiferroics of spin origin", *Reports on Progress in Physics* **77**, 076501 (2014).
- [94] H. T. Yi, Y. J. Choi, S. Lee, and S.-W. Cheong, "Multiferroicity in the square-lattice antiferromagnet of $\text{Ba}_2\text{CoGe}_2\text{O}_7$ ", *Applied Physics Letters* **92**, 212904 (2008).
- [95] M. Akaki, J. Tozawa, D. Akahoshi, and H. Kuwahara, "Gigantic magnetoelectric effect caused by magnetic-field-induced canted antiferromagnetic-paramagnetic transition in quasi-two-dimensional $\text{Ca}_2\text{CoSi}_2\text{O}_7$ crystal", *Applied Physics Letters* **94**, 212904 (2009).
- [96] H. Murakawa, Y. Onose, and Y. Tokura, "Electric-field switching of a magnetic propagation vector in a helimagnet", *Phys. Rev. Lett.* **103**, 147201 (2009).
- [97] H. Murakawa, Y. Onose, S. Miyahara, N. Furukawa, and Y. Tokura, "Comprehensive study of the ferroelectricity induced by the spin-dependent d - p hybridization mechanism in $\text{Ba}_2\text{xGe}_2\text{O}_7$ ($x = \text{mn, co, and cu}$)", *Phys. Rev. B* **85**, 174106 (2012).
- [98] J. "Oliveira, ""crystal-chemical investigations in the systems $\text{CuO} - \text{BaO} - \text{SiO}_2 - \text{GeO}_2$ and $\text{BaO} - \text{Rg}_2\text{O}_3$ """, *Heidelberger geowissenschaftliche Abhandlungen* **63**, 1 (1993).
- [99] M. Tovar, R. Dinnebier, and W. Eysel, "The Cu(II)O_4 tetrahedron in the akermanite structure", *Materials Science Forum* **278**, 750 (1998).
- [100] S. Kasap, *Principles of electronic materials and devices*, 3rd ed. (McGraw-Hill, Inc., USA, 2005).
- [101] A. Zheludev, G. Shirane, Y. Sasago, N. Kiode, and K. Uchinokura, "Spiral phase and spin waves in the quasi-two-dimensional antiferromagnet $\text{Ba}_2\text{CuGe}_2\text{O}_7$ ", *Phys. Rev. B* **54**, 15163 (1996).

- [102] A. Zheludev, S. Maslov, G. Shirane, Y. Sasago, N. Koide, and K. Uchinokura, "Field-induced commensurate-incommensurate phase transition in a dzyaloshinskii-moriya spiral antiferromagnet", *Phys. Rev. Lett.* **78**, 4857 (1997).
- [103] A. Zheludev, S. Maslov, G. Shirane, Y. Sasago, N. Koide, and K. Uchinokura, "Field-induced incommensurate-to-commensurate transition in $\text{Ba}_2\text{CuGe}_2\text{O}_7$ ", *Phys. Rev. B* **57**, 2968 (1998).
- [104] S. Mühlbauer, S. Gvasaliya, E. Ressouche, E. Pomjakushina, and A. Zheludev, "Phase diagram of the dzyaloshinskii-moriya helimagnet $\text{Ba}_2\text{CuGe}_2\text{O}_7$ in canted magnetic fields", *Phys. Rev. B* **86**, 024417 (2012).
- [105] M. Hoffmann, B. Zimmermann, G. P. Müller, D. Schürhoff, N. S. Kiselev, C. Melcher, and S. Blügel, "Antiskyrmions stabilized at interfaces by anisotropic dzyaloshinskii-moriya interactions", *Nature Communications* **8**, 308 (2017).
- [106] W. Kohn and L. J. Sham, "Self-consistent equations including exchange and correlation effects", *Phys. Rev.* **140**, A1133 (1965).
- [107] P. Giannozzi, S. Baroni, N. Bonini, M. Calandra, R. Car, C. Cavazzoni, D. Ceresoli, G. L. Chiarotti, M. Cococcioni, I. Dabo, A. D. Corso, S. de Gironcoli, S. Fabris, G. Fratesi, R. Gebauer, U. Gerstmann, C. Gougoussis, A. Kokalj, M. Lazzeri, L. Martin-Samos, N. Marzari, F. Mauri, R. Mazzarello, S. Paolini, A. Pasquarello, L. Paulatto, C. Sbraccia, S. Scandolo, G. Sclauzero, A. P. Seitsonen, A. Smogunov, P. Umari, and R. M. Wentzcovitch, "QUANTUM ESPRESSO: a modular and open-source software project for quantum simulations of materials", *Journal of Physics: Condensed Matter* **21**, 395502 (2009).
- [108] D. Vanderbilt, "Soft self-consistent pseudopotentials in a generalized eigenvalue formalism", *Phys. Rev. B* **41**, 7892 (1990).
- [109] K. Laasonen, A. Pasquarello, R. Car, C. Lee, and D. Vanderbilt, "Car-parrinello molecular dynamics with vanderbilt ultrasoft pseudopotentials", *Phys. Rev. B* **47**, 10142 (1993).
- [110] J. P. Perdew and W. Yue, "Accurate and simple density functional for the electronic exchange energy: generalized gradient approximation", *Phys. Rev. B* **33**, 8800 (1986).
- [111] J. P. Perdew, K. Burke, and Y. Wang, "Generalized gradient approximation for the exchange-correlation hole of a many-electron system", *Phys. Rev. B* **54**, 16533 (1996).
- [112] J. P. Perdew, K. Burke, and M. Ernzerhof, "Generalized gradient approximation made simple", *Phys. Rev. Lett.* **77**, 3865 (1996).
- [113] A. A. Mostofi, J. R. Yates, Y.-S. Lee, I. Souza, D. Vanderbilt, and N. Marzari, "Wannier90: a tool for obtaining maximally-localised wannier functions", *Computer Physics Communications* **178**, 685 (2008).

-
- [114] A. A. Mostofi, J. R. Yates, G. Pizzi, Y.-S. Lee, I. Souza, D. Vanderbilt, and N. Marzari, "An updated version of wannier90: a tool for obtaining maximally-localised wannier functions", *Computer Physics Communications* **185**, 2309 (2014).
- [115] H. A. Kramers, "Théorie générale de la rotation paramagnétique dans les cristaux", *Proc. Amsterdam Acad.* **33**, 959 (1930).
- [116] I. V. Solovyev, "Magnetization-induced local electric dipoles and multiferroic properties of $\text{Ba}_2\text{CoGe}_2\text{O}_7$ ", *Phys. Rev. B* **91**, 224423 (2015).

Curriculum Vitae

Ryota Ono

Graduate School of Science and Engineering, Department of Materials Science,
Chiba University, 1-33 Yayoicho, Inage, Chiba, 263-8522

Personal data

Date of Birth: 2 October 1994

Nationality: Japan

Work History

Research assistant

(2018-2019) : Graduate School of Science and Engineering, Chiba University

Research internship

(Jun./2018) : “Nanosystem Initiative München (NIM) Summer research” Ludwig-Maximilians-Universität München (LMU).

(Jun./2019, Nov./2019) : National Institute for Materials Science (NIMS)

(Aug./2019) : Tokyo Institute of Technology

Education

- | | |
|-----------------|--|
| 2013/3 | Highschool degree |
| 2013/4 - 2015/3 | National Institute of Technology, Sendai College |
| 2017/3 | <u>B. Sc</u> Faculty of Engineering, Department of Nanoscience, Chiba University |
| 2018/9 | <u>M. Sc</u> Graduate School of Science and Engineering, Department of Materials Science, Chiba University |
| 2021/3 | <u>PhD</u> Graduate School of Science and Engineering, Department of Materials Science, Chiba University |

Publications list

1. Ryota Ono and Peter Krüger “A one-dimensional model for photoemission calculations from plane-wave band structure codes”, e-J. Surf. Sci. Nanotechnol., vol 16, 49-52, 2018.
2. Ryota Ono, Sergey Nikolaev and Igor Solovyev, “Fingerprints of spin-current physics on magnetoelectric response in the spin-1/2 magnet $\text{Ba}_2\text{CuGe}_2\text{O}_7$ ”, accepted in Phys. Rev. B on 7th Aug. 2020 <https://arxiv.org/abs/2003.11765>, <https://journals.aps.org/prb/accepted/2e07aK8dD8a18401768e0280604256bc90cd6a81a>
3. Ryota Ono, Alberto Marmodoro, Yoshitaka Nakata, Jan Minár, Hubert Ebert, Jürgen Braun, Kazuyuki Sakamoto and Peter Krüger “Surface band characters of Weyl semimetal candidate MoTe_2 revealed by one-step ARPES theory” (submitted to Phys. Rev. B) <https://arxiv.org/abs/2010.13196>

Conference contributions list

(Oral)

1. ○Ryota Ono, Alberto Marmodoro, Yoshitaka Nakata, Jan Minár, Hubert Ebert, Jürgen Braun, Kazuyuki Sakamoto and Peter Krüger, “ARPES calculations of Weyl semimetal candidate material MoTe_2 ”, International Symposium on Spectro-Microscopy of Functional Materials and Interfaces, Chiba, Japan, October 2019.
2. ○Ryota Ono, Alberto Marmodoro, Yoshitaka Nakata, Jan Minár, Hubert Ebert, Jürgen Braun, Kazuyuki Sakamoto and Peter Krüger, “First-principles analysis of the surface states analysis of the type-II Weyl semimetal MoTe_2 ” (in Japanese), 74th Annual Autumn meeting of The Physical Society of Japan, Gihu, Japan, September 2019.
3. ○Peter Krüger, Ryota Ono and Alberto Marmodoro “Final state effects in ARPES of MoTe_2 and organic molecules”, 12th International Symposium on Atomic Level Characterizations for New Materials and Devices '19 (ALC '19), Kyoto, Japan, October 2019.

(Poster)

4. ○Ryota Ono, Peter Krüger, “Final state effects in ARPES from plane-wave band structure methods”, The 8th International Symposium on Surface Science (ISSS-8), Tsukuba, Japan, October 2017.
5. ○Ryota Ono, Alberto Marmodoro, Yoshitaka Nakata, Jan Minár, Hubert Ebert, Jürgen Braun, Kazuyuki Sakamoto and Peter Krüger, “Theoretical study of the candidate material for type-II Weyl semimetal MoTe_2 using relativistic KKR method”, Deutsche Physikalische Gesellschaft e.V. (DPG) Regensburg2019, Regensburg, Germany, April 2019.

6. ○Ryota Ono and Peter Krüger, “Matching method for ARPES intensity calculations from plane-wave basis” (in Japanese), 73th Annual March meeting of The Physical Society of Japan, Noda, Japan, March 2019.

Skills

Condensed matter theory (DFT, multiferroics, magnetism, many body physics, multiple scattering theory), ab-initio calculations (VASP, WIEN2k, QuantumEspresso), code development of DFT-based many-body methods (using wannier90, constrained RPA, spin model), theoretical development of effective Hamiltonians (spin Hamiltonian),

Acknowledgements

I would like to thank Prof. Peter Krüger and Dr. Igor Solovyev for providing me the project advises regarding. Discussing with them was always fruitful and precious to my experience as a researcher and also as a person.

I would like to thank all of my colleagues for interesting conversations and meaningful discussions on my study.

I would like to thank Frontier Science Program of Chiba University for giving me the opportunity to visit foreign country and do collaborations. Those surely made me a good researcher.

I am grateful to Prof. Yukinori Ohta, Prof. Takehisa Konishi, Prof. Nobuyuki Aoki, Prof. Kazuyuki Sakamoto and Dr. Sergey Nikolaev for valuable comments about this thesis.